Solid-state Dewetting of Continuous and Patterned Single Crystal Ni Thin Films

by

Jongpil Ye

B.S. Materials Science and Engineering
Seoul National University, 2005

SUBMITTED TO THE DEPARTMENT OF MATERIALS SCIENCE AND ENGINEERING IN PARTIAL FULFILLMENT OF THE REQUIREMENTS FOR THE DEGREE OF

DOCTOR OF PHILOSOPHY IN MATERIALS SCIENCE AND ENGINEERING
AT THE
MASSACHUSETTS INSTITUTE OF TEHNOLOGY

JUNE 2011

Signature of Author: _____

Department of Materials Science and Engineering
Feb 14, 2011

Certified by: _____

Carl V. Thompson
Stavros Salapatas Professor of Materials Science and Engineering
Thesis Supervisor

Accepted by: _____

Christopher A. Schuh
Chair, Departmental Committee of Graduate Students

Solid-state Dewetting of Continuous and Patterned Single Crystal Ni Thin Films

by

Jongpil Ye

Submitted to the Department of Materials Science and Engineering on Jan 27, 2011 in Partial Fulfillment of the Requirements of the Degree of Doctor of Philosophy in Materials Science and Engineering

Abstract

Solid-state dewetting of thin films is a process through which continuous solid films agglomerate to form islands. This process is driven by capillary forces, often occurring via surface self-diffusion. Solid-state dewetting of single crystal films has the potential to produce a wide range of regular structures because it occurs in ways controlled by crystallographic symmetries in single crystal films. We demonstrate this potential by pursuing two major objectives: understanding the underlying physics of regular morphological evolution during dewetting of single crystal films, and guiding the phenomenon to reproducibly produce regular structures with various morphologies.

We used single crystal Ni films grown on single crystal MgO substrates as a model system. Dewetting initiates with the nucleation of holes and proceeds through the retraction of film edges around holes. By analyzing the anisotropy of the edge retraction rate and facet morphologies, we show that the effect of the anisotropy of surface energy and surface diffusion on early-stage dewetting morphologies strongly depends on the initial film orientation and annealing ambient. A series of instabilities increases the complexity of morphological evolution in the latter stages of dewetting. These include in-plane faceting of retracting edges, accelerated growth at concave corners, edge drag at convex corners, edge pinch-off, and Rayleigh-like instabilities. Clear identification of these instabilities leads to improved understandings of the kinetic mechanisms that govern the formation of complex dewetting morphologies. We also demonstrate that solid-state dewetting can be used to produce regular structures with specific shapes via dewetting of patches patterned from single crystal films. Initial patches were systematically designed on the basis of the dewetting mechanisms to form a variety of specific morphologies. Morphological evolution of these patches occurs in more deterministic ways because of geometric constraints, and leads to the formation of regular structures with smaller sizes and more complex shapes than the initial patches.

Thesis Supervisor: Carl V. Thompson
Title: Stavros Salapatas Professor of Materials Science and Engineering

Dedicated to Minkyoung in love and gratitude

Table of Contents

List of Figures

Figure 1-11. Numerical results for the number of agglomerates that form during dewetting of films (a) with isotropic surface energy and (b) with anisotropic surface energy ($\gamma(\theta)=1+0.01332\cos(8\theta-\pi)$, where θ is the angle that the film surface makes with the substrate surface). The dashed-lines in (b) indicate the criteria for pinch-off of the film with isotropic surface energy. F and α indicate the thickness-to-width ratio of the film and the equilibrium contact angle at three-phase boundaries respectively.

Figure 1-12. Numerical results showing a perturbation on a thickened rim. This perturbation causes fingers with a characteristic spacing to form along the edge.

Figure 1-13. Formation of ordered arrays of crystallographically aligned gold nanoparticles via template-assisted solid-state dewetting. (a) SEM image of ordered arrays of single particles in each pit. Scale bar, 500 nm. (b) Pole figure x-ray diffraction pattern for the ordered arrays of gold particles.

Figure 1-14. Formation of ordered arrays of fingers and islands during dewetting of a (100) SOI film. (a) AFM image of a hole in a dewetting 7nm-thick (100)-bonded SOI film. Annealing was carried out at 950°C for 10 seconds in UHV. (b) AFM height profile along line K-L in (a).

Figure 1-15. Alignment of dewetted islands along edges of long line patterns. Long lines were patterned from (100) SOI films. SEM images of aligned islands and height profiles for long line patterns that were nearly parallel to the (a) [110] and (b) [010] directions. Height profiles were measured along the white lines in the SEM images.

Figure 2-1. Schematic illustration of the pole figure XRD geometry. (a) Goniometer and sample stage. Important angles are indicated in the illustration. (b) Example of an x-ray diffraction pattern in an equal area net. Rotation angles are indicated in the equal area net.

Figure 2-2. Schematic illustration of a 2θ-ω scan. This scan determines the value of 2θ seen in the figure. The value of ω seen in the figure is obtained from a rocking curve scan. The tilt angle between the substrate and film can be calculated using these values as shown in the illustration.

Figure 3-1. XRD patterns for 120nm-thick Ni(100) and Ni(110) films. (a) Theta-2theta patterns. (b) Pole figure XRD patterns. Out-of-plane orientations of Ni films and MgO substrates are indicated in the patterns.

Figure 3-2. Atomic force microscope (AFM) images of growing natural holes in Ni(100) and Ni(110) films at two different reducing gas flow rates. The annealing times are indicated in the images. (a), (b) Ni(100), 2310 sccm. (c), (d) Ni(100), 12 sccm. (e), (f) Ni(110), 2310 sccm. (g), (h) Ni(110), 12 sccm.

Figure 3-3. TEM images showing the rim shape of the longest edge of a natural hole that has the same shape as the natural hole shown in Fig. 3-2(h) (the longest edge is perpendicular to the $[1\bar{1}0]$ direction in a Ni(110) film).

Figure 3-4. Anisotropic edge retraction velocity. (a) Photolithography mask pattern and the patterned islands used to measure the edge retraction velocity. The general faceting behaviors along the edges are also shown in SEM images on the right. (b)-(e) Polar plots of the edge retraction distance after annealing for 318 minutes. The film orientation and the flow rate of reducing gas are indicated in each polar plot.

Figure 3-5. Faceting of long retracting edges. (a) Ni(100), 2310 sccm. (b) Ni(100), 12 sccm. (c) Ni(110), 2310 sccm. (d) Ni(110), 12 sccm. The arrows indicate the in-plane orientations of the two stable edges at lowest angles of rotation.

Figure 3-6. Schematic illustration of the retraction of a faceted edge. The dashed lines in the diagram indicate the macroscopic orientation of the edge. The edge retraction velocity can be expressed as the distance between the two dashed lines.

Figure 3-7. Stereographic projection of {111}, {100}, {110}, and {210} faces of a cubic crystal (a) (100) projection. (b) (110) projection. These stereographic projections were plotted using MTEX, an open source texture analysis MATLAB code.

Figure 3-8. AFM height profiles of some stable edges in pre-patterned Ni(110) films. The flow rate of reducing gas, annealing time, and edge retraction directions are indicated in each height profile. There are small errors in measured angles that might be caused by AFM tip artifacts or small deviations of the scan directions from the edge normal directions.

Figure 3-9. AFM height profiles of some stable edges in pre-patterned Ni(100) films. The annealing condition, annealing time, and edge retraction directions are indicated in each height profile. There are small errors in measured angles that might be caused by AFM tip artifacts or small deviations of the scan directions from the edge normal directions.

Figure 3-10. Striations on the flat film surface behind the pre-patterned edge retracting in the <011> direction in a Ni(100) film. The lower left figure is an AFM image and the upper right figure is a corresponding height profile of the flat surface behind the edge. The angle between the terrace and the horizontal line is indicated in the AFM height profile.

Figure 3-11. High resolution XRD measurements for the sample shown in Fig. 3-10. (a) Rocking curve for MgO(100). (b) Rocking curve for Ni(100). (c) 2θ-ω scan for MgO(100). (d) 2θ-ω scan for Ni(100).

Figure 3-12. Retraction distances of 90 μm-long edges versus annealing time. (a) The edge that retracts in the [001] direction in Ni(110) film. (b) The edge that retracts in the [011] direction in Ni(100) film. The data were collected from samples annealed in a reducing gas flow rate of 2310 sccm. The data are well-fitted by a power-law with the exponent of 0.4 for (a) and 0.56 for (b).

Figure 3-13. Schematic diagram of the diffusion field around a growing natural hole in a Ni(110) film.

Figure 4-1. AFM images of growing natural holes in Ni(100) and Ni(110) films after their edges have become unstable. (a), (b) Ni(100), 2310 sccm. (c), (d) Ni(100), 12 sccm. (e)-(h) Ni(110), 2310 sccm. (i)- (l) Ni(110), 12 sccm. The annealing times are indicated in the images.

Figure 4-2. Schematic illustration of the diffusion field around a natural hole, illustrating the cause of a corner-induced instability.

Figure 4-3. The change of the rim height and rim width across the corner and edge center of a natural hole in a Ni(100) film during annealing. (a) and (b) At a reducing gas flow rate of 2310 sccm. (c) and (d) At a reducing gas flow rate of 12 sccm.

Figure 4-4. The change of the rim height and rim width across the corner and edge center of a natural hole in a Ni(110) film during annealing. (a) and (b) At a reducing gas flow rate of 2310 sccm. (c) and (d) At a reducing gas flow rate of 12 sccm. The directions in each plot indicate the retraction directions of the two edges of a natural hole in a Ni(110) film.

Figure 4-5. Growth of square and rectangle holes with various initial sizes and aspect ratios, all of which were patterned from a Ni(110) film. Holes were patterned using FIB milling. Initial dimensions of pre-patterned holes are indicated above each image. The in-plane crystallographic orientation is indicated in the lower-left corner. Scale bar, 2 μm.

Figure 4-6. Retraction distance at the centers of edges with different initial lengths versus the total annealing time, (a) in the <001> directions and (b) in the <110> directions.

Figure 4-7. Deepening of valleys and pinch-off of edges in a natural hole in a Ni(110) film. The flow rate of reducing gas was 2310 sccm. (a)-(c) AFM height images. (d)-(f) AFM height profiles. The annealing times are indicated in the figures.

Figure 4-8. SEM images of complex morphologies in the late stage of morphological evolution. (a) through (c) Images of a dewetting Ni(110) film, (a) annealed for 1255 minutes and (b) annealed for 4495 minutes. (d) through (e) Images of a dewetting Ni(100) film, (d) annealed for 3240 minutes and (e) annealed for 4200 minutes. The flow rate of reducing gas was 2310 sccm.

Figure 5-1. Dewetting of square patches patterned from a Ni(110) film. (a)-(d) AFM images of evolving square patches with various initial sizes. The initial edge length of each patch was about 18.4, 14.6, 10.8, and 8.9 μm respectively. The total annealing time was 270 minutes, 540 minutes, and 1020 minutes from the left to right panel. The in-plane crystallographic orientation is indicated in the lower-left corner. Scale bars, 4 μm. (e)-(h) Height profiles for each of the patterns on the left. The height profiles were measured along the dashed lines in the AFM images. The dashed lines in the height profiles show the initial film thickness.

Figure 5-2. Dewetting of cross patches patterned from a Ni(110) film. (a) SEM image of the dewetted pattern that evolved from a smaller cross patch. The edge length of an initial patch was about 10.8 μm. (b) SEM image of the dewetted pattern that evolved from a larger cross patch. The edge length of an initial patch was about 18.4 μm. The gray dashed lines indicate the initial shapes of the patches. The in-plane crystallographic orientations are indicated in the lower-left corners. The total annealing time was 1020 minutes. Scale bar, 10 μm. These images were taken in low vacuum mode.

Figure 5-3. Schematic illustration of the cross section of patches with different width, W, to thickness, H, ratios, dewetting into one, two or three lines (after Dornel et al).

Figure 5-4. (a)-(b) Tilt-corrected SEM images of FIB-milled cross sections of the lines shown in Fig. 5-2(a). Before milling, the lines were coated with carbon and platinum to reduce charging and protect the nickel. The curved lines are artifacts of milling of these protective layers. Scale bar, 400 nm. (c)-(d) AFM images of thickened edges retracting in the $[1\bar{1}0]$ and [001] directions. The annealing time was 270 minutes. (e)-(f) Height profiles of the thickened edges seen in (c) and (d). These were measured from the substrate surface to the top of the facets. The actual angles in the profiles approximately match the ideal angles of the indicated facets.

Figure 5-5. AFM image at a relatively early stage of dewetting of a cross patch with the same initial dimensions as the cross patch of Fig. 5-2(b). The annealing time was 270 minutes. The heights of the valleys from the substrate surface were measured along the dashed lines. The results are shown on the right.

Figure 5-6. Retraction and pinch-off of long lines perpendicular to the $[1\bar{1}0]$ direction. (a)-(c) Images of long lines annealed for 540 minutes. (d)-(f) Images of long lines annealed for 1020 minutes. (h)-(j) Images of long lines annealed for 1600 minutes.

Figure 5-7. Retraction and pinch-off of long lines perpendicular to the [001] direction. (a)-(c) Images of long lines annealed for 540 minutes. (d)-(f) Images of long lines annealed for 1020 minutes.

Figure 5-8. AFM images around the middle of evolving long line patches. (a) The patch with long edges perpendicular to the $[1\bar{1}0]$ direction. (b) The patch with long edges perpendicular to the [001] direction. Annealing times are indicated in each image. The initial widths were 11.1 μm and 11.7 μm respectively.

Figure 5-9. Dewetting of a square patch patterned from a Ni(110) film. The annealing was carried out in a Transtemp furnace under a reducing gas flow rate of 90 sccm. The initial width was about 17.6 μm. The annealing time was 1020 minutes. Scale bar indicates 10 μm.

Figure 5-10. The shape of thickening rims that developed via edge retraction. (a) Annealed in a Transtemp furnace at 90 sccm for 318 minutes. (b) Annealed in a Lindberg/Blue Mini-Mite furnace at 2310 sccm for 270 minutes.

Figure 5-11. Dewetting of square patches patterned from a Ni(100) film. (a)-(d) AFM images of evolving square patches with various initial sizes. The initial edge length of each patch was about 19.3, 15.4, 11.6, and 9.7 μm respectively. The total annealing time was 270 minutes, 540 minutes, and 1020 minutes from the left to the right panel. The in-plane crystallographic orientation is indicated in the lower-left corner. Scale bars, 4 μm. (e)-(h) Height profiles for each of the patterns on the left. The height profiles were measured along the dashed lines in the AFM images.

Figure 5-12. AFM images showing the variation in height along thickening rims of the dewetting pattern shown in Fig. 5-11(a). Both the top-view (left-side) and the 90-degree tilted-view (right-side) images are shown. Arrows indicate relatively low parts of thickening rims. The annealing times are indicated on the left.

Figure 5-13. AFM image showing the shape of a thickening rim in a Ni(100) film. The annealing time was 318 minutes.

Figure 5-14. Descriptions for parameters in Equation 5-2.

Figure 5-15. Schematic illustration showing (a) the initial shape and (b) the equilibrium shape of a 2-dimensional thin film whose evolution is simulated. The bottom facet is attached to the substrate.

Figure 5-16. Simulation example showing the effect of the initial film width on the pinch-off phenomenon during evolution of two films.

Figure 5-17. Simulation example showing the effect of the anisotropy of surface energy on the pinch-off phenomenon during evolution of two films.

Figure 5-18. Dependence of the pinch-off phenomenon on the initial width of a film and the surface energy anisotropy.

Figure 5-19. Dependence of the pinch-off phenomenon on the initial width and surface diffusivity of a film

Figure 5-20. The equilibrium shape and simulation result in a partial wetting condition. Compare the result on the right to the result on the right in Fig. 5-16.

Figure 5-21. Dependence of the pinch-off phenomenon on the initial width of a film and the film-substrate adhesion energy. (a) The equilibrium shape. Wad indicates the adhesion energy between the film and substrate. (b) The simulation result.

Figure 5-22. The edge retraction distance versus time in the different conditions of surface energy anisotropy. The edge retraction distance at time t is calculated by dividing the change in length of the film-substrate interfacial facet by 2.

Figure 6-1. A polar array of square patches with or without internal holes. Scale bar, 200 μm

Figure 6-2. Dewetting of square patches with edges oriented in various in-plane crystallographic directions, all of which were patterned from a Ni(110) film. (a) and (b) SEM images of evolving square patches with two different in-plane orientations, (a) square patches with a relatively small initial size. The initial edge length was about 12 μm. (b) Square patches with a relatively large initial size. The initial edge length was about 19.7 μm. The total annealing time was 270 minutes, 540 minutes, and 1020 minutes from the left to right panel. The gray dashed lines indicate the initial shapes of the patches. (c) and (d) SEM images of a group of dewetted patterns with four different in-plane orientations. (c) The initial edge length was 12 μm and (d) the initial edge length was 19.7 μm. The total annealing time was 1020 minutes. The in-plane crystallographic orientations are indicated in the lower-left corner. Scale bars, 10 μm.

Figure 6-3. Dewetting of square patches patterned from a Ni(100) film. (a) SEM images of evolving square patches with three different in-plane orientations. The total annealing time was 270 minutes and 540 minutes from the top to bottom panel. The gray dashed lines indicate the initial shapes of the patches. The in-plane crystallographic orientations are also indicated. (b) SEM images of a group of dewetted patterns seen in (a). The total annealing time was 540 minutes. Scale bars, 10 μm.

Figure 6-4. SEM images of dewetted structures that evolved from square ring patches with two different in-plane orientations. (a) Patterned from a Ni(110) film. (b) Patterned from a Ni(100) film. The total annealing time was 1020 minutes. The gray dashed lines indicate the initial shapes of the patches. The in-plane crystallographic orientations are also indicated. Scale bars, 5 μm

Figure 6-5. Dewetting of square patches with circular internal holes and with edges oriented in different in-plane crystallographic directions, all of which were patterned from a Ni(110) film. The total annealing time was 540 minutes and 1020 minutes from the top to bottom panel. The gray dashed lines indicate the initial shapes of the patches. The in-plane crystallographic orientations are indicated in the lower-left corner. Scale bars, 5 μm.

Figure 6-6. SEM images showing dewetting results for square patches with off-centered internal square holes, all of which were patterned from a Ni(110) film. (a) Off-centered in the [001] direction. (b) Off-centered in the $[1\bar{1}0]$ direction. The annealing time was 1020 minutes. The gray dashed lines indicate the initial shapes of the patches. The in-plane crystallographic orientations are also indicated. Scale bars, 10 μm

Figure 6-7. SEM images of (a) square and (b) circular patches with inverted T-shaped internal holes patterned from a Ni(110) film. The gray dashed lines indicate the initial shapes of the patches. The initial shapes were the same for patterns in the same column of each image. The position of the T-shaped internal holes within the patterns changes going from left to right. The in-plane orientation is indicated in the lower-left corner. The annealing time was 1020 minutes. Scale bar, 10 μm.

Figure 6-8. Dewetting of cross patches with pre-patterned internal circular holes patterned from a Ni(110) film. (a) through (c) are SEM images of dewetted patterns with an initial edge length of 10.8 μm. (d) through (i) are SEM images of dewetted patterns with an initial edge length of 18.4 μm. The gray dashed lines indicate the initial shapes of the patches. The in-plane orientation is indicated in the lower-left corner. The annealing time was 1020 minutes. Scale bars, 10 μm.

Figure 6-9. AFM images and height profiles of dewetting cross patterns. AFM images show the earlier-stage morphology of the pattern shown in Fig. 6-8(i) (upper image) and 6-8(d) (lower image). The annealing time was 540 minutes.

Figure 6-10. Dewetting of cross patches with pre-patterned internal holes patterned from a Ni(100) film. (a) though (d) are SEM images of dewetted patterns with an initial edge length of 11.6 μm. (d) through (i) are SEM images of dewetted patterns with an initial edge length of 19.2 μm. The gray dashed lines indicate the initial shapes of the patches. The in-plane orientation is indicated in the lower-left corner. The annealing time was 1020 minutes. Scale bars, 10 μm.

Figure A-1. SEM images showing dewetting results for Ni(110) films with various initial film thicknesses. The initial film thickness and annealing time is indicated for each image. The in-plane crystallographic orientations are also indicated in each image.

Figure B-1. AFM images showing dewetting results for 15nm-thick Ni(110) films. (a) Annealed at 500°C. (b) Annealed at 900°C.

Figure B-2. SEM images of natural holes that formed during dewetting of 120nm-thick Ni(110) films. (a) Annealed at 900°C for 30 minutes. (b) Annealed at 800°C for 2.5 hours. (c) Annealed at 700°C for 6 hours. The in-plane crystallographic orientation is indicated in the lower-left corner.

Figure C-1. The edge retraction distance versus time for different magnitudes of the adhesion energy. The larger value of N_{ad} indicates the higher adhesion energy. The edge retraction distance at time t is calculated by dividing the change in length of the film-substrate interfacial facet by 2.

Acknowledgement

First of all, I would like to thank my advisor, Professor Carl Thompson, for having guided and encouraged me with much patience for the past five years. I am also grateful to my committee members, Professor Caroline Ross and Professor Craig Carter, for their useful comments and suggestions on my thesis and presentation.

I am also thankful to the research staffs at MIT and Harvard: Kurt Broderick, Libby Shaw, Scott Speakman, and Richard Schaleck. They all have been great teachers to me, offering technical advice and support. I also want to thank former and present Thompson group members for helping me adapt to the new environment and for giving me a hand whenever I struggled with my experiments.

I would like to express my sincere gratitude to my parents and younger brother, Jongmin, for their love and endless support.

Most of all, I would like to give my deepest thanks to my wife, Minkyoung, for believing in me and for supporting me throughout many tough moments.

Chapter 1 Introduction

1.1 Solid-state dewetting of thin films

Because thin solid films are generally deposited under conditions far from equilibrium, they often become unstable and evolve into equilibrium morphologies when they are heated to sufficiently high temperatures below film's melting temperature. The equilibrium film morphology depends on relative magnitudes of three interfacial energies: film-vapor interfacial energy (film surface energy) γ_{fv}, substrate-vapor interfacial energy (substrate surface energy) γ_{sv}, and film-substrate interfacial energy γ_{fs}. Young derived an expression for thermodynamic equilibrium between the three phases as follows,

$$\gamma_{sv} = \gamma_{fs} + \gamma_{fv} \cos\theta \ , \tag{1.1}$$

where θ is the equilibrium contact angle at three-phase boundary. When $\gamma_{sv} \geq \gamma_{fv} + \gamma_{fs}$, the equilibrium contact angle is 0˚ and film wets the substrate and the equilibrium film morphology is a continuous flat film. However, for other cases, the equilibrium contact angel is nonzero, which means that the equilibrium film morphology will be a mound as illustrated in Fig. 1-1 assuming isotropic interfacial energy. Therefore, for nonzero equilibrium contact angles, continuous flat films decompose into arrays of isolated islands to minimize the total interfacial energy of the system, when heated to sufficiently high temperatures. This process is called dewetting.

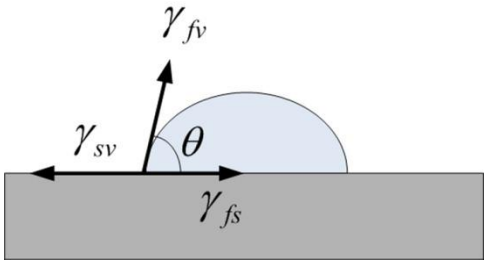

Figure 1-1. Schematic illustration of equilibrium film morphology when the equilibrium contact angle θ is nonzero.

Equilibrium shapes of islands on a foreign substrate and with anisotropic surface energy can be determined through the Winterbottom construction [1], which is a modified Wulff construction. As shown in Fig. 1-2(a), the Wulff construction yields an equilibrium shape of a free-standing solid with anisotropic surface energy by drawing lines perpendicular to the vector representing the surface energy at each orientation and finding the area enclosed by these lines. This enclosed area represents a surface energy minimizing shape of the free-standing solid under conditions of constant volume. In the Winterbottom construction, the wetting interaction between the film and substrate is also considered. The vector in the Wulff construction is replaced with the vector representing the adhesion energy $(\gamma_{fs}- \gamma_{sv})$ at the orientation of the film-substrate interface, as shown in Fig. 1-2(b). Therefore, the equilibrium shape of a film on a foreign substrate and with anisotropic surface energy is predicted to depend on the magnitude of the adhesion energy between the film and substrate.

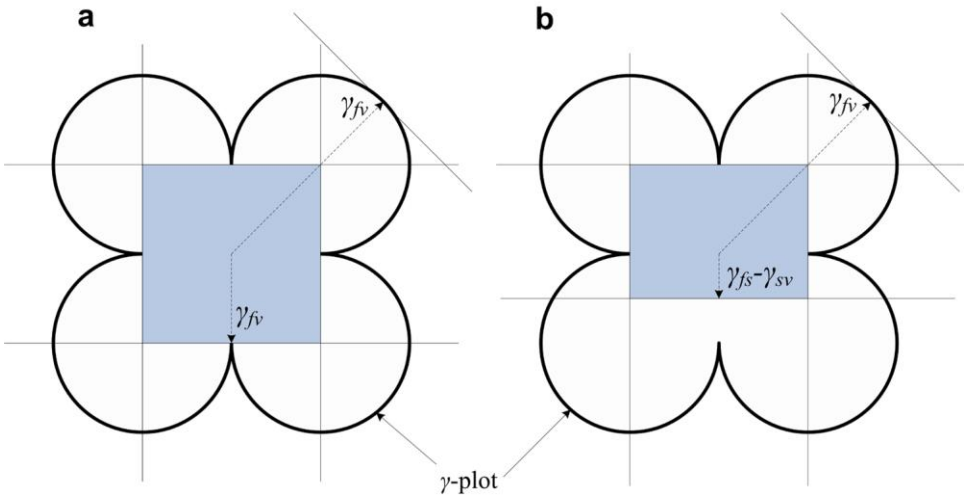

Figure 2-2. Geometric constructions yielding the equilibrium shape of a two-dimensional solid with square symmetry. γ_{fv} is the surface energy of the solid (film material), γ_{sv} is the surface energy of the substrate, and γ_{fs} is the film-substrate interfacial energy. (a) Wulff construction. (b) Winterbottom construction.

1.2 Mechanisms of solid-state dewetting of thin films

1.2.1 Surface evolution driven by capillarity

Dewetting of thin films occurs via motion of film surfaces to decrease the free energy associated with film interfaces. The driving force for this type of motion is called a capillary force. In the presence of capillary effects, chemical potentials of surface components (ad-atoms or vacancies) depend on local surface curvature, and are given by Gibbs-Thomson equation,

$$\mu = \mu^{\circ} + \kappa\gamma\Omega\,, \tag{1.2}$$

where μ° is the chemical potential at a flat surface, κ is the local surface curvature, γ is the surface energy, Ω is the atomic volume. Therefore, variations in surface curvature drive mass transport and surface evolution. Surface diffusion and evaporation-condensation

processes are the transport mechanisms typically considered for surface evolution driven by capillarity. For surface diffusion and on a film with isotropic surface energy, the gradient in local surface curvature drives the motion of surface atoms along the surface and the atomic flux is given by Nernst-Einstein relation,

$$J_s = \frac{D_s \gamma \Omega \nu}{kT} \vec{\nabla}_s \kappa, \tag{1.3}$$

where κ_s is the local surface curvature, D_s is the surface diffusivity, γ is the isotropic surface energy, Ω is the atomic volume, ν is the number of atoms per unit area.

For evaporation-condensation kinetics, the atomic flux direction is normal to the surface and is given by,

$$J_v = K(P_{amb} - P_{eq}(\kappa)), \tag{1.4}$$

where P_{amb} is the ambient vapor pressure, $P_{eq}(\kappa)$ is the equilibrium vapor pressure at a local surface with surface curvature κ, K is a rate constant that is related to the density of condensation sites and the condensation rate. Due to the difference in the path of the atomic flux for the two different mass transport mechanisms, shapes of evolving surfaces depend on the mass transport mechanisms. Carter et al. [2] computed shape evolution via the two mass transport processes driven by capillarity for anisotropic surface energy. They showed that convex regions of a surface can become concave regions through the formation of locally thickened areas for surface diffusion kinetics while convex regions remain convex for evaporation-condensation kinetics (surface attachment limited kinetics). Figure 1-3 shows the shape evolution of 2-dimenstional faceted crystals via the two mass transport processes. As seen in the figure, local thickening is observed near the

end of the two dimensional crystal for surface diffusion kinetics, leading to the formation of concave regions behind the thick regions. This characteristic of a surface shape evolving via surface diffusion can also be seen during solid-state dewetting of thin films. This will be further discussed later in this chapter and in connection with experimental results obtained in this study.

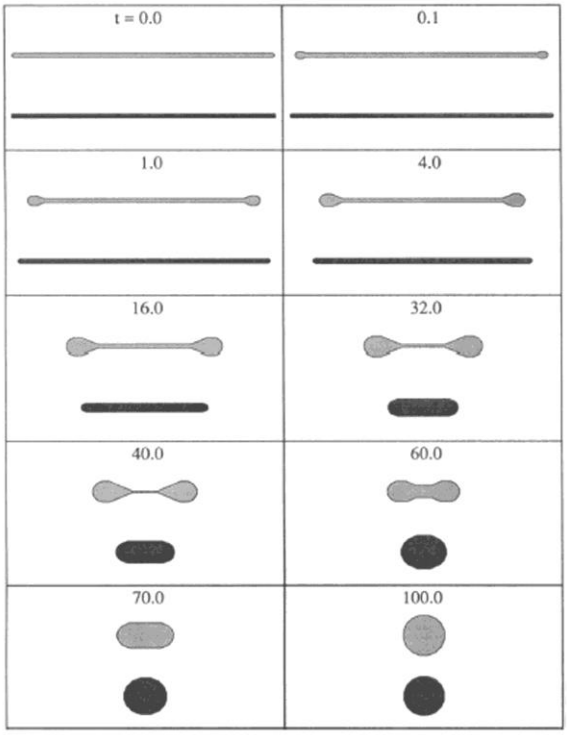

Figure 1-3. Time evolution of an elongated rectangle with a regular 16-gon equilibrium shape. Light gray shapes indicate evolution is motion by surface diffusion and dark gray shapes indicate evolution by evaporation-condensation. [2]

1.2.2 Nucleation of holes

Mullins demonstrated that perturbations of an isotropic solid plane surface spontaneously decay to reduce surface area by mathematically analyzing the evolution of perturbations in the small slope regime [3]. This demonstration implies that solid-state dewetting of thin films requires the nucleation of holes that reach the substrate surface. For the case of polycrystalline films, grooving at grain boundary triple junctions or grain boundaries provides a mechanism for hole nucleation. Mullins studied the kinetics of grain boundary grooving via evaporation-condensation as well as surface diffusion and showed that grain boundary grooves have a time-independent shape with a depth proportional to $t^{1/2}$ for evaporation-condensation and $t^{1/4}$ for surface diffusion [4]. Srolovitz and Safran further studied grooving at arrays of grain boundaries and grain boundary triple junctions and developed criteria for film rupture [5]. They showed that groove at a grain boundary triple junction generally penetrates the film to touch the substrate surface. They also demonstrated that there is a critical hole size required for continuous growth of nucleated holes. Holes with smaller sizes than the critical size were found to shrink and eventually disappear. For the case of single crystal films, it has been suggested that nucleation of supercritical holes occurs at defects such as protrusions on a substrate surface or scratches on a film surface based on the large barrier for homogenous nucleation of a supercritical hole [6].

1.2.3 Growth of holes via edge retraction

Nucleation of supercritical holes leads to the formation of film edges at which large local surface curvature develops. The growth of holes is induced by the large local surface curvature at film edges and continues via retraction at the film edges. The kinetics of edge retraction (hole growth) for isotropic surface energy has been investigated in several studies [7-10] and different time-dependencies of the edge retraction velocity were derived. Srolovitz and Safran considered the growth of cylindrical holes for both surface diffusion kinetics and evaporation-condensation kinetics [7]. They found a steady-state surface profile and a constant hole growth rate that is inversely proportional to the initial thickness of a film in the large hole size limit for evaporation-condensation kinetics. However, for surface diffusion kinetics, both the surface profile and hole growth rate were found to change with time. Equation 1.3 can be converted to an equation for the velocity of the surface normal using the continuity equation to give [4],

$$V_n = B_s \nabla_s^2 \kappa_s , \qquad (1.4)$$

$$B_s = \frac{D_s \gamma \Omega^2 \nu}{kT} ,$$

where κ_s is the local surface curvature, D_s is the surface diffusivity, γ is the isotropic surface energy, Ω is the atomic volume, ν is the number of atoms per unit area. Srolovitz and Safran solved Equation 1.4 numerically in cylindrical coordinates and in the small slope limit. They showed that the surface profile consists of a thickening rim adjacent to a deepening valley as seen in Fig. 1-4, and that the hole growth rate decreases over time and is proportional to $t^{-3/4}$.

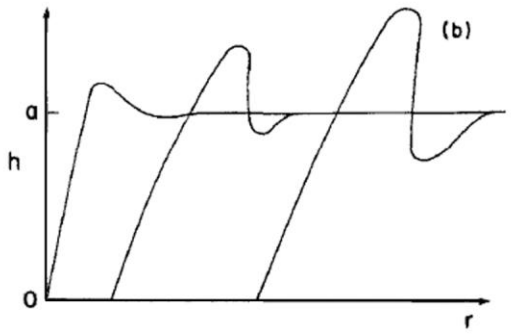

Figure 1-4. Schematic view of the profile of a film edge retracting via surface diffusion. [7]

Kinetic equations for hole growth (or edge retraction) have also been derived from phenomenological models based on experimental observations of morphologies of growing holes during dewetting of thin films. Figure 1-5 shows schematic surface profiles of retracting hole edges suggested in two representative kinetic models for edge retraction: the 1) Brandon and Bradshaw and 2) Jiran and Thompson models. Both models considered surface diffusion as the mass transport mechanism for edge retraction and were consistent with experimental observations in each study.

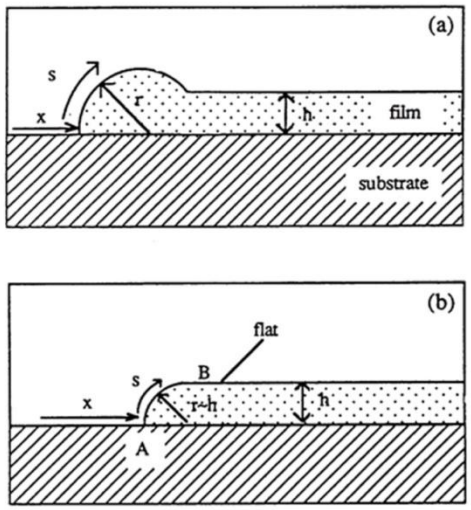

Figure 1-5. Schematic profiles of retracting edges according to the (a) Brandon and Bradshaw model and (b) Jiran and Thompson model. [9]

Brandon and Bradshaw observed dewetting of single crystal silver films deposited on mica substrates [10]. Dewetting occurred through nucleation, growth, and coalescence of holes with circle-like shapes as seen in Fig. 1-6. Thickening rims around growing holes seen in the figure suggests that this morphological evolution occurs via surface diffusion rather than evaporation-condensation. Brandon and Bradshaw simplified the surface profile of retracting edges by assuming that the cross-section of the thickening rim is a semi-circle of radius r and the contact angle of the film with the substrate at three-phase line is 90˚ as illustrated in Fig. 1-5(a). They also assumed perfect circular shapes of growing holes. In this model, film materials diffuse along the film surface from the film edges where the surface curvature is 1/r to the top flat film surface where the surface curvature is about zero and the surface diffusion results in edge retraction. By

using Equation 1.3 and the continuity equation, they derived an equation for the growth rate of a hole,

$$\frac{dR}{dt} = \left(\frac{2h}{5B_s^{2/3}\pi^{1/3}} \right)^{-3/5} t^{-3/5}, \qquad (1.5)$$

where R is the radius of a hole, h is the initial film thickness, t is the annealing time, B_s is as previously defined in Equation 1.4. This equation was in a quantitative agreement with their experiment results. They tracked and measured the diameter of growing holes and showed that the values of $(d_{final})^{5/2} - (d_{initial})^{5/2}$ had a very closely linear relationship with time interval between the initial and final measurement, as predicted by Equation 1.5. The decrease of the edge retraction velocity with annealing time can also be qualitatively understood in terms of the decrease in the surface curvature gradient (driving force) between the film edge and top film surface due to thickening of rims.

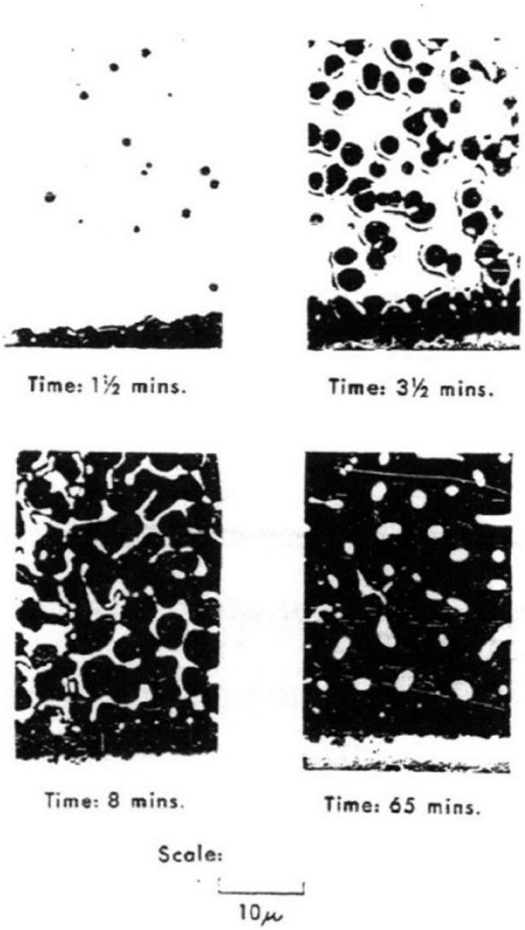

Figure 1-6. Optical micrographs of morphological evolution during dewetting of 110 nm-thick Ag films deposited on mica substrates. Thickening rims are observed around growing holes. The film was annealed at 360°C in air. Annealing times are indicated under each micrograph. [10]

Jiran and Thompson observed more complex morphological evolution during dewetting of gold films deposited on silica substrates [8, 9]. Holes grew unstably and formed complex shapes during dewetting, as seen in Fig. 1-7(a). They found that accumulation of material was uneven around edges of growing holes as seen in Fig. 1-7(b), and that edges retracted faster where accumulation of material was less, leading to unstable hole growth. They analyzed the dewetting morphologies in detail and suggested the following phenomenological model. In the very early stage, edges of holes retract via surface diffusion and develop thickening rims. In this stage, the edge retraction velocity decreases with time, as suggested by Brandon and Bradshaw. However, thickening rims become unstable and perturbations in their thickness develop, making certain areas of the rims thinner than others. Due to the higher surface curvature gradient across the thinner parts of thickened rims, edges retract much faster through the thinner parts, forming fingerlike morphologies as seen in Fig. 1-7(a). Accumulation of material to the side of the fingerlike edges seen in Fig. 1-7(b) indicates that material diffuses away from the fronts of fast-retracting fingerlike edges and piles up to the sides of the fingerlike edges. Due to the accumulation of material, the sides of fingerlike edges become nearly stagnant. These stagnant sides evolve to fingers of film material via retraction of a series of fingerlike edges and subsequently decay into isolated beads as illustrated in Fig. 1-8. Based on these observations and analysis of morphologies of dewetted films, Jiran and Thompson concluded that dewetting rate of the gold thin films is controlled by the retraction velocity of the fingerlike edges.

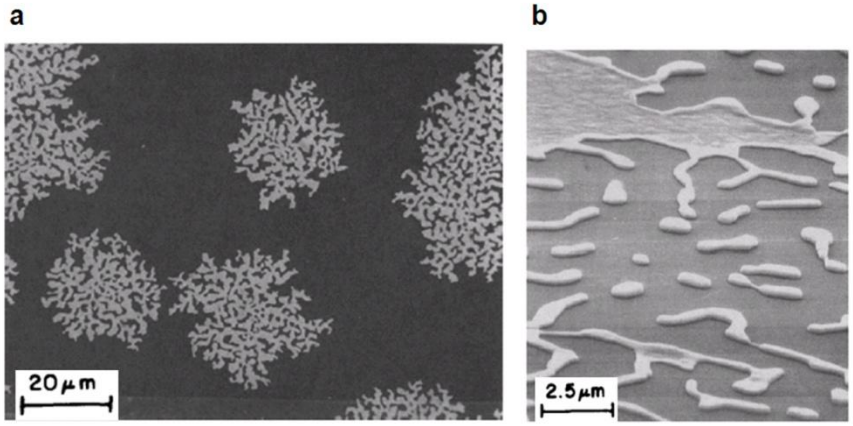

Figure 1-7. Unstable hole growth during dewetting of 30 nm-thick gold films on fused silica substrates. (a) An optical micrograph of growing holes with complex shapes. The micrograph was made using transmitted light. The dark area is gold and bright areas are exposed silica substrate. (b) An SEM image showing uneven accumulation of material around the edges of unstably growing holes. [9]

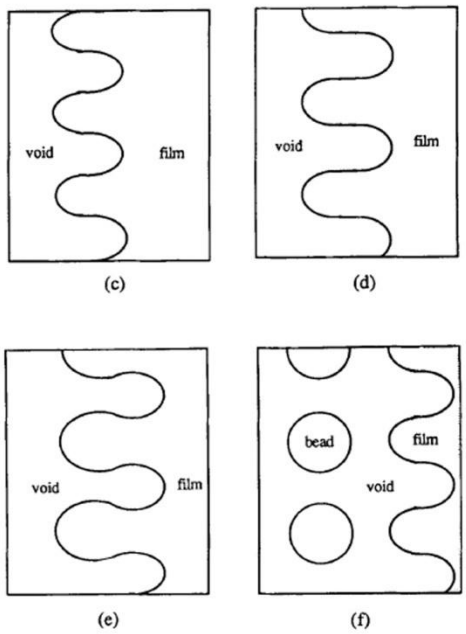

Figure 1-8. Schematic illustration of the edge instability that leads to formation of fingerlike morphologies and isolated beads. [9]

Jiran and Thompson expanded on the Brandon and Bradshaw model to build a model for unstable hole growth. In their model, edge retraction in the very early stage was described using the Brandon and Bradshaw model. However, for the later stage of hole growth, in which retraction of fingerlike edges determines the dewetting kinetics, they modeled retraction of fingerlike edges using the surface profile seen in Fig. 1-5(b), given that material diffuses away from the fast-retracting fingerlike edges and therefore there is no accumulation of material ahead of the fingerlike edges. A simple calculation similar to that of Brandon and Bradshaw led to the following expression for the retraction velocity of fingerlike edges,

$$\frac{dx}{dt} = \frac{2B_s}{\pi h^3}, \tag{1-6}$$

where x is the location of a fingerlike edge, t is the annealing time, h is the initial film thickness, B_s is as previously defined in Equation 1.4. This equation indicates that the retraction velocity of a fingerlike edge remains constant over time. The constant velocity can be understood in terms of a constant surface curvature gradient at fingerlike edges of this model. Jiran and Thompson also showed quantitative evidence for the constant retraction velocity of fingerlike edges through measurements of light transmittance through dewetting patterned and continuous gold films on silica substrates [9].

1.2.4 Mass shedding, Fingering instability, and Rayleigh-like instability

Kinetic processes other than edge retraction can also be observed during dewetting of thin films: Mass shedding, fingering, and break-up of lines into particles. As seen in the characteristic surface profile of Fig. 1-4, the numerical analysis of Srolovitz and Safran showed that valleys develop and deepen behind edges of growing holes for hole growth via surface diffusion. Srolovitz and Safran also found that the valleys eventually reach the substrate surface to form new hole edges unless growing holes impinge earlier. They speculated that the hole growth rate will greatly increase after the formation of new edges and decrease again as the new rims thicken. Wong et al. studied the deepening of valleys more extensively through a two-dimensional numerical analysis of edge retraction of semi-infinite films [11]. They found that valleys reach the substrate surface at a time that depends on the equilibrium contact angle at three-phase lines (Schematic illustration for this "pinch-off" process is shown in Fig. 1-9). As seen in Fig. 1-10(a), valleys reach the substrate surface at earlier times for larger equilibrium contact angles. The pinch-off of edges leads to the detachment of thickened rims from the film, which Wong and Voorhees called a mass shedding process. They showed that this mass shedding process occurs periodically and results in a great increase in the average edge retraction velocity as shown in Fig. 1-10(b).

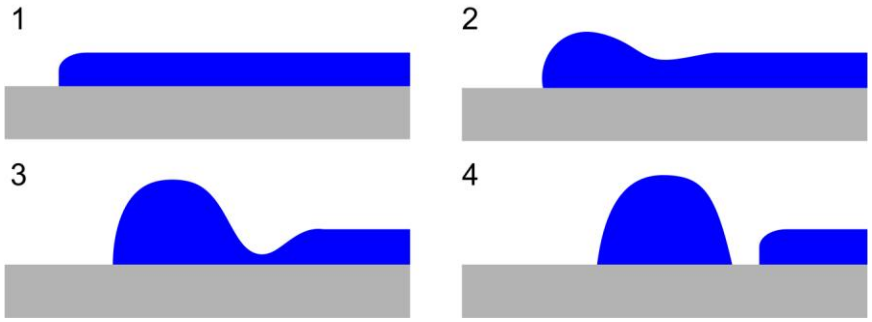

Figure 1-9. Schematic illustration of the pinch-off process.

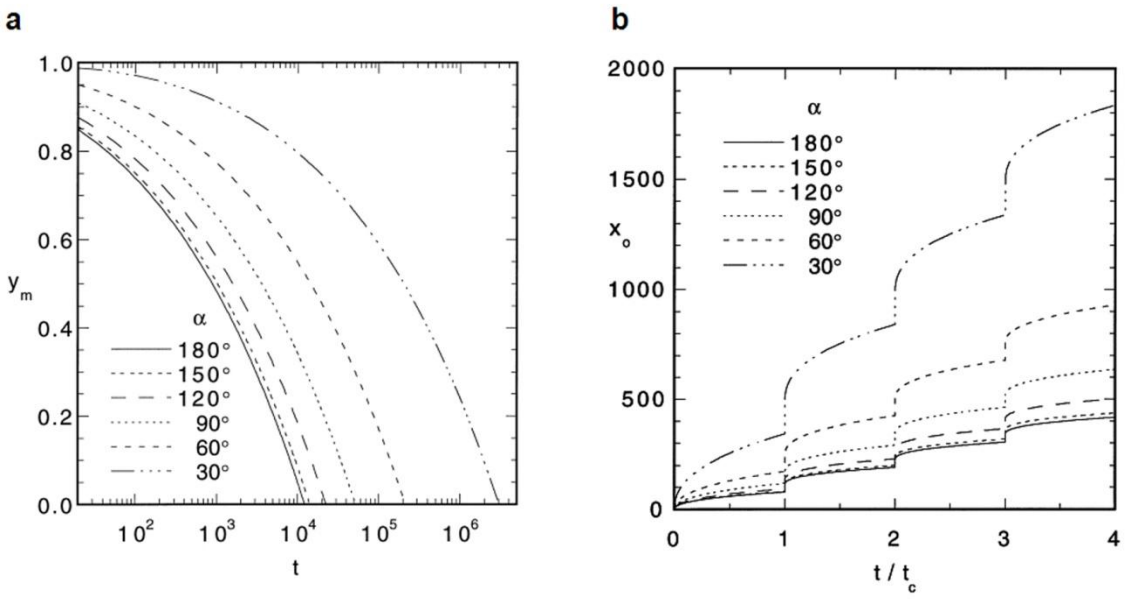

Figure 1-10. Numerical results for the valley deepening and edge retraction rates during the mass shedding process for various equilibrium contact angles at three-phase lines. (a) The minimum height of valleys from the substrate surface versus time. (b) The contact line position versus normalized time for the first four periods of mass shedding. t_c is the time at which valleys reach the substrate surface for the first time. [11]

For the case of films with a finite initial width, it has been shown by Dornel et al. [12] that the pinch-off process can lead to formation of a different number of agglomerates, and that the number of agglomerates depends on several parameters such

as the thickness-to-width ratio of the film, the equilibrium contact angle at the three-phase boundaries, and the anisotropy of the surface energy. Plots of Fig. 1-11 show the effect of these parameters on the number of agglomerates. As seen in this figure, pinch-off is favored as the thickness-to-width ratio of the film becomes higher and the equilibrium contact angle becomes larger, which can also result in a larger number of agglomerates. The effect of the anisotropy of the surface energy can be seen in comparing the number of agglomerates in Figs. 1-11(a) and 1-11(b) (The functional form of the surface energy was taken $\gamma(\theta)=1+0.01332\cos(8\theta-\pi)$, where θ is the angle that the film surface makes with the substrate surface). Anisotropy of the surface energy shifts the criteria for pinch-off. Dornel et al. investigated the effect of surface energy anisotropy with different functional forms and showed that the pinch-off is favored when the surface energy of the top film surface is higher.

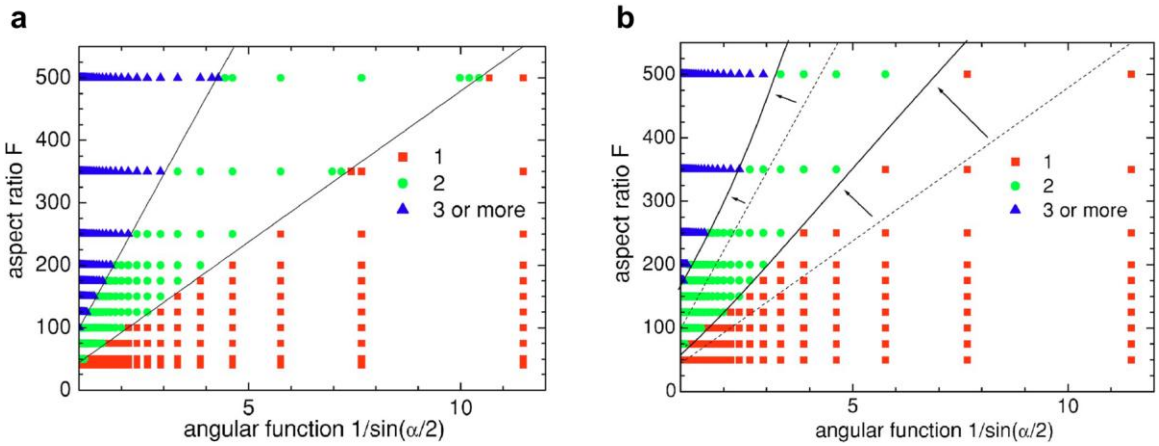

Figure 1-11. Numerical results for the number of agglomerates that form during dewetting of films (a) with isotropic surface energy and (b) with anisotropic surface energy ($\gamma(\theta)=1+0.01332\cos(8\theta-\pi)$, where θ is the angle that the film surface makes with the substrate surface). The dashed-lines in (b) indicate the criteria for pinch-off of the film with isotropic surface energy. F and α indicate the thickness-to-width ratio of the film and the equilibrium contact angle at three-phase boundaries respectively. [12]

Kan and Wong numerically modeled the fingering instability that was observed earlier by Jiran and Thompson in detail [13]. They demonstrated that heights of thickened rims are perturbed as seen in Fig. 1-12, and that the perturbation of a particular wavelength λ_m grows fastest. The particular wavelength λ_m was found to be proportional to the initial film thickness. The growth of the perturbation subsequently leads to faster edge retraction through thinner parts of the perturbed thickened rims and formation of long lines in-between the fast retracting fingerlike edges. They showed that their calculated value of λ_m is in agreement with spacing between adjacent fingers measured in Jiran and Thompson's experiment.

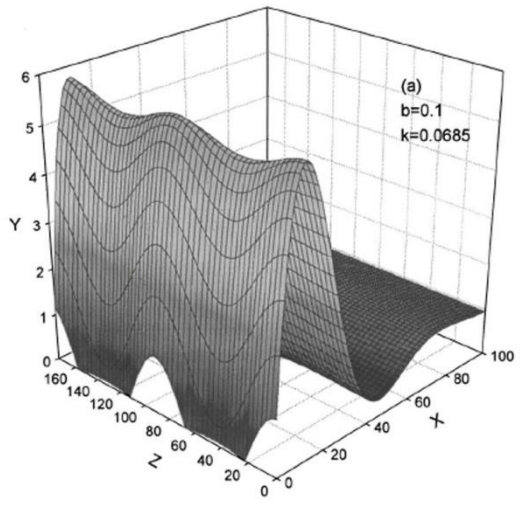

Figure 1-12. Numerical results showing a perturbation on a thickened rim. This perturbation causes fingers with a characteristic spacing to form along the edge. [13]

Both the mass shedding process and a fingering instability lead to formation of long lines during dewetting of thin films. It has been demonstrated that solid or liquid cylindrical bodies that are subjected to longitudinal perturbations that have longer wavelengths than their circumference will eventually break up into arrays of spheres [14]. This instability of a cylindrical body is called the Rayleigh instability. Srolovitz and Thompson showed that thin film lines on rigid substrates are also unstable with respect to arrays of islands that have spacing larger than a critical value by calculating the energy change associated with island formation [15]. McCallum et al. [16] examined the morphological stability of an infinite line on a rigid substrate via linear stability analysis and found that axial perturbation of a line grows and causes the line to break into isolated islands for nonzero contact angle at the three-phase line. Due to the Rayleigh-like instability, the long lines formed by either the mass shedding process or a fingering instability decay into arrays of isolated islands to further reduce the total interfacial energy of the system. It has been reported by Cahn [17] that the anisotropy of surface energy affects the Rayleigh instability of a single crystal cylindrical solid. Cahn analyzed the effect of the anisotropy of surface energy on the critical wavelength for the Rayleigh instability under the assumption that the surface energy depends only on the angle that the surface makes with the z-axis of the cylinder. His analysis demonstrated that the critical wavelength is proportional to the value of $\left(1+\frac{1}{\gamma_s}\left(\frac{\partial^2\gamma_s}{\partial\varphi^2}\right)\right)^{1/2}$, where γ_s is the surface energy of the cylinder and φ is the angle that surface makes with the z-axis of the cylinder.

1.4 Formation of ordered structures via solid-state dewetting

Dewetting of flat continuous films eventually leads to formation of isolated islands through the series of kinetic processes discussed in the previous section. Many experimental results for solid-state dewetting [8-10, 18-25] show that dewetting generally leads to disordered arrays of islands (e.g. dewetting morphologies seen in Figs. 1-6 and 1-7). The irregularities of dewetting morphologies have limited the application of solid-state thin film dewetting for fabrication of ordered structures.

However, in recent years it has been reported that solid-state dewetting of thin films under geometric or crystallographic constraints can lead to formation of ordered structures. Geometric constraints can be imposed by depositing films on pre-patterned substrates with regular topography. In this case, a variance in surface curvature develops in specific directions and guides dewetting to form ordered structures. Crystallographic constraints are imposed on dewetting processes in single crystal films. During dewetting of single crystal films, holes are constrained by crystallographic symmetry to form crystallographically aligned island morphologies. In this section, we will review the literature on the formation of ordered structures through controlled dewetting.

1.4.1 Template-assisted dewetting

Template-assisted solid-state dewetting was first studied by Giermann and Thompson [26, 27]. They modulated the surface curvature of gold films by depositing the films on oxidized silicon substrates templated with square arrays of inverted pyramidal

pits. The modulation of the surface curvature controlled the initiation of dewetting and resulted in the formation of ordered arrays of particles. They found that the gold films dewet to form ordered arrays of single gold particle per pit for specific relative values of the film thickness and the geometric length scales of the pyramidal pits (see Fig. 1-13(a)) [28] . In addition, they showed that gold particles were crystallographically aligned as seen in Fig.1-13(b). As seen in this figure, the particles in pits had a (100) out-of-plane orientation and a near-uniform in-plane orientation. Giermann and Thompson found that this specific crystallographic alignment of particles is the result of the surface energy anisotropy of gold and geometry of pyramidal pits, by observing faceted shapes of the gold particles. Following this pioneering work, formation of ordered structures via template-assisted dewetting has been demonstrated for other film materials [29] and templates with other geometries [30, 31].

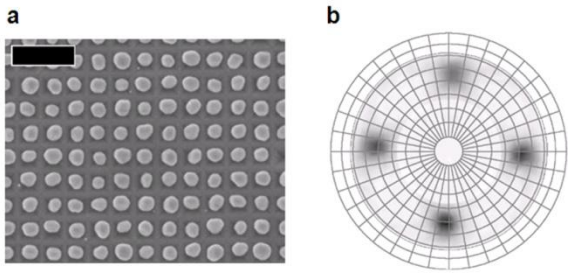

Figure 1-13. Formation of ordered arrays of crystallographically aligned gold nanoparticles via template-assisted solid-state dewetting. (a) SEM image of ordered arrays of single particles in each pit. Scale bar, 500 nm. (b) Pole figure x-ray diffraction pattern for the ordered arrays of gold particles. [26]

1.4.2 Dewetting of single crystal films

Solid-state dewetting of single crystal films has been studied in recent years, mostly for single crystal silicon-on-insulator (SOI) films [6, 12, 32-40]. Unlike polycrystalline films, dewetting morphologies of SOI films show regular characteristics in terms of size, spacing, and alignment of dewetted islands, as well as in the shapes of holes. Regular dewetting morphologies of SOI films were first observed by Ono et al [32]. They annealed (100) and (111) SOI films in ultra high vacuum and observed morphological evolution of films during dewetting. Holes were found to grow by accumulating material at thickening rims and the holes were found to have anisotropic shapes that depended on crystallographic orientations of films. Holes had square shapes in (100) SOI films while they had hexagonal shapes with three-fold symmetry in (111) SOI films. The edges of these holes were aligned along specific crystallographic directions in which thickening rims expose low surface energy facets of Si, such as {111} and {311} facets.

Nuryadi et al. [33, 34] also studied dewetting of (100) SOI films and showed that flat films evolved into ordered arrays of fingers and isolated islands, as shown in Fig. 1-14. As seen in the figure, finger-like hole edges were observed to propagate along the <310> directions and this resulted in formation of fingers and isolated islands aligned along the <310> directions. They also found that the islands were bound by {311} and {111} sidewall facets and {100} top facets. Formation of ordered arrays of islands or fingers (wires) that have {311} or {111} facets was also observed during dewetting of (111) and (110) SOI thin films [35, 36]. These results for SOI dewetting suggest that

specific regular morphologies of dewetting SOI films were associated with surface energy anisotropy of Si.

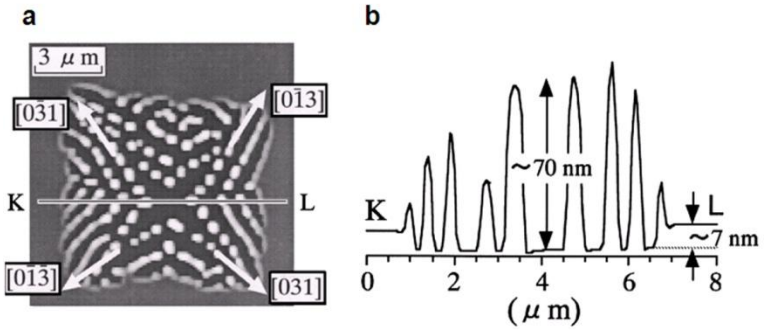

Figure 1-14. Formation of ordered arrays of fingers and islands during dewetting of a (100) SOI film. (a) AFM image of a hole in a dewetting 7nm-thick (100)-bonded SOI film. Annealing was carried out at 950°C for 10 seconds in UHV. (b) AFM height profile along line K-L in (a). [33]

Kinetic mechanisms underlying regular dewetting morphologies of SOI films have been studied [6, 12, 37], and it has been demonstrated that morphological evolution occurred through kinetic processes similar to those described for isotropic films (e.g. finger formation due to uneven accumulation of material, mass shedding processes, and island formation due to Rayleigh-like instability. See section 1.2). It was also found that surface energy anisotropy of Si placed crystallographic constraints on these kinetic processes, leading to formation of regular dewetting morphologies.

Ishikawa et al. [38-40] investigated the effect of patterning on dewetting morphologies of (100) SOI films and found that the alignment direction of dewetted islands can be controlled to be parallel to edges of patterns for line patterns having a width of 0.3~0.5 μm and the thickness of ~3 nm, as shown in Fig. 1-15. They showed

that such an alignment of dewetted islands requires a narrow line width for which nucleation and growth of holes inside of lines rarely occur.

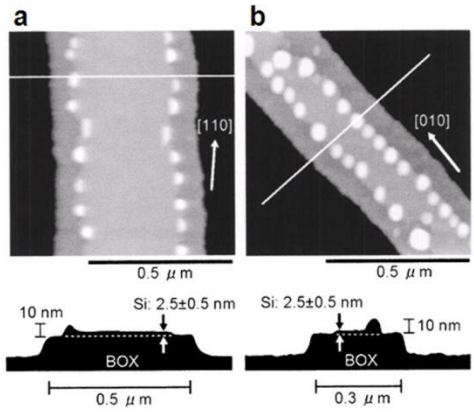

Figure 1-15. Alignment of dewetted islands along edges of long line patterns. Long lines were patterned from (100) SOI films. SEM images of aligned islands and height profiles for long line patterns that were nearly parallel to the (a) [110] and (b) [010] directions. Height profiles were measured along the white lines in the SEM images. [40]

As shown in the results of SOI dewetting, solid-state dewetting of single crystal thin films can also be used as a process for producing ordered structures. The ordering obtained via this process has not yet been observed to be as precise as that obtained via template-assisted dewetting seen in the previous section. However, dewetting of single crystal films can have advantages over template-assisted dewetting in terms of crystallographic alignment of dewetted structures and the ability to produce complex structures. To exploit these advantages and improve the quality of ordering, it is important to develop mechanistic understandings through which we can predict morphological evolution during dewetting of single crystal films.

1.5 Scope of work

The goal of this work is to improve the understanding of the mechanisms underlying regular morphological characteristics of dewetting single crystal films and to demonstrate the potential of solid-state dewetting of single crystal films as a self-assembly method. To achieve the goal, we studied morphological evolution during dewetting of as-deposited and patterned single crystal Ni films. Single crystal Ni films were epitaxially grown on single crystal MgO substrates.

In chapter 2, we review experimental methods used in this work, including epitaxial thin film growth, x-ray texture analysis, film patterning, thermal annealing, and microscopy.

In chapter 3, we report observations of specific in-plane faceted shapes of growing natural holes that depend strongly on the crystallographic orientation of the Ni films, as well as on the annealing ambient. During the early stage of hole growth, natural holes maintain their simple in-plane faceted shapes. By analyzing the anisotropy of the edge retraction velocity and faceting of edges, we characterize the effects of surface energy anisotropy on specific shapes of natural holes.

In chapter 4, we present results for late-stage dewetting of single crystal Ni films and discuss kinetic mechanisms underlying complex hole shapes and island morphologies observed in the late stage of dewetting. By tracking morphological evolution of individual natural holes, we show that corner-induced instabilities, pinch-off, fingering instabilities, and Rayleigh-like instabilities lead to the formation of complex dewetting morphologies.

In chapter 5 we focus on pinch-off behaviors observed during dewetting of square, cross, long-line patches patterned from single crystal Ni films. These patches evolved to regular shapes with increased complexity through retraction and pinch-off of edges during dewetting. By analyzing morphological evolution of the patches, we show the effect of the initial patch geometry and surface energy anisotropy on the pinch-off process. Numerical simulations are also carried out to study these effects.

In chapter 6, we demonstrate regular pattern formation with various shapes via dewetting of patches with different initial shapes and crystallographic alignments. We also further develop mechanistic understandings of regular pattern formation through dewetting of single crystal films described in previous chapters. Results and findings in this chapter show the potential of solid-state dewetting of single crystal films as a self-assembly method.

In chapter 7, we summarize the results of this work and propose future work on solid-state dewetting of single crystal thin films.

Chapter 2

Experimental Methods

2.1 Film Deposition

Single crystal Ni films used in this study were deposited on one-side of epi-polished single crystal MgO substrates (purchased from MTI Corporation) using a Balzers UMS500 electron-beam evaporation system. Ni on MgO was selected as a model system for our study of single crystal thin film dewetting since it has been demonstrated in the literature [41-46] that Ni films of different crystallographic orientations can be grown epitaxially on MgO substrates. The Balzers UMS500 electron-beam evaporator is equipped with a turbo pump, a rotary vane pump, and a catalyzer trap that prevents back-streaming of hydrocarbons on the rotary vane vacuum pumps by burning hydrocarbons in the fore vacuum line. Because the system does not have a load-lock, the main chamber is exposed to atmosphere when samples are loaded. Therefore, a bake-out process is necessary to desorb gases from chamber walls and reach a high vacuum. The bake-out process is started after the chamber pressure reaches the range of low 10^{-5} Torr. The chamber pressure is measured using a hot tungsten filament ion gauge. During the bake-out process, the chamber was baked overnight at 120°C for about 24 hours using a radiant heater integrated into the system. The bake-out temperature is limited by the maximum operating temperature (130°C) of a quartz crystal sensor used for monitoring

the film thickness (right angle single sensor, purchased from INFICON). During the bake-out process, a sample stage mounted to the top of the chamber was further heated to a higher temperature of around 320°C using a home-built tungsten heater. The temperature of the stage was measured using a K-type thermocouple. Heating of the sample stage prevents desorbed gases from being re-adsorbed on the surfaces of the substrates during the bake-out process. After the bake-out process, a preliminary evaporation was carried out to degas the source material contained in a FireRite crucible. During the preliminary evaporation process, the temperatures of the chamber and sample stage were set at 90°C (below a boiling point of water) and about 280°C respectively. The chamber and sample stage were still heated to the elevated temperatures during the degassing process to prevent re-adsorption of gases on the chamber wall and the surfaces of the substrates. The deposition was carried out after cooling down the sample stage and chamber overnight to room temperature. The base pressure was between mid 10^{-8} Torr and high 10^{-8} Torr and the pressure varied between low 10^{-7} Torr and mid 10^{-7} Torr during deposition. The deposition rate that was monitored using a quartz crystal monitor was about 0.5 Å/s. The film thickness was controlled by manually opening and closing a shutter located in front of the sample stage during evaporation of source material.

2.2 X-ray Texture Analysis

Crystallographic orientations of as-deposited and dewetted Ni films were measured using X-ray diffraction (XRD). Theta-2theta scans were performed on a Rigaku

RU300 diffractometer to measure the out-of-plane orientations of the films. In the case of single crystal Ni films, the diffraction data shows a strong peak for Ni at a particular value of 2θ, $2\theta_{peak}$. Pole figure and high resolution X-ray texture analyses were then carried out using a Bruker D8 Discover system to determine both out-of-plane and in-plane crystallographic alignments of the films with respect to the single crystal MgO substrates. The Bruker D8 Discover system was equipped with a 2-D area detector [47] and a high resolution detector. Pole figure measurements were made using a copper tube x-ray generator, a 0.5 mm-diameter spot collimator, and a 2-D area detector. A schematic illustration for Pole figure XRD measurements is shown in Fig. 2-1.

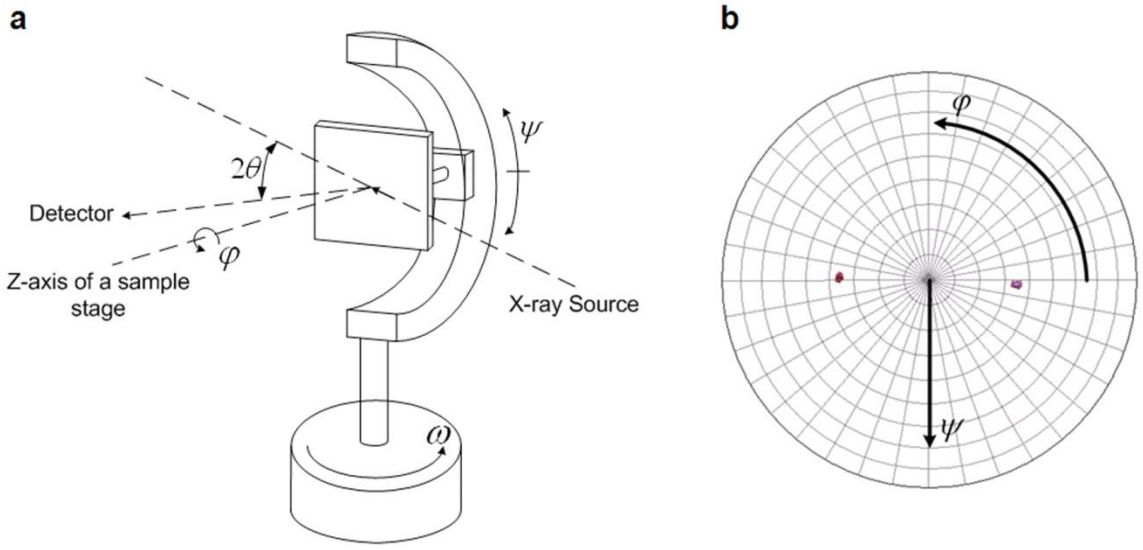

Figure 2-1. Schematic illustration of the pole figure XRD geometry. (a) Goniometer and sample stage. Important angles are indicated in the illustration. (b) Example of an x-ray diffraction pattern in an equal area net. Rotation angles are indicated in the equal area net.

Before collecting pole figure data, a preliminary scan was made with the area detector centered at $2\theta \sim 2\theta_{peak}$, setting $\psi=0^{\circ}$, and rotating a sample about the φ-axis to check if the surface normal of a sample was reasonably well-aligned to the z-axis of the sample stage. After the preliminary scan, pole figure data were collected with the area detector centered at $2\theta=88^{\circ}$ and rotating a sample about the φ-axis and ψ-axis. By centering the detector at $2\theta=88^{\circ}$, diffraction data for $73^{\circ} < 2\theta < 103^{\circ}$ could be collected because the area detector can collect data for $2\theta \pm 15^{o}$ simultaneously. The 2θ values of the strongest (111) and (311) peaks are between 73° and 103° for both Ni and MgO. Therefore, in-plane crystallographic alignment of Ni films with respect to MgO substrates could be measured by comparing (111) or (311) pole figures of Ni to those of MgO.

High resolution XRD measurements were made using a copper tube x-ray generator, a Ge(022) 4-bounce monochromator, and a LynxEye high resolution detector in 0-dimensional mode. A schematic illustration of the configuration for high-resolution XRD measurements is shown in Fig. 2-2. Before collecting high resolution XRD data for Ni films, a series of detector scans (changing 2theta), rocking curve scans (changing omega), 2theta-omega scans (changing both 2theta and omega), and chi scans (changing the tilt angle of a sample) were carried out for sample alignment. Through the sample alignment procedure, we optimized the values of Z (the sample location in the direction of the sample surface normal), omega, 2theta, and chi. The value of Z is optimized to focus the X-ray beam on the sample surface. The values of omega, 2theta, and chi are optimized to obtain the maximum intensity of the x-ray beam diffracted from the MgO substrate. The optimized values of 2theta and omega were recorded for the calculation of

the tilt angle between the MgO substrate and the Ni film. After finishing the sample alignment, the data for Ni film were collected by making a rocking curve scan and a 2theta-omega scan. As illustrated in Fig. 2-2, the tilt angles between the surface normal and {hkl} plane normals were calculated by subtracting the value of θ (collected from a 2θ-ω scan) from the value of ω (collected from a rocking curve scan) for both the MgO substrate and Ni film. The angles between {hkl} planes of the Ni film and MgO substrate were obtained by calculating the difference in the tilt angle for the MgO substrate and Ni film.

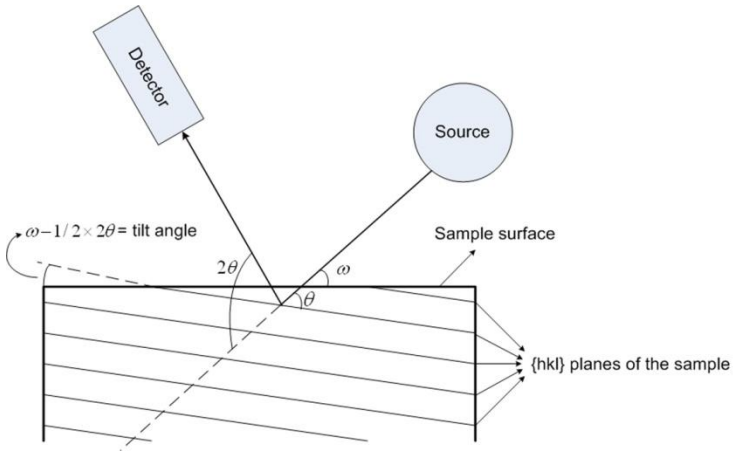

Figure 2-2. Schematic illustration of a 2θ-ω scan. This scan determines the value of 2θ seen in the figure. The value of ω seen in the figure is obtained from a rocking curve scan. The tilt angle between the substrate and film can be calculated using these values as shown in the illustration.

2.3 Film patterning

Film patterning in this work was mostly carried out using contact photolithography followed by wet etching of Ni. Samples were dehydrated at 110°C for about 5 minutes on a hot plate before coating with photoresist. The samples were then spin-coated with OCG825 positive photoresist at a spin rate of 3000 rpm for 30 seconds and then baked at 110°C for 5 minutes on a hot plate to evaporate solvents from the photoresist. After the bake, samples were brought into contact with the mask and aligned to mask patterns using a mask aligner. Samples were then exposed to UV light. After exposure, the photoresist was developed in OCG934 1:1 developer and then samples were baked at 130°C for 5 minutes on a hot plate. After the photolithography process, wet etching of Ni was carried out using an etchant composed of 69% HNO_3, H_2SO_4, CH_3COOH, H_2O with a volume ratio of 7.2:2:5:28. Samples were then ultra-sonicated in photoresist remover (RR4, Futurrex, Inc) to strip the photoresist.

2.4 Thermal Annealing

As-deposited and pre-patterned Ni films were annealed at sufficiently high temperatures (typically 900°C in this work) in quartz tube furnaces to induce dewetting of the films. Reducing gas (5% H_2 and 95% N_2, purchased from Airgas, Inc.) was flowed through the quartz tube during annealing to prevent oxidation of the films (Nickel oxide can be reduced by hydrogen because the free energy change of the oxidation reaction is more negative for hydrogen than for nickel unless the temperature is much less than 0°C

[48].) Two different tube furnaces were used in this work, a Lindberg/Blue Mini-Mite model and a Transtemp model. Stainless steel tubes were used as gas flow tubes and connected to a quartz tube using vacuum flanges in the Lindberg/Blue Mini-Mite model while rubber gas flow tubes were used and clamped using screw clamps in the Transtemp model. The temperature in the quartz tubes was calibrated with a K-type thermocouple, and the flow rate of reducing gas was controlled during annealing. The flow rate was measured using rotameters installed between the gas inlet of the furnace and the gas bottle. The maximum flow rate of reducing gas was much more limited in the Transtemp model than in the Lindberg/Blue Mini-Mite model because heated reducing gas burns the rubber tubes at the gas outlet. Accordingly, annealing at a high flow rate (e.g. 2310 standard cubic centimeters per minute (sccm)) was carried out only in the Lindberg/Blue Mini-Mite model.

2.5 Atomic Force Microscopy and Scanning Electron Microscopy

Morphologies of samples were mostly characterized using atomic force microscopy (AFM) and scanning electron microscopy (SEM). AFM imaging was done in tapping mode using a Veeco Nanoscope IV AFM. AFM probes were standard tapping mode silicon probes (RTESP model, purchased from Veeco Probes). Most AFM imaging was carried out periodically to track morphological evolution of specific features during dewetting. Low resolution scans were done before taking high resolution images, to locate an AFM tip on top of specific locations. After finding specific features, high-

resolution images of the specific features were obtained, typically at a scan rate of 0.2~0.3 Hz. At higher scan rates, trace and retrace images of tall and steep features become significantly different.

SEM imaging was carried out mostly using an FEI/Philips XL30 FEG ESEM. The exposed MgO surface of dewetted samples became charged during SEM imaging. Charging occurred because excessive electrons remained on the insulating MgO surface instead of penetrating the samples to reach the microscope's electrical ground. Reducing the accelerating voltage and spot size helped reduce charging effects in normal vacuum mode, but low vacuum operation of the ESEM reduced the charging effect more significantly. In low vacuum mode, water vapor was introduced into the specimen chamber during operation. Water molecules are positively ionized due to collisions with secondary electrons. Water ions are forced to move toward the negatively charged sample surface by the electric field between the detector and the sample. Sample surfaces are neutralized by these water ions, thereby reducing charging effect. Increasing water vapor pressure reduced image resolution as well as charging effects. In this work, the water vapor pressure during imaging was 0.8~1.2 Torr, at which reasonably good images could be taken.

Chapter 3

Anisotropic edge retraction and hole growth

3.1 Introduction

As mentioned in chapter 1, dewetting of a thin film occurs through the nucleation and growth of holes that reach the substrate surface. In polycrystalline thin films, holes penetrate the film to reach the substrate surface via grooving at grain boundary triple junctions. The holes then grow and develop a thickened rim due to a local surface curvature gradient at their edges, and as the rim thickens, the net curvature is reduced and edge retraction slows down. Due to the lack of uniform crystalline symmetry in polycrystalline films, the holes do not propagate in a regular way and this leads to irregular island morphologies of dewetted films.

As discussed in chapter 1, it has been recently reported that dewetting of single-crystal silicon films in silicon-on-insulator (SOI) structures can produce specific ordered morphologies that depend on the crystallographic orientation of the film. The underlying physics behind this phenomenon has been studied from both energetic and kinetic points of view. These studies show the possibility of purposely guiding dewetting to produce specific regular structures. To realize this potential and obtain precise control over regular structures produced by dewetting, it is important to develop an improved understanding of the underlying physics.

In this chapter, we report studies of the regular morphological characteristics of growing natural holes and pre-patterned retracting edges in 120 nm-thick single crystal Ni(100) and Ni(110) thin films on MgO(100) and MgO(110) substrates. We characterize the effects of anisotropic surface energy and surface diffusion on the specific morphologies of dewetting films by analyzing the anisotropy of edge retraction velocities and the dependence of shapes of natural holes on the annealing ambient. The mechanistic understanding of edge retraction provided through this chapter will provide a basis for understanding the evolution of complex morphologies that result from solid-state dewetting of unpatterned single crystal films.

3.2 Experimental

120 nm-thick single crystal Ni(100) and Ni(110) films were deposited on MgO(100) and MgO(110) substrates. 99.995% pure Ni pellets purchased from Kurt J. Lesker were used as the source material. After the depositions, some of as-deposited films were patterned into polar arrays of 45 μm X 90 μm rectangular patches via photolithography followed by wet etching of Ni. Both the as-deposited films and pre-patterned films were annealed in a tube furnace at 900°C with flowing reducing gas (5% H2 and 95% N2). We carried out separate experiments at two different reducing gas flow rates, 2310 sccm and 12 sccm. We observed the results of morphological evolution of the films using SEM and AFM. The AFM imaging was carried out in tapping mode using a Veeco Nanoscope IV AFM. The AFM images were then analyzed using WSxM software developed by Nanotec Electronica [49]. The SEM images were taken using an FEI/Philips XL30 FEG ESEM. Cross-sectional TEM sample preparation in this work was carried out via an in-situ lift-out process [50] in an FEI DualBeam 235 FIB system, and the TEM images were taken using a JEOL 200CX TEM. As discussed in chapter 2, out-of plane orientations of Ni films were measured using theta-2theta scans with a Rigaku RU300 diffractometer. To measure the crystallographic alignments of the nickel films with MgO substrates, pole figure XRD and high-resolution XRD measurements were made using a Bruker D8 Discover system with an area detector and a high resolution XRD detector.

3.3 Results and Discussion

Figure 3-1 shows results of XRD measurements for as-deposited Ni (100) and Ni(110) films. As seen in the figure, Ni films are crystallographically aligned with both out-of-plane and in-plane orientations of the MgO substrates. Since the Ni films were grown as single crystal films, the crystallographic orientations of features observed in dewetting films can be readily determined.

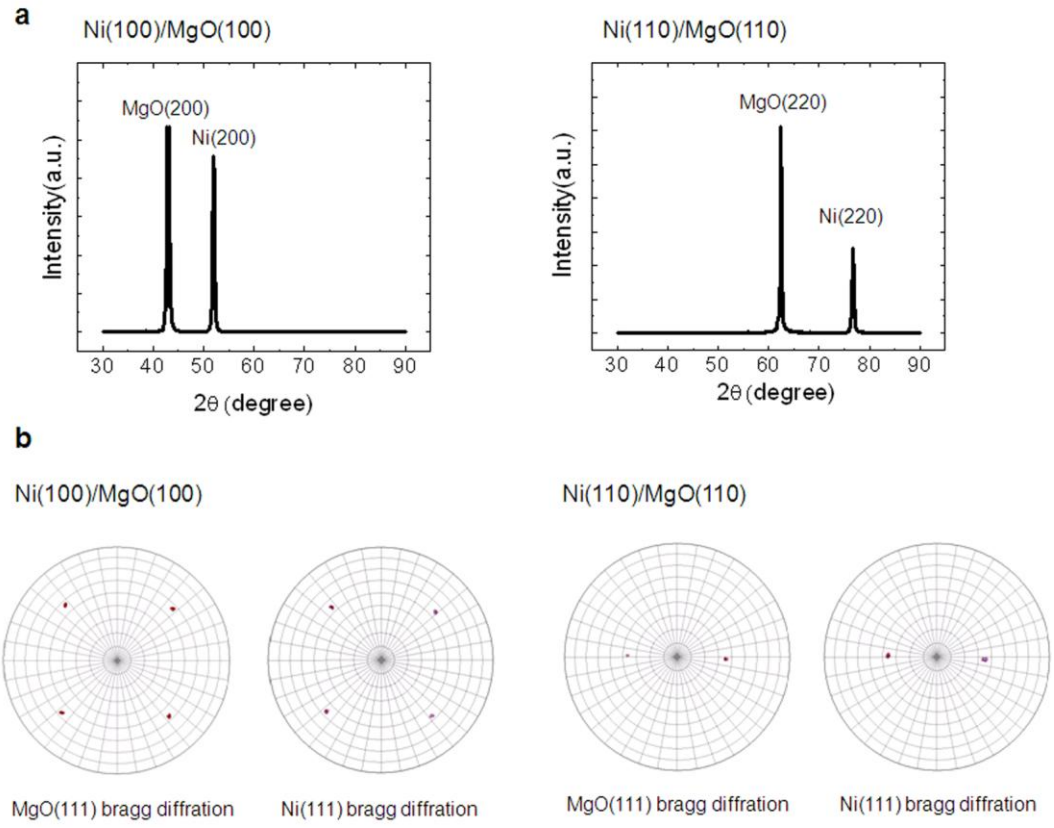

Figure 3-1. XRD patterns for 120nm-thick Ni(100) and Ni(110) films. (a) Theta-2theta patterns. (b) Pole figure XRD patterns. Out-of-plane orientations of Ni films and MgO substrates are indicated in the patterns.

Morphological evolution of the single crystal Ni films begins with the nucleation and growth of holes that have specific shapes that strongly depend on the film orientation and annealing ambient, as seen in Fig. 3-2. As seen in this figure, there is local accumulation of material near the edges of growing holes. Accumulation of material near the edges indicates that the mass transport mechanism for the hole growth is surface diffusion rather than evaporation and condensation. The holes grow as Ni diffuses from the three-phase lines at their edges to the flat film surface, due to a gradient in the local surface curvature, and thickened rims develop around the holes. During their initial growth, natural holes are bound by straight edges that are perpendicular to specific crystallographic directions. In Ni(100) films, edges of natural holes are initially perpendicular to the <011> directions when a reducing gas flow rate of 2310 sccm was used, but they are perpendicular to the <001> directions at a reducing gas flow rate of 12 sccm (see Figs. 3-2(a)-3-2(d)). In Ni(110) films, natural holes are bound by two edges perpendicular to the <001> directions and two other edges perpendicular to the <110> directions for both flow rates. However, the holes grow faster in the <110> directions at 2310 sccm, but in the <001> directions at 12 sccm (see Figs. 3-2(e)-3-2(h)). Figure 3-3 shows the rim shape of the longest edge of a natural hole, which has the same shape as the natural hole shown in Fig. 3-2(h). As seen in the figure, the thickened rim is composed of {hk0} facets such as {100}, {210}, and {410} facet. This shows that the surface energy of nickel is highly anisotropic in this annealing condition. The anisotropy of the surface energy of nickel in different annealing conditions will be discussed later in this chapter.

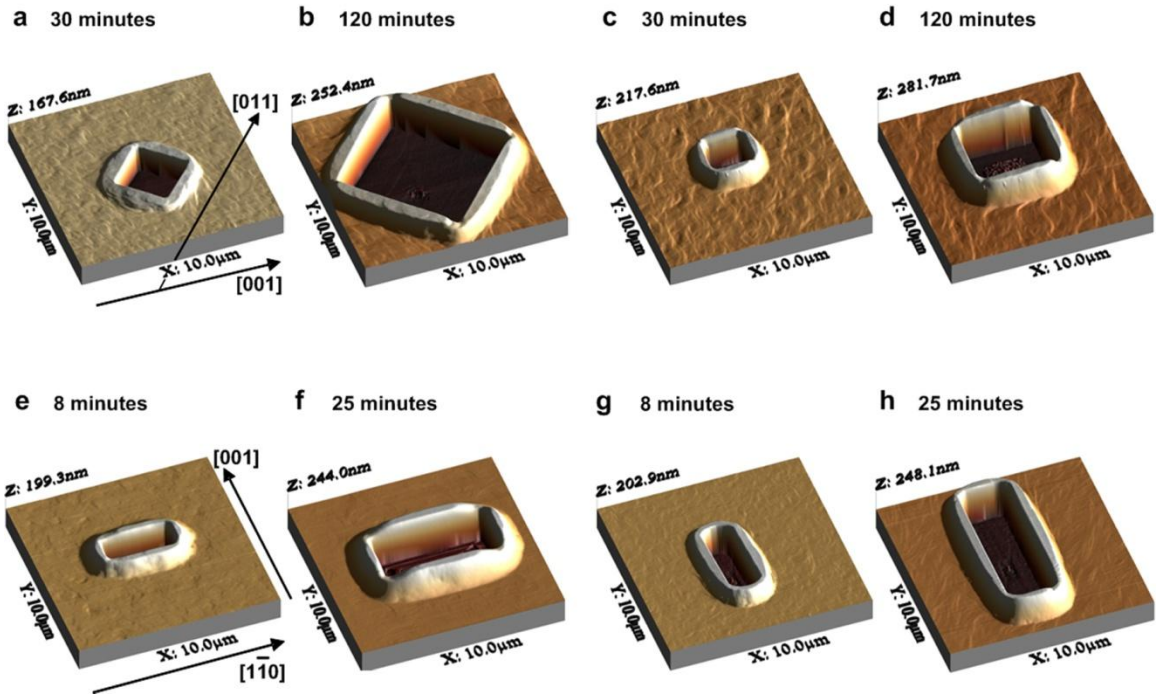

Figure 3-2. Atomic force microscope (AFM) images of growing natural holes in Ni(100) and Ni(110) films at two different reducing gas flow rates. The annealing times are indicated in the images. (a), (b) Ni(100), 2310 sccm. (c), (d) Ni(100), 12 sccm. (e), (f) Ni(110), 2310 sccm. (g), (h) Ni(110), 12 sccm.

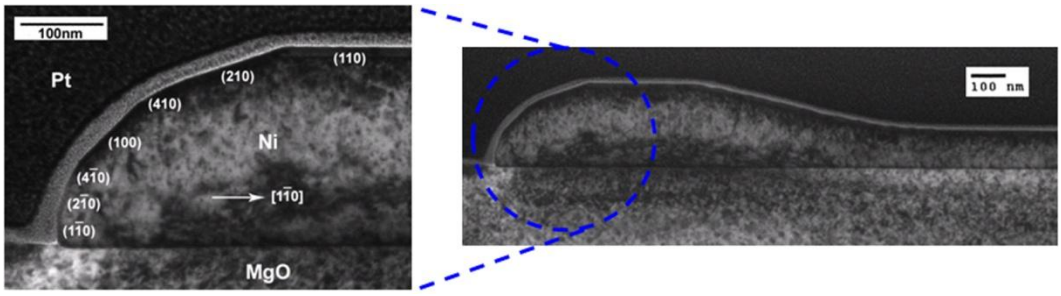

Figure 3-3. TEM images showing the rim shape of the longest edge of a natural hole that has the same shape as the natural hole shown in Fig. 3-2(h) (the longest edge is perpendicular to the $[1\bar{1}0]$ direction in a Ni(110) film).

Anisotropic growth morphologies can be understood in terms of the orientation-dependent growth velocity [51, 52]. The morphologies will have straight interfaces whose normals are parallel to specific directions in which the growth velocity is particularly low. To investigate if the specific shapes of natural holes shown in Fig. 3-2 are associated with variations of the edge retraction velocity for different in-plane retraction directions, we measured the retraction distances of pre-patterned 90 μm-long edges on rectangular patches oriented in various in-plane crystallographic directions (see Fig. 3-4(a)), after annealing at 900°C for 318 minutes. The annealing time is defined as the total annealing time of multiple annealing runs, summing to 30 minutes, 108 minutes, 198 minutes, and 318 minutes. Figures 3-4(b) through 3-4(e) show polar plots for the average retraction distance as a function of the in-plane crystallographic alignment of the initial edge. For each edge, at least 12 edge retraction distance values were measured and averaged. The most remarkable characteristic of the polar plots is the prominent cusps appearing in certain directions. The directions showing these prominent cusps correspond to the directions of the edges in natural holes shown in Fig. 3-2, suggesting that slow edge retraction in these particular directions influences the shape of natural holes.

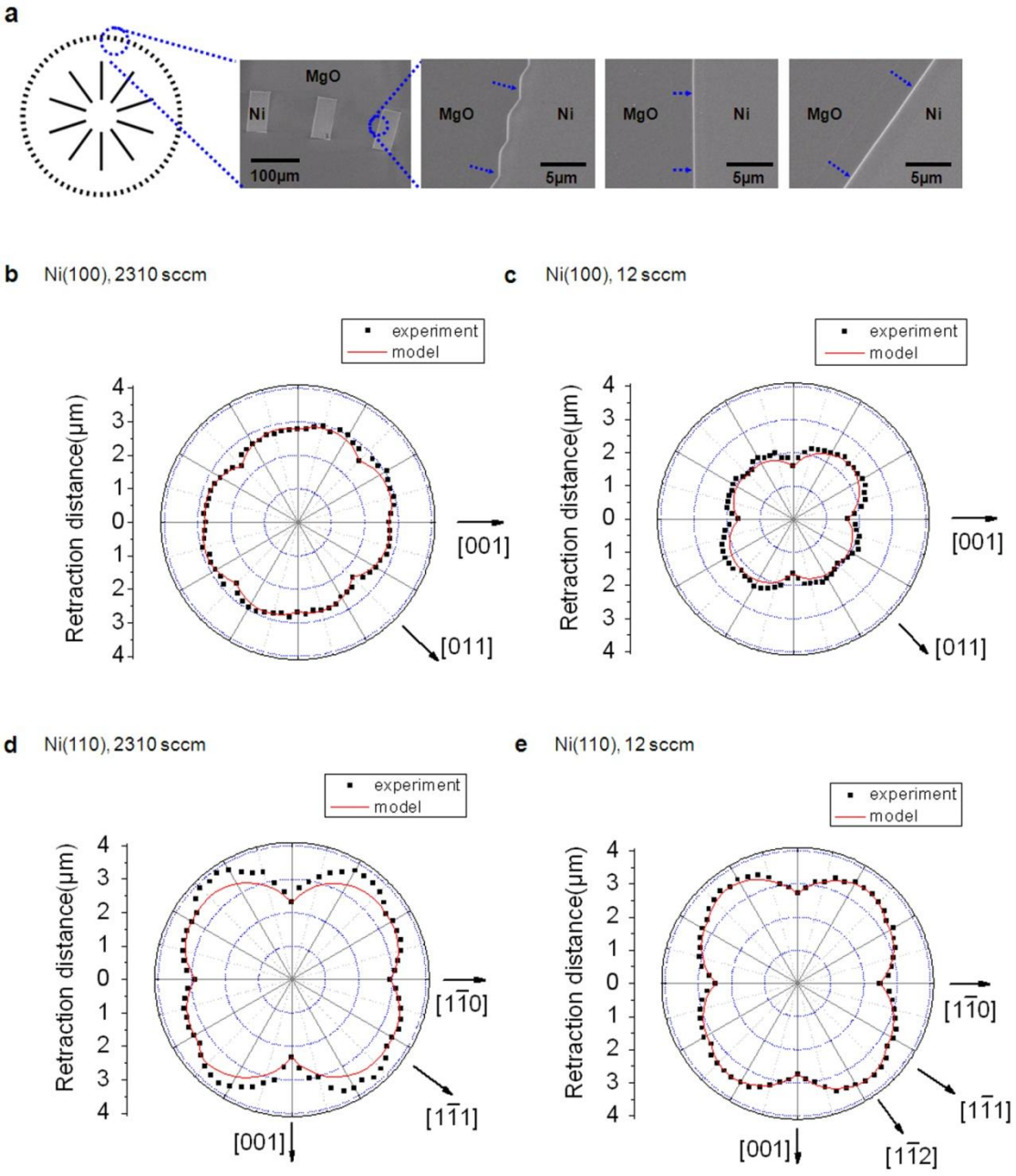

Figure 3-4. Anisotropic edge retraction velocity. (a) Photolithography mask pattern and the patterned islands used to measure the edge retraction velocity. The general faceting behaviors along the edges are also shown in SEM images on the right. (b)-(e) Polar plots of the edge retraction distance after annealing for 318 minutes. The film orientation and the flow rate of reducing gas are indicated in each polar plot.

As seen in Fig. 3-4(a), some edges remain straight as single facets during retraction, while others are unstable as single facets and break up into two alternating facets. The directions in which edges remain stable are indicated in each polar plot of Fig. 3-4. As shown in the figure, certain stable edges with single facets have locally minimum velocities corresponding to cusps in the velocity polar plot. Figure 3-5 shows more examples of edges that break up into alternating facets during retraction. As seen in Figs. 3-4(a) and 3-5, in general, the in-plane orientations of the alternating facets correspond to the in-plane orientations of the two stable edges at the adjacent lowest angles of rotation.

We derived a simple expression for the anisotropic edge retraction velocity based on the faceting behaviors of edges oriented in various in-plane crystallographic directions. Figure 3-6 shows a schematic diagram of a micro-faceted edge that has decomposed into two facets, denoted as facet 1 and facet 2. The retraction velocity of the edge, can be described by

$$V(\theta) = V_1(\cos\theta - \frac{\sin\theta}{\tan\alpha}) + V_2(\frac{\sin\theta}{\sin\alpha}),$$

where V_1 and V_2 are the velocities of the two alternating facets, θ is the angle between the macroscopic in-plane orientation of the edge and the in-plane orientation of facet 1, and α is the acute angle between facet 1 and facet 2. The two facets in this model have the same in-plane orientations as the two stable edges with in-plane normals closest to the retraction direction. We obtain the values of V_1 and V_2 from the measured retraction velocities of the two stable edges at the two nearest angles of rotation, and plot the results as solid lines in the pole plots of Fig. 3-4. The general consistency between this equation

and the data shows that the in-plane orientation-dependent faceting behavior plays a critical role in determining the anisotropic edge retraction velocity.

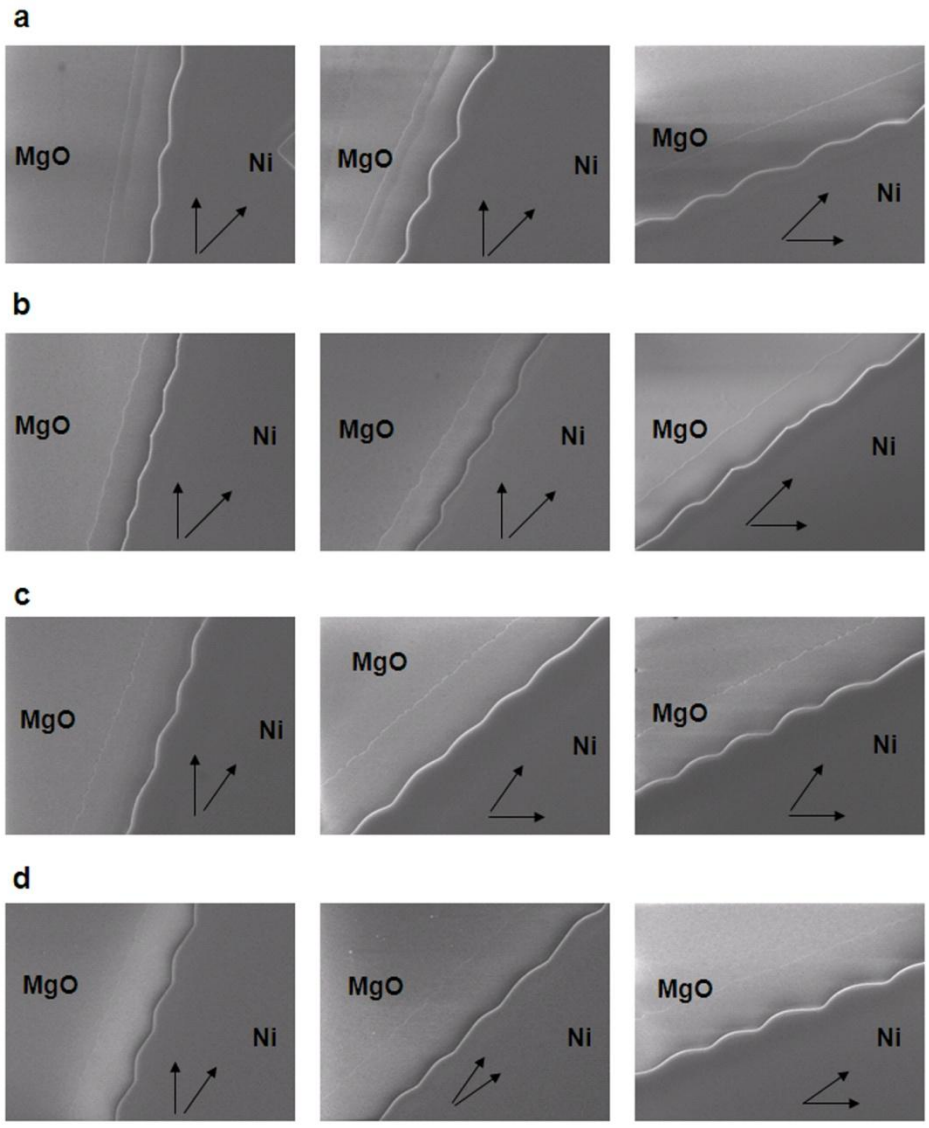

Figure 3-5. Faceting of long retracting edges. (a) Ni(100), 2310 sccm. (b) Ni(100), 12 sccm. (c) Ni(110), 2310 sccm. (d) Ni(110), 12 sccm. The arrows indicate the in-plane orientations of the two stable edges at lowest angles of rotation.

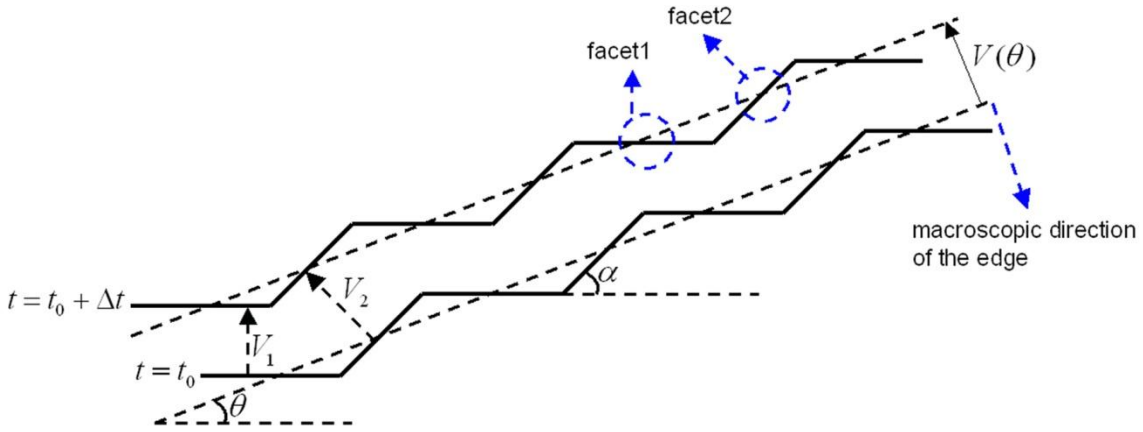

Figure 3-6. Schematic illustration of the retraction of a faceted edge. The dashed lines in the diagram indicate the macroscopic orientation of the edge. The edge retraction velocity can be expressed as the distance between the two dashed lines.

The in-plane orientation-dependent faceting behavior originates from the anisotropy of the Ni surface energy. Due to this anisotropy, facets form at orientations of local energy minima, corresponding to cusps in the γ-plot [53]. In the case of face-centered cubic metals, the orientations of local energy minima generally include low index orientations ({111}, {100}, and {110}). For the case of nickel, it has been reported that there can also be a cusp at {210} in the γ-plot [54, 55]. Because of the crystallographic constraint of surface energy minimization, only a few edges having specific in-plane orientations have a single facet that remains stable during edge retraction. This crystallographic constraint can be seen in Fig. 3-7. Figure 3-7 shows (100) and (110) stereographic projections of {111}, {100}, {110}, and {210} faces of a cubic crystal. The directions in which an edge remains stable as a single facet are also indicated in each stereographic projection (The edges that were initially perpendicular in

the [$1\bar{1}2$] direction of a Ni(110) film were stable only at 12 sccm as indicated in Fig. 3-4(e)). As shown in the figure, there are several poles with the low energy faces along the particular directions of the projections. This indicates that edges oriented in those particular directions can expose the low energy facets along their thickening rims without being decomposed to into alternating in-plane facets, and therefore remain stable during retraction. As mentioned earlier, certain stable edges show prominent cusps in the polar plot of edge retraction velocities. A characteristic in common for these edges is that they can expose either {hk0} facets ({100}, {110}, and {210}) or {hhl} facets ({111}, {110}, and {100}) without evolving to alternating facets. Some of these facets are also observed in the AFM height profiles shown in Figs. 3-8 and 3-9.

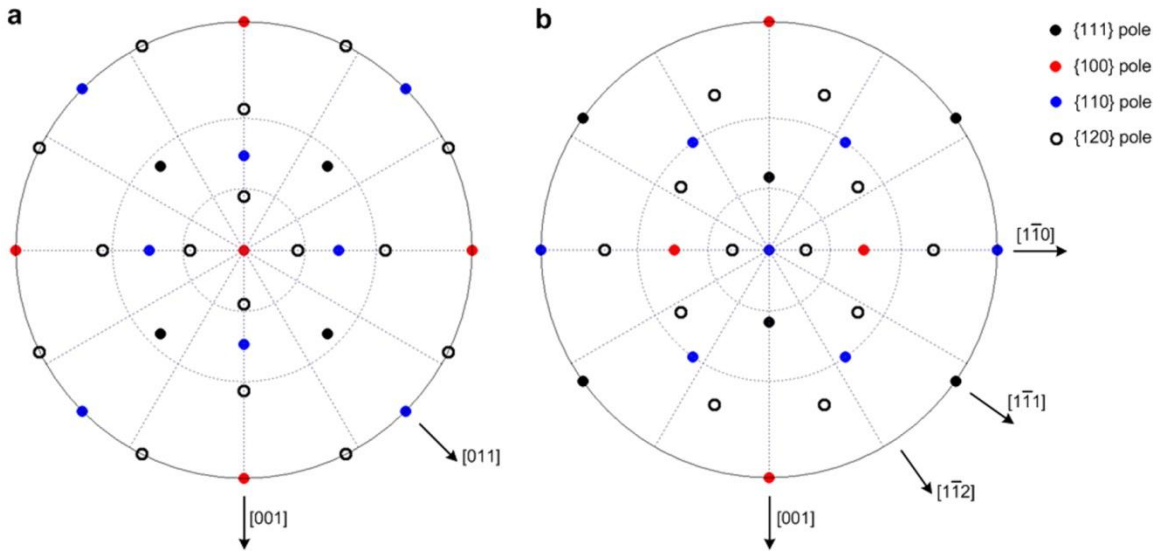

Figure 3-7. Stereographic projection of {111}, {100}, {110}, and {210} faces of a cubic crystal (a) (100) projection. (b) (110) projection. These stereographic projections were plotted using MTEX [56], an open source texture analysis MATLAB code.

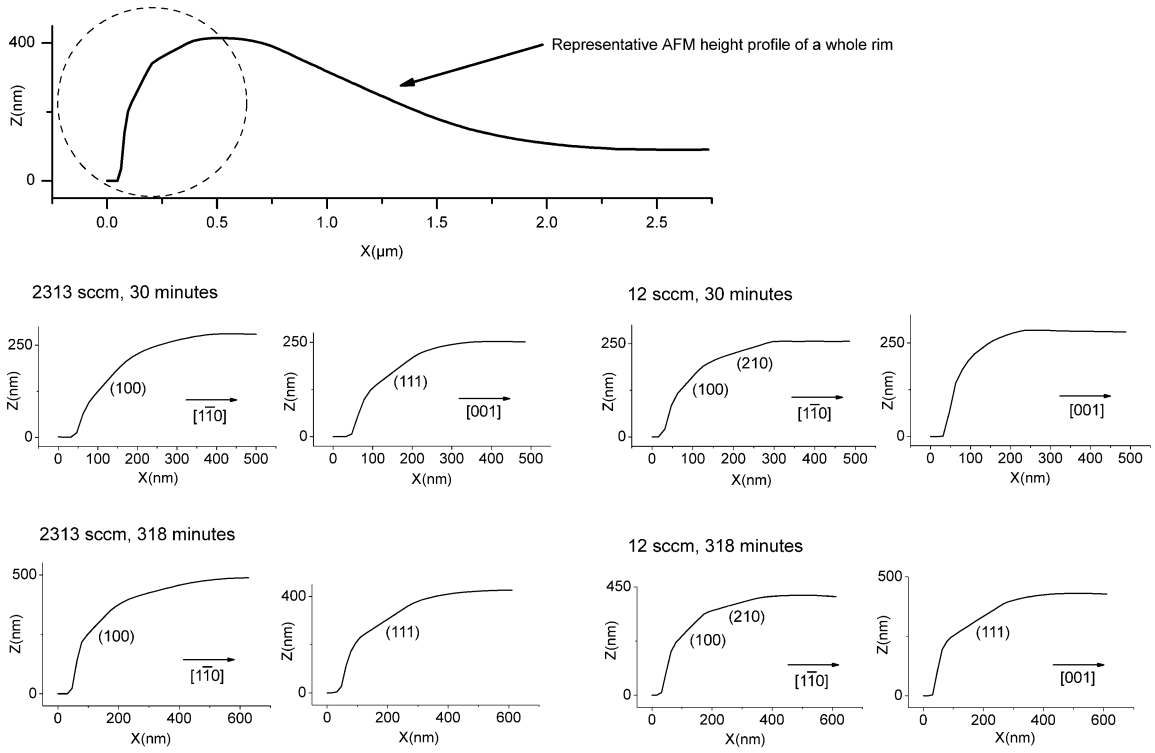

Figure 3-8. AFM height profiles of some stable edges in pre-patterned Ni(110) films. The flow rate of reducing gas, annealing time, and edge retraction directions are indicated in each height profile. There are small errors in measured angles that might be caused by AFM tip artifacts or small deviations of the scan directions from the edge normal directions.

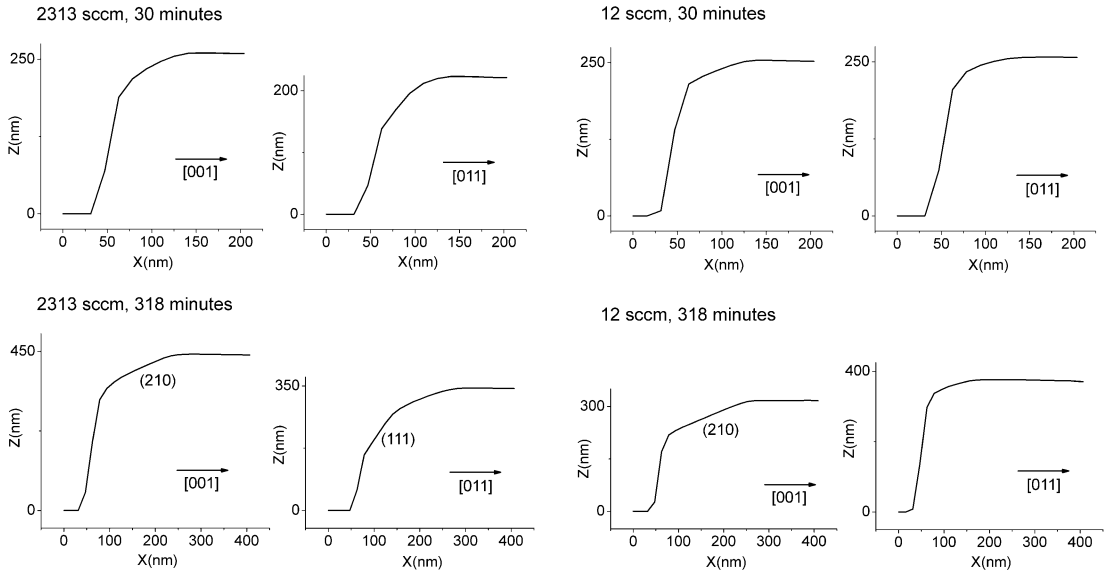

Figure 3-9. AFM height profiles of some stable edges in pre-patterned Ni(100) films. The annealing condition, annealing time, and edge retraction directions are indicated in each height profile. There are small errors in measured angles that might be caused by AFM tip artifacts or small deviations of the scan directions from the edge normal directions.

The annealing ambient affects the formation of each facet since gas adsorption can alter the shape of a γ-plot. The shape of a γ-plot is influenced by impurity adsorption because the impurity adsorption energy depends on the crystallographic orientations of surfaces. It has been suggested that impurity adsorption can deepen the cusps at orientations such as {100}, {110}, and {210} relative to the cusp at {111} in the γ-plot of nickel [54, 55]. During edge retraction, {111} facets appear earlier and more clearly at a reducing gas flow rate of 2310 sccm while {210} facets appear earlier and more clearly at 12 sccm as shown in Figs. 3-8 and 3-9. This can be associated with the effect of oxygen adsorption on the surface energy. As the flow rate of the reducing gas decreases, the coverage of oxygen absorbates on the Ni surface increases. This could deepen the cusp at

{210} in the γ-plot while decreasing the depth of the cusp at {111}. The annealing ambient also affects the edge retraction velocity. At 2310 sccm, the edge retraction velocities show the most prominent cusps in the directions in which rims expose a clear {111} facet, while they show the most prominent cusps in the directions in which the rims expose a clear {210} facet at 12 sccm (see the polar plots in Figs. 3-4(b) to 3-4(e) and height profiles in Figs. 3-8 and 3-9). The effects of the annealing ambient on both faceting and edge retraction velocities suggest that surface energy anisotropy plays a role in determining the kinetics of edge retraction and which retraction directions will be slowest.

Because edges retract via surface diffusion, the surface diffusivity can also affect the anisotropy of the edge retraction velocity. Surface diffusion will be slowest on the flat film surface behind the rim, where there is no curvature gradient. Hence, surface diffusion on the flat film surface will be rate-limiting and will determine the effect of surface diffusivity on the edge retraction velocity. Surface diffusivity can be represented as a second-rank tensor

$$D_{ij} = \begin{bmatrix} D_{11} & D_{12} \\ D_{21} & D_{22} \end{bmatrix} .$$

Two principle axes can be determined by diagonalizing the tensor, and the surface diffusivity in a direction at angle θ to a principle axis is given by

$$D_s(\theta) = D_1 \cos^2\theta + D_2 \sin^2\theta ,$$

where D_1 and D_2 are principal values of the surface diffusivity tensor [57]. Given that D_1 and D_2 are the same for (100) surfaces, surface diffusion on (100) surfaces is expected to

be isotropic, so that the polar plot of the edge retraction velocity in (100) films should have four-fold symmetry, even if surface-diffusion on the flat film surface is rate limiting to the point that it significantly affects the edge retraction velocity. However, breakdown in four-fold symmetry is seen in Figs. 3-4(b) and 3-4(c).

Inspection of the flat surfaces of these films reveals striations (see Fig. 3-10), which are associated with ledges and terraces resulting from misorientations between the film and substrate. To measure the misorientation between the Ni(100) film and MgO(100) substrate, we carried out high resolution XRD measurements, with the results shown in Fig. 3-11 and Table 3-1. The peak positions (2θ(peak) of 2θ-ω scan and ω(peak) of the rocking curve) in the plots were determined using Bruker software. The tilt angles of the {100} plane normal of the MgO and Ni from the z-axis of the sample stage can be calculated by subtracting the value of 1/2*2θ(peak) from the value of ω(peak) as illustrated in Fig. 2-2. The tilt angle of the {100} plane normal was –0.3057° for MgO and –0.7136° for Ni. The misorientation between MgO(100) and Ni(100) is the difference between the two tilt angles. Therefore, the misorientation is 0.4079°, which is close to the angle indicated in the AFM height profile shown in Fig. 3-10. Since surface diffusion on crystals is a thermally activated process, surface atoms have to overcome an activation barrier to migrate over a flat terrace. It is also known that there is an additional activation barrier (the Ehrlich-Schwoebel barrier) for surface atoms to overcome when they jump over terrace edges [58-60]. Due to the Ehrlich-Schwoebel barrier at terrace edges, the surface diffusivity in the direction perpendicular to the striations will be lower than that in the direction parallel to the striations indicated in the AFM image of Fig. 3-10.

The effect of the striations on surface diffusion is therefore expected to lead to the breaking of the four-fold symmetry expected for a fully aligned (100) film. This shows that when anisotropic diffusion is present, it, as well as surface energy anisotropy, contributes to the anisotropy of the edge retraction velocity.

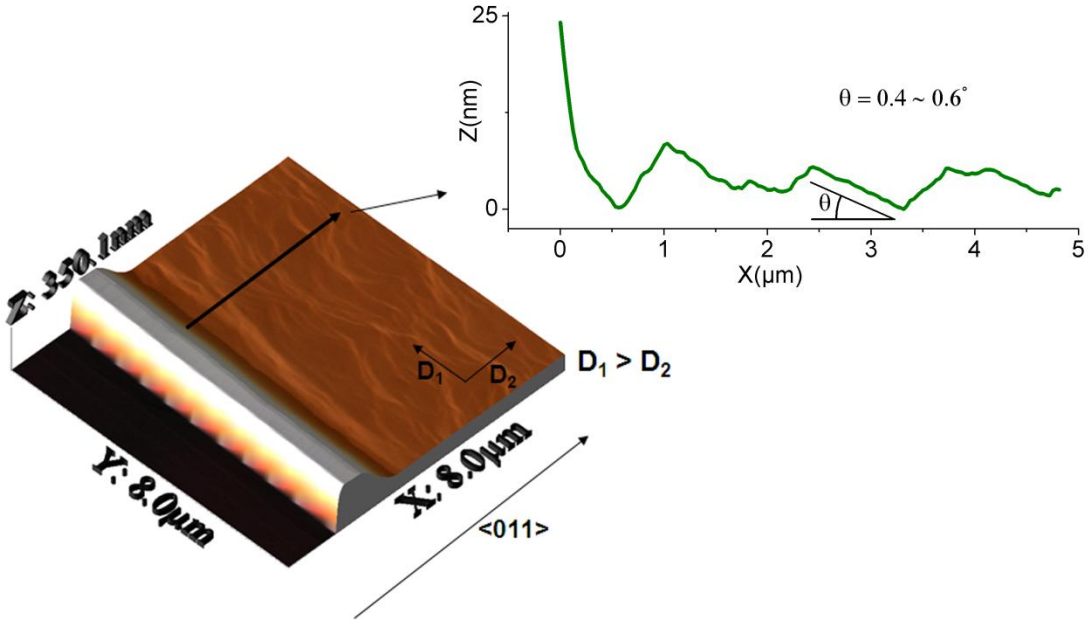

Figure 3-10. Striations on the flat film surface behind the pre-patterned edge retracting in the <011> direction in a Ni(100) film. The lower left figure is an AFM image and the upper right figure is a corresponding height profile of the flat surface behind the edge. The angle between the terrace and the horizontal line is indicated in the AFM height profile.

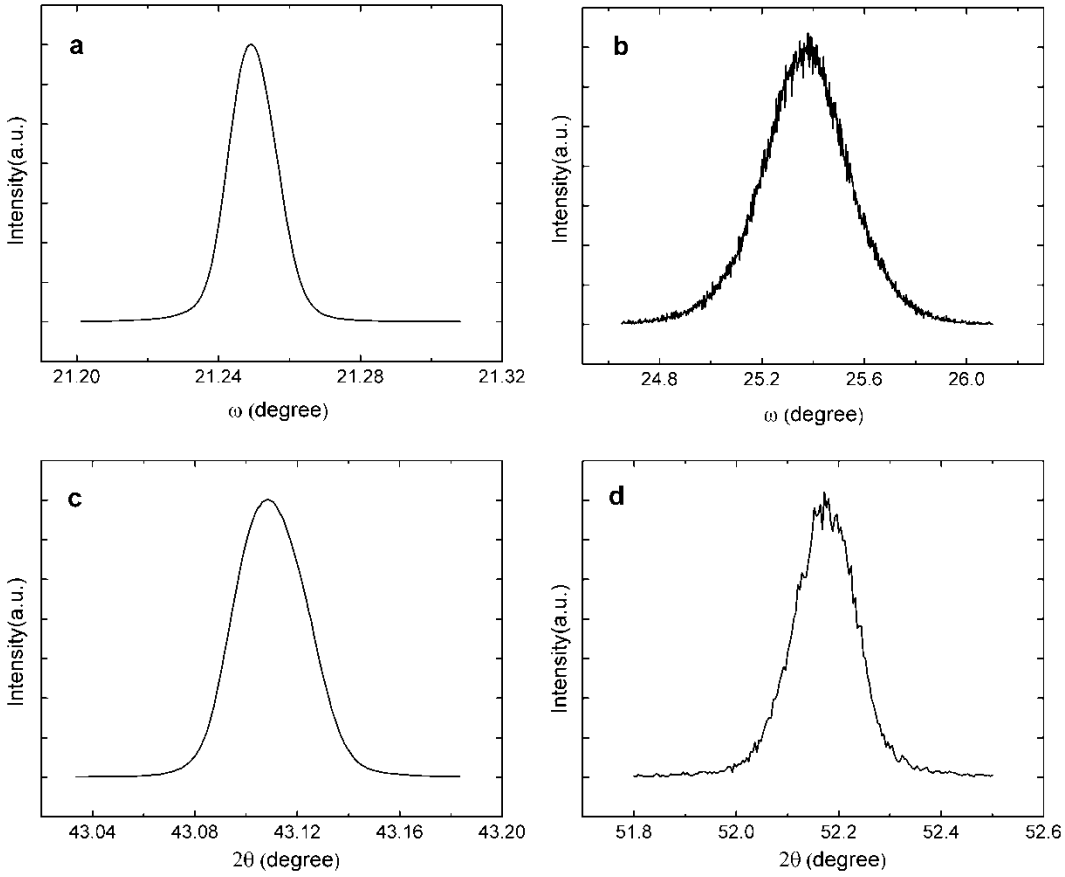

Figure 3-11. High resolution XRD measurements for the sample shown in Fig. 3-10. (a) Rocking curve for MgO(100). (b) Rocking curve for Ni(100). (c) 2θ-ω scan for MgO(100). (d) 2θ-ω scan for Ni(100).

Table 3-1. Peak positions in each measurement shown in Fig. 3-11.

	ω(peak) in Rocking curve	2θ(peak) in 2θ-ω scan
MgO(100)	21.2491°	43.1096°
Ni(100)	25.3738°	52.1748°

While the natural holes seen in Fig. 3-2 are bound by specific edges that show prominent cusps in the edge retraction velocity, the shapes of natural holes in Ni(110) films are more anisotropic and more significantly affected by the annealing ambient than the edge retraction velocities determined for large patterns (see Fig. 3-4). This can be attributed to the different diffusion fields along the perimeter of a natural hole compared to that in front of a long edge. Since the retraction of a long edge is driven by a surface curvature gradient that exists only in the retraction direction, the diffusion field can be considered unidirectional. Due to the unidirectional diffusion field, the retraction velocity of a long edge decreases with time as material accumulates and the surface curvature gradient decreases [10] (see the plots in Fig. 3-12. The sub-linear relationship between the retraction distance and annealing time shows that the retraction velocity decreases with time).

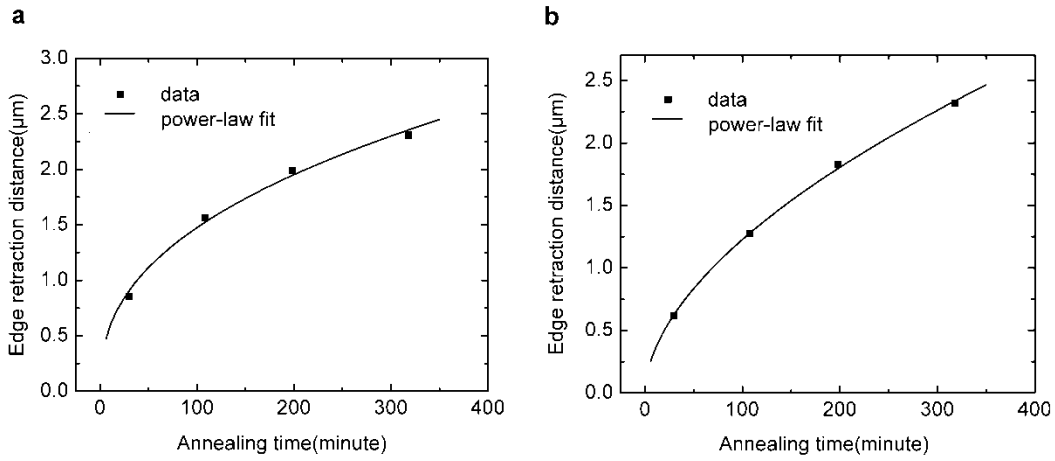

Figure 3-12. Retraction distances of 90 μm-long edges versus annealing time. (a) The edge that retracts in the [001] direction in Ni(110) film. (b) The edge that retracts in the [011] direction in Ni(100) film. The data were collected from samples annealed in a reducing gas flow rate of 2310 sccm. The data are well-fitted by a power-law with the exponent of 0.4 for (a) and 0.56 for (b).

In contrast, the diffusion field around a natural hole is complicated because its perimeter expands around the corners and the expanding perimeter is filled with material diffusing from the edges. If each edge of a natural hole has a different retraction velocity, material diffusing from a faster edge can fill the expanding perimeter earlier than material diffusing from the other edge, as illustrated in Fig. 3-13. This diffusion flux therefore reduces the amount of material that accumulates in the rim of the faster edge and accelerates the retraction velocity relative to that of the slower edge, leading to the more anisotropic shape of the natural hole compared to what might be expected from the velocity anisotropy of long edges.

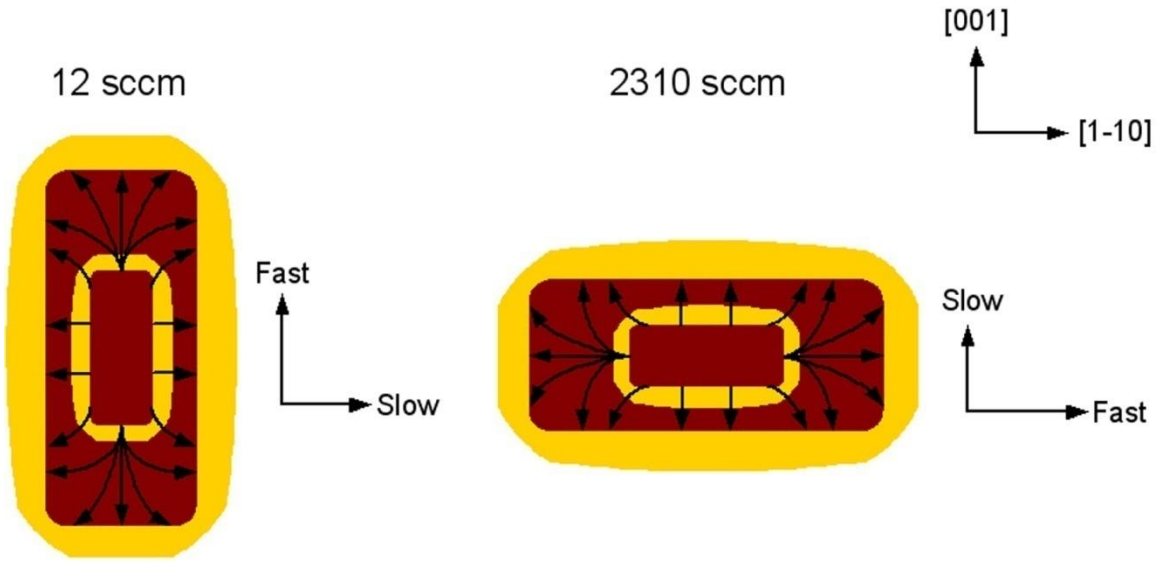

Figure 3-13. Schematic diagram of the diffusion field around a growing natural hole in a Ni(110) film.

While the absolute edge retraction velocities are different for long edges and the edges of a hole, the crystallographic orientations of the slowest edges remain the same. The change in relative magnitudes of the rate of edge retraction observed for long edges in different annealing ambients is consistent with the change in the crystallographic orientations of the edges of growing holes seen in Fig. 3-2.

3.4 Summary

In this chapter, we have shown that morphological evolution during solid-state dewetting of single crystal Ni thin films depends strongly on their crystallographic orientation and the annealing ambient. We measured the rates of edge retraction for single-crystal (110) and (100) Ni films with edges patterned along different in-plane crystallographic directions. By analyzing the morphological evolution during the edge retraction in detail, we show that both anisotropic surface energy and surface diffusion lead to anisotropic edge retraction velocities, but that effects due to surface energy anisotropy dominate and lead to sharp cusps in polar plots of the edge retraction velocity. The characteristic anisotropy in the edge retraction velocity can be understood in terms of in-plane orientation-dependent edge faceting, with single faceting in specific edges, and multiple micro-faceting in other edges. Faceting occurs due to surface energy minimization, and is modified by changes in the annealing ambient. Changes in facet morphologies affect the relative edge retraction rates in different crystallographic orientations. This leads to specific in-plane faceted shapes of growing natural holes that depend on the crystallographic orientation of films and annealing ambient. This study has

led to quantitative understandings of the key elements of edge retraction during the dewetting of single crystal thin films, and will provide the basis for understanding more complex morphologies that result from dewetting of unpatterned and patterned single crystal films that will be discussed in following chapters.

Chapter 4

Instabilities in growing holes

4.1 Introduction

Shapes of growing holes become more and more complex as the dewetting process proceeds, and the complex growth of holes eventually leads to the formation of lines and particles. The kinetic mechanism of thin film dewetting has been described in detail for an isotropic surface energy, and Rayleigh-like and fingering instabilities, as well as mass shedding, have been identified as possible mechanisms for the complex morphological evolution. During the growth of a hole, a thickening rim develops at the edges and the rim often breaks down via a fingering or pinch-off instability that leads to formation of lines that subsequently decay into isolated islands through a Rayleigh-like instability.

Regular morphologies of dewetted single-crystal nickel and SOI thin films show the possibility of producing ordered arrays of crystallographically-aligned catalysts via solid-state dewetting of thin films. It has been shown that similar kinetic processes seen in dewetting of isotropic films lead to formation of isolated islands during dewetting of single crystal films, but specific kinetic mechanisms of the dewetting of single crystal films have not been clearly identified. In this chapter, we present results of studies of the late stage-dewetting of 120nm-thick single crystal Ni(100) and Ni(110) thin films. In the late stage, natural holes develop substantially more complex structures compared to the

simple in-plane faceted shapes observed in the early stage. By tracking the growth of individual holes we clearly identify corner-induced instabilities, mass shedding processes, fingering instabilities, and Rayleigh-like instabilities that lead to development of the complex morphologies. We also observe growth of pre-patterned square and rectangle holes with various initial sizes and aspect ratios to further study corner-induced instability and characterize the effect of edge length of holes on unstable hole growth at corners [61].

4.3 Experimental

120 nm-thick single crystal Ni(100) and Ni(110) films on MgO(100) and MgO(110) substrates were annealed in a Lindberg/Blue Mini-Mite furnace for a long enough time to observe unstable hole growth and isolated island morphologies. The annealing conditions were the same as those described in the previous chapter except for the longer annealing time. We observed morphological evolution during dewetting of the Ni films using SEM and tapping mode AFM. The AFM imaging was carried out using a Veeco Nanoscope IV AFM. The AFM images were then analyzed using WSxM software developed by Nanotec Electronica [49]. The SEM images were taken using an FEI/Philips XL30 FEG ESEM. Pre-patterned holes with various shapes and sizes were produced in a Ni(110) film by milling the film with 30pA ion-beam in FEI DualBeam 235 FIB system. A film with the pre-patterned holes was annealed under a reducing gas flow rate of 90 sccm in the Transtemp furnace and growth of pre-patterned holes was observed using SEM.

4.3 Results and Discussion

Figure 4-1 shows growth of natural holes beyond the early stage, in which natural holes maintain their simple in-plane faceted shapes. As seen in the figure, natural holes still have regular shapes that strongly depend on the crystallographic orientations of the films and the annealing ambient. Natural holes grow as Ni diffuses from the three-phase boundary at the substrate surface to the flat film surface, and the rims around natural holes thicken as seen in the early stage of hole growth. However, in the late stage of growth, natural holes evolve to more complex shapes as their edges lag at the centers behind the other parts of the edges.

These shape evolutions can be understood in terms of the difference in the diffusion fields at the centers of the edges and near the corners. As illustrated in Fig. 4-2, near the corners of a hole, material diffuses in various directions to fill expanding perimeters while material accumulates in front of the edges at the centers of the sides. This results in accumulation of more material at the centers of the edges than near the corners, as seen in Fig. 4-1. Accumulation of material and thickening of rims lead to a decrease in the gradient in surface curvature, which is the driving force for edge retraction. The consequence is that the retraction velocity of the edges, especially near the centers, decreases relative to that near the corners [37]. This corner-induced instability is analogous to a fingering instability [13], but is caused by the shape of the diffusion field rather than the development of a rim instability. The edges at the centers lag more and more as holes grow. In the case of natural holes in Ni(110) films, this process often leads

to formation of a line and subsequent development of another corner-induced instability as shown in Fig. 4-7(b) (top-view image), Fig. 4-1(h), and Figs. 4-1(k) and 4-1(l).

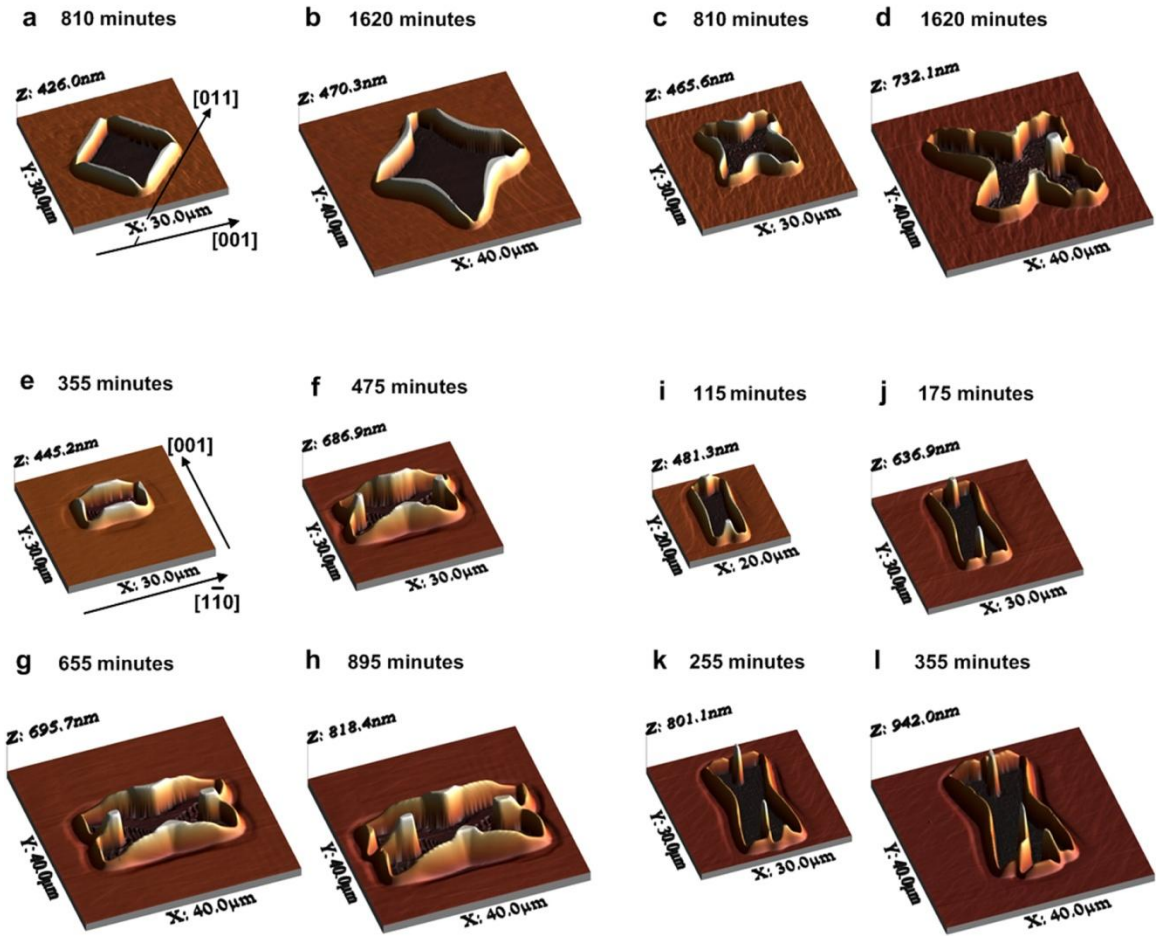

Figure 4-1. AFM images of growing natural holes in Ni(100) and Ni(110) films after their edges have become unstable. (a), (b) Ni(100), 2310 sccm. (c), (d) Ni(100), 12 sccm. (e)-(h) Ni(110), 2310 sccm. (i)-(l) Ni(110), 12 sccm. The annealing times are indicated in the images.

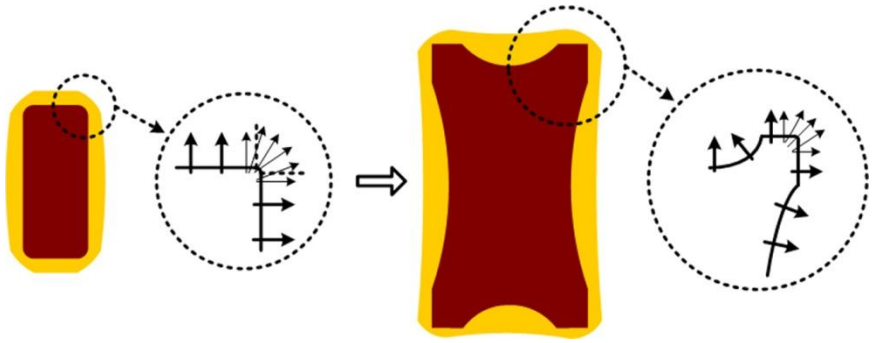

Figure 4-2. Schematic illustration of the diffusion field around a natural hole, illustrating the cause of a corner-induced instability. [61]

To further demonstrate the origin of the corner-induced instability, we quantitatively investigated the uneven accumulation of material around natural holes. Figures 4-3 and 4-4 show the change of the rim height and width measured across the corners and edge centers of growing holes shown in Figs. 3-2 and 4-1. The measurements were carried out using AFM images. As seen in the figures, the rim height and width measured across the corners do not increase after the early stage of hole growth while those measured across the centers of edges continue to increase. Given the evolution of rims seen in Figs. 4-3 and 4-4, edge retraction near the corners and at the centers of edges is seen to be similar to that described by the Jiran and Thompson model and that described by Brandon and Bradshaw model, respectively. As seen in the equations for the edge retraction velocity derived from the two models (Equations 1-5 and 1-6), the difference in edge profiles during edge retraction leads to the different time dependence of the edge retraction velocity. The edge retraction velocity decreases with time in the Brandon and Bradshaw model while it remains constant in the Jiran and Thompson

model. Therefore, edges of holes will become more and more unstable over time during the growth of holes when edge retraction at different locations of the hole edges follows different models. The corner-induced instability shown in Fig. 4-1 can be seen as a particular type of the edge instability.

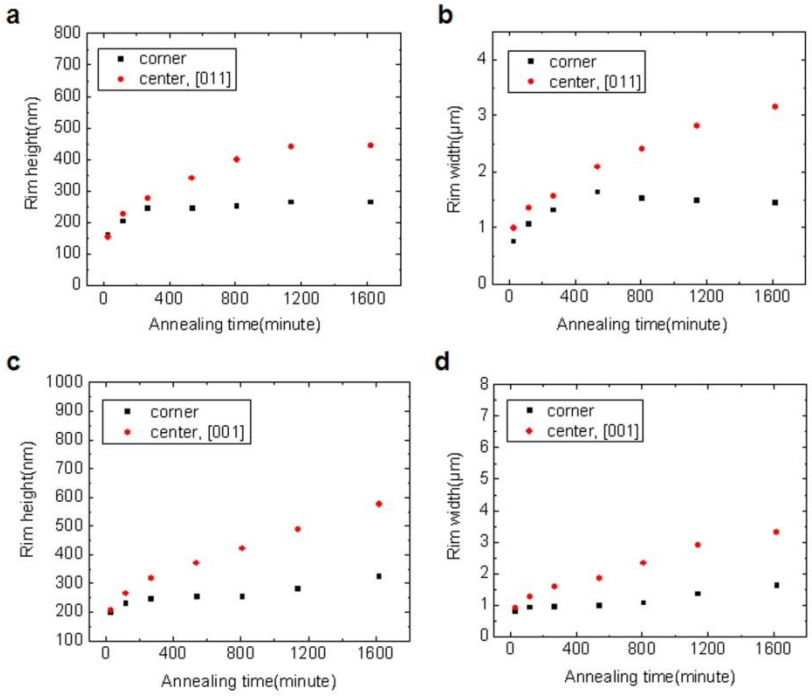

Figure 4-3. The change of the rim height and rim width across the corner and edge center of a natural hole in a Ni(100) film during annealing. (a) and (b) At a reducing gas flow rate of 2310 sccm. (c) and (d) At a reducing gas flow rate of 12 sccm.

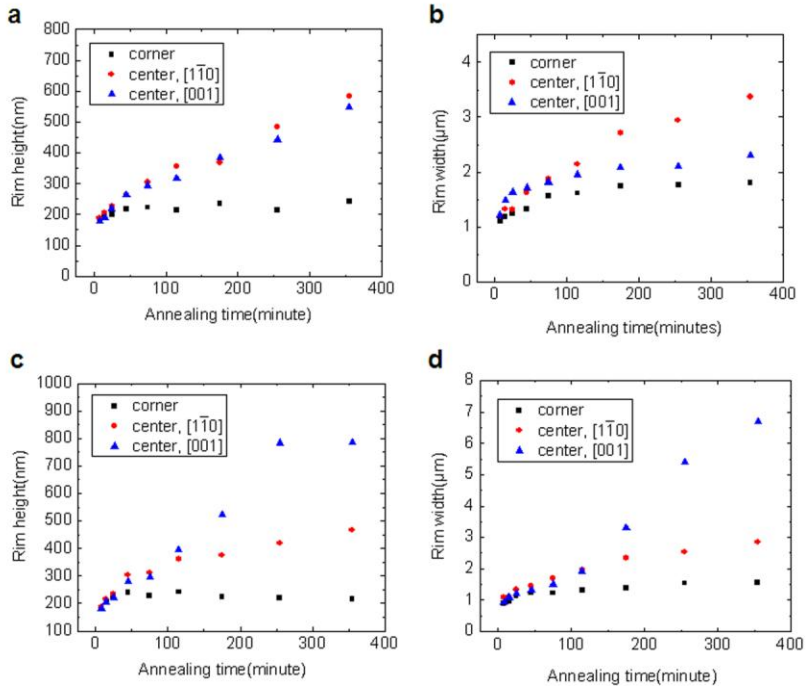

Figure 4-4. The change of the rim height and rim width across the corner and edge center of a natural hole in a Ni(110) film during annealing. (a) and (b) At a reducing gas flow rate of 2310 sccm. (c) and (d) At a reducing gas flow rate of 12 sccm. The directions in each plot indicate the retraction directions of the two edges of a natural hole in a Ni(110) film.

Based on the shape of growing natural holes shown in Fig. 4-1, we suggest that material diffusing out from edges fill expanding perimeters of natural holes only at locations of edges within a certain distance from the corners of the holes, as illustrated in Figs. 3-13 and 4-2. To further demonstrate the shape of the diffusion fields, we observed growth of square and rectangle holes with various initial sizes and aspect ratios, all of which were patterned from a Ni(110) film. The sample was annealed in a Transtemp furnace at 900°C for 35 minutes under a reducing gas flow rate of 90 sccm. The annealing time is defined as the total annealing time of multiple annealing runs, summing to 5 minutes, 15 minutes, 25 minutes, and 35 minutes. It should be noted that shapes of

natural holes in this film were similar to the shape of a natural hole seen in Fig. 3-2(h). As seen in Fig. 4-5, the development of a corner-induced instability depends on the initial length and in-plane crystallographic orientation of edges of pre-patterned holes. The corner-induced instability develops earlier at longer edges in a given in-plane crystallographic orientation of edges, leading to lag of retraction near the centers of edges. The distance between a certain location and the corner of a hole is therefore seen to determine the shape of the diffusion field at given location. This result is consistent with the diffusion field illustrated in Fig. 4-2.

Edges with an initial length of 0.9 μm remained straight during hole growth for both edge normal directions, <110> and <001>. However, the retraction velocity was much higher in the <001> directions as previously seen in the natural hole of Fig. 3-2(h). Given that the anisotropy of the edge retraction velocity is lower for long edges, the highly anisotropic edge retraction in the pre-patterned holes also indicates that material diffusing from a faster edge fills the expanding perimeter of holes earlier, as previously illustrated in Fig. 3-13. Due to the diffusion field, a corner-induced instability develops more clearly in the <001> directions than in the <110> directions, as seen in Fig. 4-5. Consequently, the retraction velocity at the centers of edges depend on the initial lengths of edges more strongly in the <001> directions than in the <110> directions. Figure 4-6 shows the retraction distance at the center of edges in the <001> and <110> directions versus the total annealing time. As seen in the figure, the retraction velocity at the center of edges is slower, as the initial edge is longer in both directions. However, the difference is larger in the <001> directions.

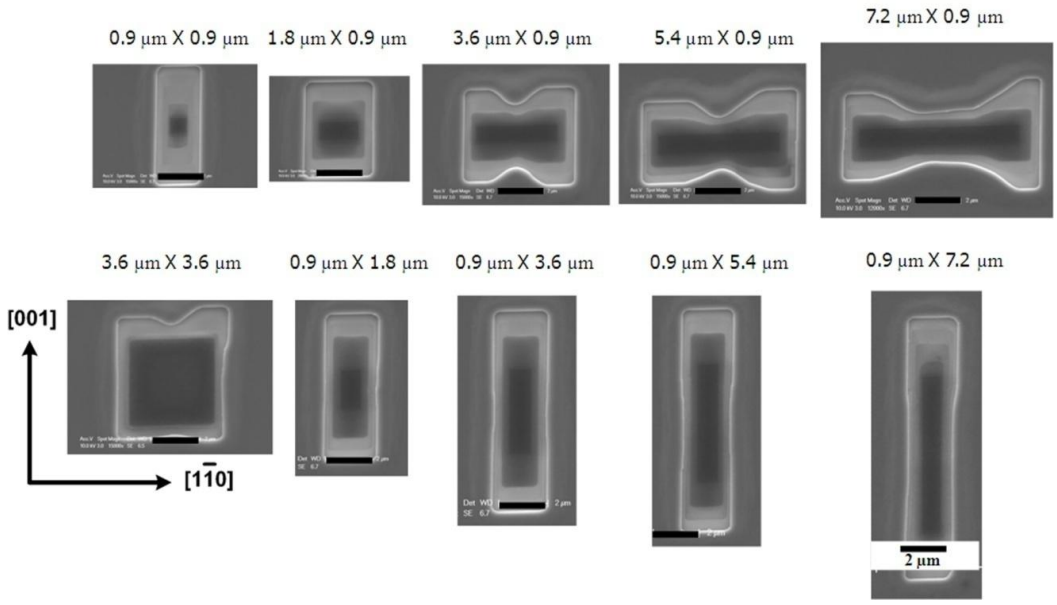

Figure 4-5. Growth of square and rectangle holes with various initial sizes and aspect ratios, all of which were patterned from a Ni(110) film. Holes were patterned using FIB milling. Initial dimensions of pre-patterned holes are indicated above each image. The in-plane crystallographic orientation is indicated in the lower-left corner. Scale bar, 2 μm.

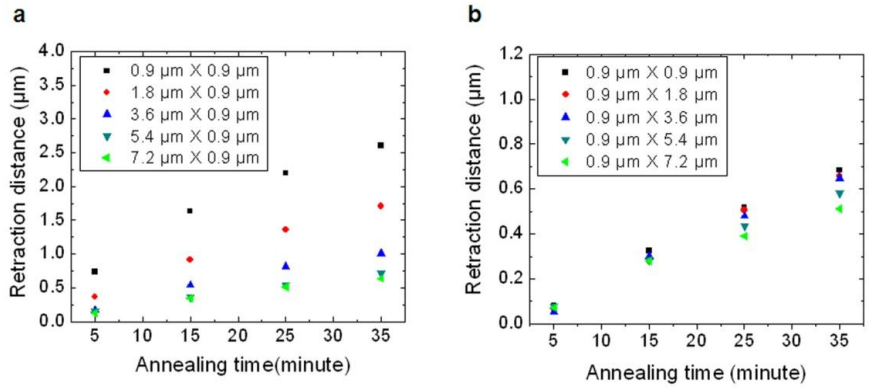

Figure 4-6. Retraction distance at the centers of edges with different initial lengths versus the total annealing time, (a) in the <001> directions and (b) in the <110> directions.

Natural holes in Ni(110) films annealed under a reducing gas flow rate of 2310 sccm are also subject to an additional instability that causes the film to touch the substrate

surface behind thickening rims. Figure 4-7 shows the evolution associated with this 'pinch-off' process at edges. Valleys develop and deepen behind thickening rims, until the valleys contact the substrate to form new rims and leave a line behind, as seen in Fig. 4-7(c). This mass shedding process is similar to that proposed by Wong et al [11]. Valleys also developed behind thickening rims in Ni(110) films annealed at 12 sccm as seen in Figs. 4-1(g) and 4-1(h), but the valley deepening rate was slower. This pinch-off process did not occur in Ni(100) films. Dornel et al. [12] modeled the evolution of a 2D cross section of a film with an edge and found that the anisotropy of surface energy affects the development and deepening rate of valleys. In the previous chapter, we have shown that the surface energy anisotropy of nickel along thickening rims depends on the initial crystallographic orientation of the film. This suggests that the differences in the pinch-off processes is due to the difference in surface energy anisotropy along thickening rims for Ni(110) and Ni(100) films. (We will further study important factors that affect the pinch-off behavior, including the anisotropy of surface energy, in chapter 5).

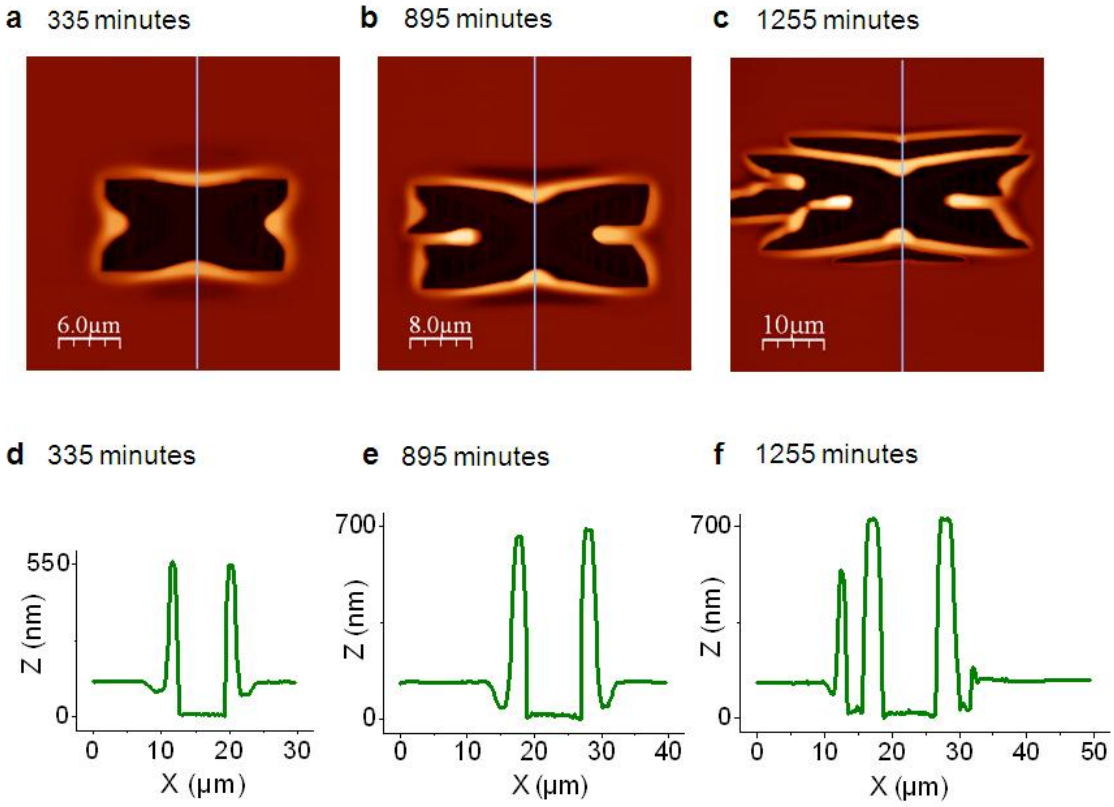

Figure 4-7. Deepening of valleys and pinch-off of edges in a natural hole in a Ni(110) film. The flow rate of reducing gas was 2310 sccm. (a)-(c) AFM height images. (d)-(f) AFM height profiles. The annealing times are indicated in the figures. [61]

Figure 4-8 shows more complex morphologies in the Ni films further annealed under a reducing gas flow rate of 2310 sccm. In the later stage of morphological evolution of Ni(110) films, development of a corner-induced instability and the pinch-off process occur iteratively and lead to formation of arrays of lines, as seen in Figs. 4-8(a) and 4-8(b). It has been shown that long solid lines are generally subject to a Rayleigh-like instability since they have higher interfacial energy compared to an array of isolated islands with spacings above a critical value [9, 14, 15]. Due to this Rayleigh-like

instability, the long lines eventually decompose into isolated islands as shown in Fig. 4-8(c).

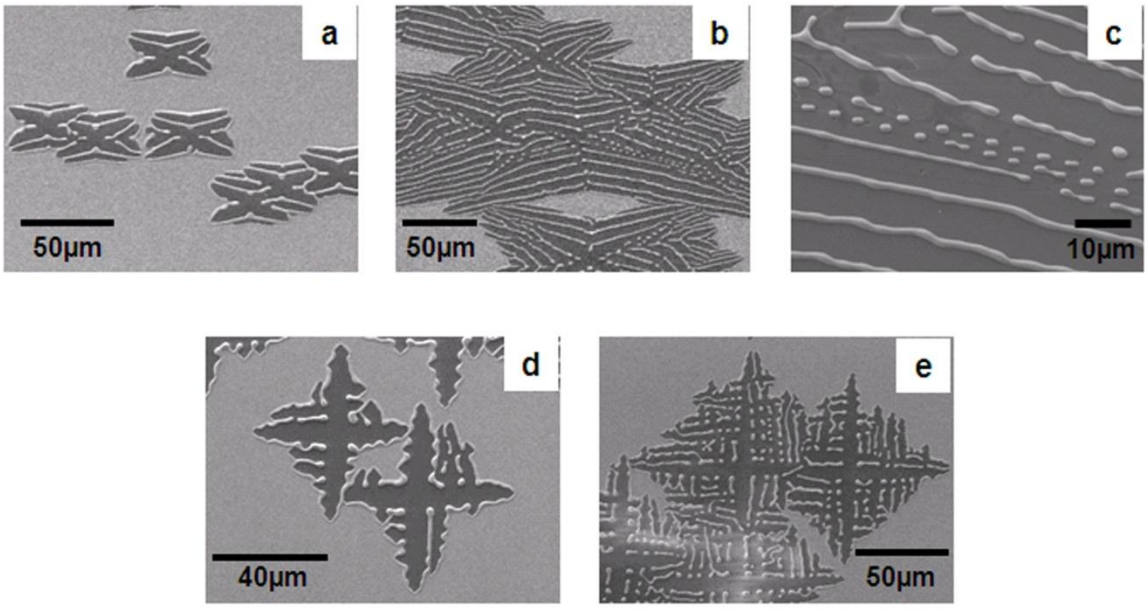

Figure 4-8. SEM images of complex morphologies in the late stage of morphological evolution. (a) through (c) Images of a dewetting Ni(110) film, (a) annealed for 1255 minutes and (b) annealed for 4495 minutes. (d) through (e) Images of a dewetting Ni(100) film, (d) annealed for 3240 minutes and (e) annealed for 4200 minutes. The flow rate of reducing gas was 2310 sccm. [61]

In the case of Ni(100) films, an instability develops along the lengths of thickening rims of the retracting corners and causes formation of finger-like edges, as seen in Figs. 4-8(d) and 4-8(e). These fingers propagate faster than other parts of edges, leaving long lines between them. The long lines between fingers are also subsequently subject to a Rayleigh-like instability that leads to formation of isolated islands [Fig. 4-8(e)]. The fast propagation of the fingers implies that this instability began with a perturbation in the thickness of the rims, and that the rims were thinner where the fingers

formed, as suggested in the model by Kan and Wong [13] and described for polycrystalline films by Jiran and Thompson [8, 9]. It should be noted that the tips of the fingers have the same shapes as the corners shown in Figs. 4-1(a) and 4-1(b) and this causes the fingers to continue to propagate faster than other parts of edges during the growth of natural holes. The overall evolution seen in Figs. 4-8(d) and 4-8(e) is reminiscent of the dendritic growth observed during solidification [62].

4.4 Summary

To summarize, we report that morphological evolution in the late-stage dewetting of single crystal Ni thin films also depends strongly on the crystallographic orientations of the films and annealing ambient, and is governed by a series of instabilities. Growing holes are subject to instabilities at retracting corners that lead to their rapid growth relative to the hole edges. By analyzing the growth of natural holes and pre-patterned holes in detail, we have shown that the corner-induced instability originates from the specific shape of the diffusion field around growing holes. In the case of natural holes in Ni(110) films, the lagging regions at the centers of edges evolve through the iteration of either development of a corner-induced instability or a mass shedding process, and form long lines. In Ni(100) films, a fingering instability causes formation of long lines. These lines are subsequently subject to a Rayleigh-like instability that leads to formation of isolated islands. These are the key mechanistic elements that produce complex morphologies during solid state dewetting of continuous single crystal films.

Development of these understandings will provide a basis for controlling these phenomena to fabricate specific ordered structures.

Chapter 5

Retraction and Pinch-off of Edges in Patterned Ni Films

5.1 Introduction

As shown in the previous chapters, dewetting of thin films requires formation of holes, followed by retraction of the film edges at the perimeters of the holes. Because of the large surface curvature gradient at the film edge, material diffuses from the three-phase boundary at the substrate surface to the flat film surface and this diffusion results in retraction of the edge. A two-dimensional numerical study of the edge retraction of a semi-infinite film has shown that the film surface near an edge evolves to a characteristic shape with a thickened rim and an adjacent valley. As the edge retracts and the rim continues to thicken, the valley often deepens and eventually reaches the substrate surface to pinch-off and leave a semi-cylindrical wire and a new film edge. The new edge retracts again and the pinch-off process is periodically repeated.

For the case of films having a finite width, recent 2D simulations suggest that edge retraction can result in the formation of different numbers of wires, depending on the thickness-to-width ratio of the film as well as the anisotropy of the energy of the film surface and the contact angle at a three-phase boundary [12]. In the case of pre-patterned single crystal films, it was shown in chapter 3 that the dewetting rates depend on the initial crystallographic orientation of the edge, and this anisotropy can be understood in

terms of simple models for faceting of retracting edges. In this chapter, we present results of regular morphological evolution during the dewetting of square and cross patches with different initial sizes and long line patches with various initial widths, all of which are patterned from single crystal Ni(110) films. Reproducible evolution to smaller-scale regular patterns is observed as these simple large-scale patches dewet through the retraction and pinch-off of edges. To understand the underlying mechanisms of this phenomenon, we characterized the effects of geometries of patterned films, contact angles of edges, surface energy anisotropy, the anisotropic retraction velocities, and the deepening rates of valleys adjacent to retracting edges.

As shown in the previous chapter, pinch-off of edges does not occur during dewetting of continuous Ni(100) films. We also analyze morphological evolution during dewetting of square patches patterned from a Ni(100) film to further characterize the effect of surface energy anisotropy on the pinch-off phenomenon.

5.2 Experimental

120 nm-thick single crystal Ni(110) and Ni(100) films were also used in this work. After the depositions, films were patterned into square, cross, and long line patches via photolithography followed by wet etching of Ni. The pre-patterned films were annealed in a tube furnace (Lindberg/Blue Mini-Mite model) at 900°C with flowing reducing gas (5% H_2 and 95% N_2). The flow rate of the reducing gas was set to 2310 sccm during annealing. We observed the results of morphological evolution of the pre-patterned films using SEM and AFM. The AFM imaging was carried out in tapping mode using a Veeco Nanoscope IV AFM. The AFM images were analyzed using WSxM software developed by Nanotec Electronic. The SEM images were taken using an FEI/Philips XL30 FEG ESEM. Most of the SEM images were taken in low vacuum mode at a water vapor pressure of 0.8~1.2 Torr to reduce artifacts from charging of the MgO substrate. FIB milling was used to make cross sections of a dewetted cross shaped patterned patch using a Zeiss NVision 40 FIB system. Before putting a sample into the FIB system, it was coated with a carbon layer to reduce charging effects, using a Denton Thermo Vacuum Evaporator. Before milling the pattern, a platinum protection layer was deposited on the location that was to be milled. This deposition was done using a 150 pA ion beam. The milling of the pattern was carried out in several steps. The cross section was made using 700 pA ion beam. Subsequently, 150 pA and 40 pA ion beams were used to clean the cross section.

5.3 Results and Discussion

5.3.1 Ni(110) film

To investigate the effect of pattern size on morphological evolution, we observed dewetting of square patches with various initial sizes and with edges aligned along [001] and $[1\bar{1}0]$ directions of a Ni(110) film. Figure 5-1 shows results for square patches of different widths but a fixed thickness (120 nm). Due to a local surface curvature gradient at each film edge, the edges of these square patches retract and develop thickened rims. As seen in each case, more material accumulates near corners than at the centers of edges and this leads to slower retraction near the corners. This happens because the diffusion fields at any two perpendicular edges overlap at the corners. The height profiles in Fig. 5-1 were measured in the $[1\bar{1}0]$ direction along the dashed lines shown in the figures. Behind thickened rims, except for the smallest patches, valleys form after annealing for 270 minutes (the first column of AFM images and height profiles). In large patches (e.g. the top row of AFM images and height profiles), the valleys reach sufficient depths before they merge to cause pinch-off to form two parallel Ni lines. In smaller patches (e.g. the last two rows of AFM images and height profiles), the smaller initial distance between two parallel edges allows valleys to completely merge before they reach the substrate surface. The single valley then fills to form a single line. This result demonstrates that whether one or two Ni lines form is a function of the initial distance of separation of the two parallel edges. It should be noted that all patterns of a given size

showed the same behavior, except for the second largest patch that evolved to form either one or two lines.

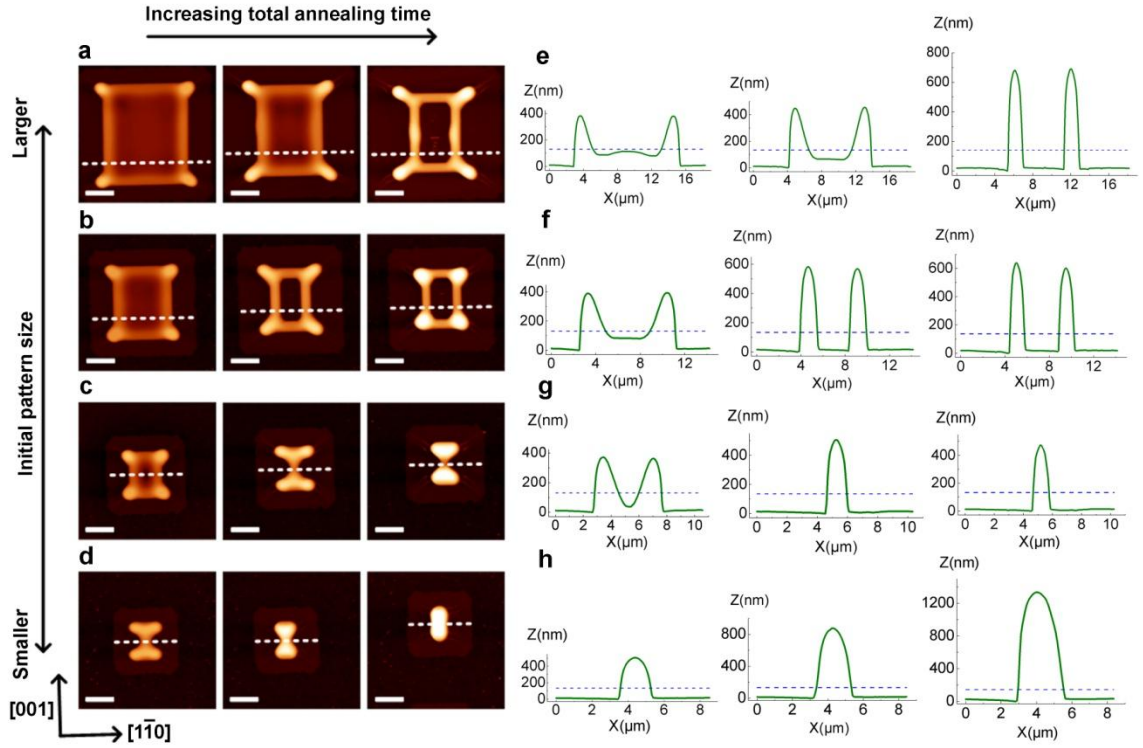

Figure 5-1. Dewetting of square patches patterned from a Ni(110) film. (a)-(d) AFM images of evolving square patches with various initial sizes. The initial edge length of each patch was about 18.4, 14.6, 10.8, and 8.9 μm respectively. The total annealing time was 270 minutes, 540 minutes, and 1020 minutes from the left to right panel. The in-plane crystallographic orientation is indicated in the lower-left corner. Scale bars, 4 μm. (e)-(h) Height profiles for each of the patterns on the left. The height profiles were measured along the dashed lines in the AFM images. The dashed lines in the height profiles show the initial film thickness.

Figure 5-2(a) shows the result of dewetting of an initial patch with a cross shape that was patterned from a Ni(110) film. As seen in Fig. 5-2(a), pinch-off occurs and two separate lines form in the horizontal arm of the cross, while the thickening rims coalesce into a single rim in the vertical arm of the cross. Because the initial distances between two parallel edges are the same in the two arms, this difference in the result of dewetting

is not associated with the size effect seen in Fig. 5-1. Figure 5-2(b) shows the result of dewetting of a larger cross patch. In this pattern, due to the larger initial distances between edges, pinch-off occurs in both the vertical and horizontal arms. As seen in this figure, two parallel Ni lines are observed in the vertical arm and three parallel lines develop in the horizontal arm. This indicates that the initial edge separation was sufficiently large in the vertical arm that the valleys did not completely merge before pinch-off, and that in the horizontal arm, the valleys behind the retracting edges pinched-off while material was still left between them. These pinch-off behaviors of cross patches seen in Figs. 5-2(a) and 5-2(b) are the same in other patches of the same dimension and annealed under the same conditions.

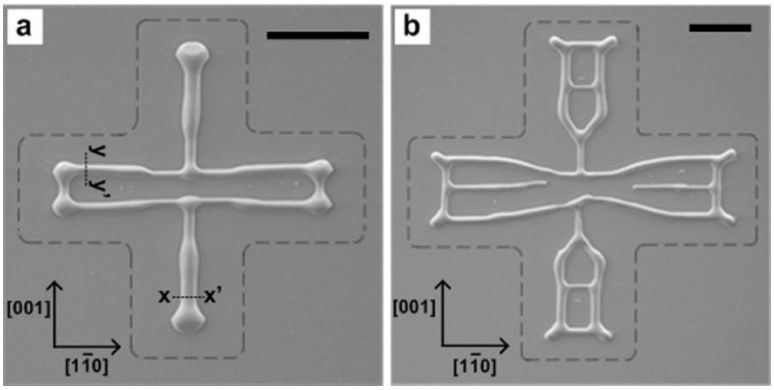

Figure 5-2. Dewetting of cross patches patterned from a Ni(110) film. (a) SEM image of the dewetted pattern that evolved from a smaller cross patch. The edge length of an initial patch was about 10.8 μm. (b) SEM image of the dewetted pattern that evolved from a larger cross patch. The edge length of an initial patch was about 18.4 μm. The gray dashed lines indicate the initial shapes of the patches. The in-plane crystallographic orientations are indicated in the lower-left corners. The total annealing time was 1020 minutes. Scale bar, 10 μm. These images were taken in low vacuum mode.

Dewetting in solid films occurs by diffusion of material from the three-phase line out into the flat surface of the film. When surface energy is isotropic, surface diffusion at the film edge is driven by curvature gradient, with the diffusion flux given by

$$\vec{J} = -\left(\frac{D_s \ \gamma \ N_s \Omega}{kT} \right) \vec{\nabla}_s \kappa \equiv -B_s \vec{\nabla}_s \kappa \,, \tag{5-1}$$

where D_s is the surface diffusivity, γ is the surface energy, N_s is the number of surface atoms per area, Ω is the atomic volume, k is Boltzmann's constant, T is temperature, and κ is the local surface curvature. Dornel et al. [12] modeled evolution of the 2D cross section of a film with width W, thickness H, and film-substrate contact angle α, as shown in Fig. 5-3. They found that, for an isotropic surface energy and a given contact angle, the film would dewet into one, two, or three islands (cylinders), depending on the magnitude of the ratio of W to H, F, with the number of islands (cylinders) increasing with increasing F (as seen in Fig. 5-1 and in comparing the arms in Figs. 5-2(a) and 5-2(b)). They showed that while the time taken to achieve a one, two, or three cylinder structure scales with B^{-1}, the final result is a function of F alone, indicating that the edge retraction velocity and valley deepening rate scale together with B. These conclusions are consistent with our results for edge retraction in a given crystallographic direction.

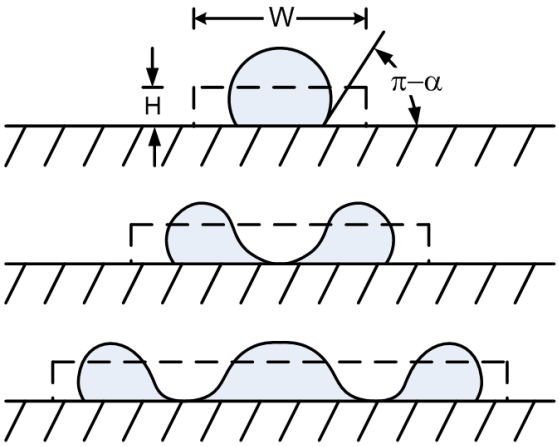

Figure 5-3. Schematic illustration of the cross section of patches with different width, W, to thickness, H, ratios, dewetting into one, two or three lines (after Dornel et al [12]).

We found, though, that the number of lines for a fixed *F* depended on the crystallographic orientation of the retracting edges. This suggests that the relative magnitude of the valley deepening rate-to-edge retraction velocity depends on the crystallographic orientation of an edge. For a fixed F, the number of lines will be larger for the orientation that shows the larger relative magnitude of the valley deepening rate-to-edge retraction velocity. The relative magnitude, rather than the absolute value of valley deepening rate is important because the edge retraction velocity will determine when two parallel edges begin to interact at a given valley deepening rate. Dornel et al. [12] showed that differences in the contact angle and surface energy anisotropy affected the relationship between the number of islands and F by changing the valley deepening rate. As shown in chapter. 3, surface energy anisotropy also affects the anisotropy of the edge retraction velocity. This suggests that the different number of lines we observe for

different arms of the cross structure has its origin in the difference in either the contact angle or surface energy anisotropy at the edges.

To measure and compare the contact angles at the three-phase lines of two arms, we made cross sections using FIB milling across lines with $[1\bar{1}0]$ and [001] in-plane normals. Figures 5-4(a) and 5-4(b) show tilt-corrected SEM images of the two cross sections. As seen in these figures, the contact angles are approximately right angles in both cross sections. Because it is generally known that film edges evolve to reach the equilibrium contact angle at a three-phase boundary in the very early stage of their retraction [11, 12, 63], we can assume that these angles are equilibrium contact angles in each direction and that they have been maintained at equilibrium values from an early stage of evolution. This suggests that the equilibrium contact angle does not play a dominant role in determining the crystallographic differences in pinch-off behavior we observe. However, the facets that are seen in Fig. 5-4, show that the surface energy is anisotropic and that different surfaces are exposed on the two types of lines and edges with different crystallographic orientations. We therefore conclude that the observed differences in pinch-off behavior are most likely associated with surface energy anisotropy.

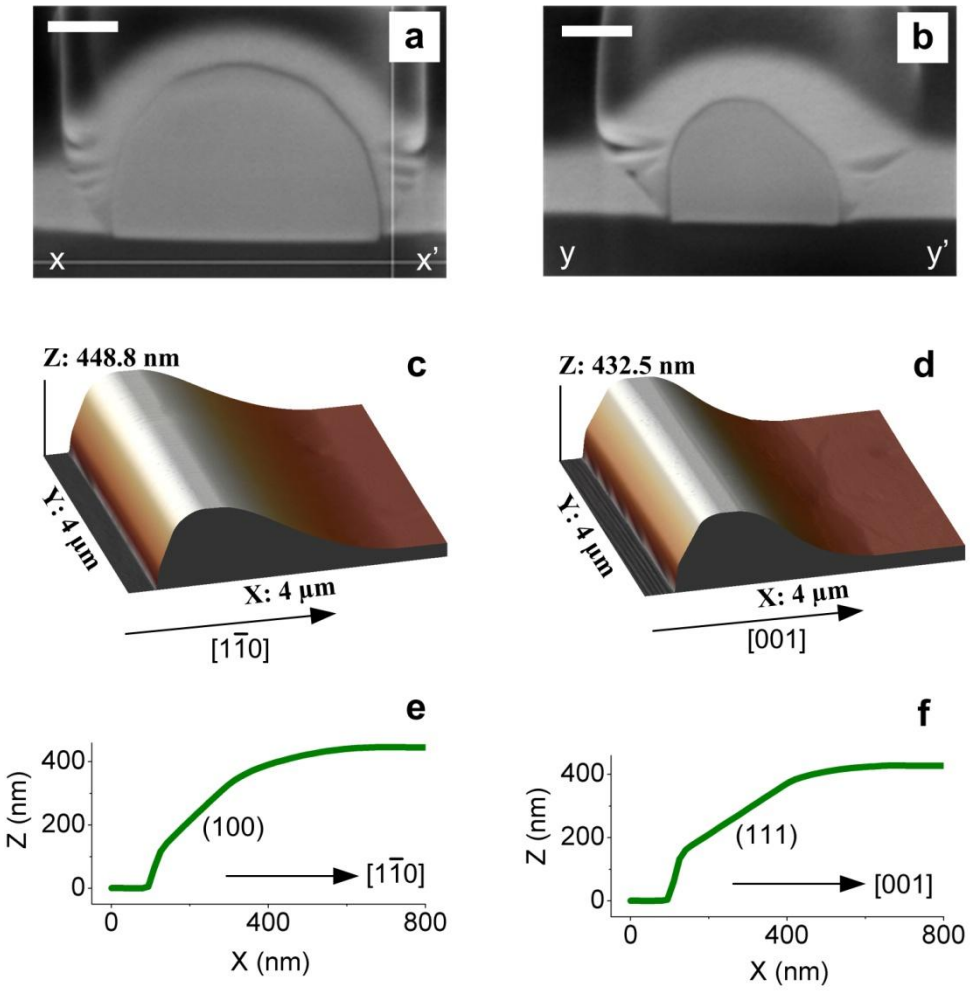

Figure 5-4. **(a)-(b) Tilt-corrected SEM images of FIB-milled cross sections of the lines shown in Fig. 5-2(a). Before milling, the lines were coated with carbon and platinum to reduce charging and protect the nickel. The curved lines are artifacts of milling of these protective layers. Scale bar, 400 nm. (c)-(d) AFM images of thickened edges retracting in the $[1\bar{1}0]$ and $[001]$ directions. The annealing time was 270 minutes. (e)-(f) Height profiles of the thickened edges seen in (c) and (d). These were measured from the substrate surface to the top of the facets. The actual angles in the profiles approximately match the ideal angles of the indicated facets.**

Figure 5-5 shows an early-stage morphology of a dewetting cross patch with the same initial size as the one shown in Fig. 5-2(b). As seen in the figure, valleys deepen faster and the edges retract more slowly in the horizontal arm than in the vertical arm (The slower edge retraction in the horizontal arm than in the vertical arm is consistent with the result of measurement of edge retraction velocities presented in chapter 3. In Ni(110) films annealed at a reducing gas flow rate of 2310 sccm, the edge retraction was found to be faster in the $[1\bar{1}0]$ direction than in the $[001]$ direction (see Fig. 3-4(e)). This leads to a larger number of lines in the horizontal arm than in the vertical arm of the dewetted pattern of Fig. 5-2(b). A number of more complex pinch-off phenomena are also visible in Fig. 5-2(b). Around the middle of the dewetted pattern, the number of lines is smaller than in the arms. There are only two lines in the middle adjacent to the horizontal arms and only a single line in the middle adjacent to the vertical arms. This is associated with concave corners of the cross pattern. As mentioned in the previous chapter, retracting concave corners have a larger diffusion field for redistribution of mass, and hence a higher retraction rate. As seen in Fig. 5-5, the faster retracting concave corners more rapidly move toward the middle of the pattern than the edges of the arms move to the center of the arms. The valley depth was also shallowest behind the concave corner edge. As a consequence of the slower rate of valley deepening and the higher edge retraction velocity at the concave corner, fewer lines developed in the middle of the larger cross patch of Fig. 5-2(b).

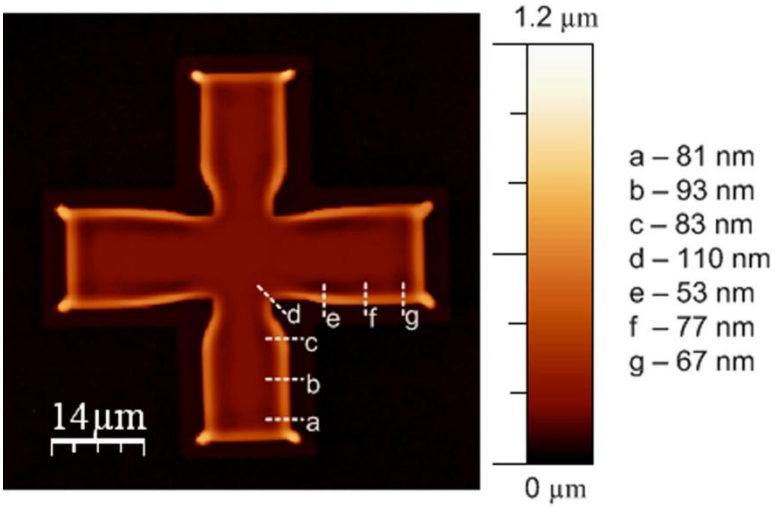

Figure 5-5. AFM image at a relatively early stage of dewetting of a cross patch with the same initial dimensions as the cross patch of Fig. 5-2(b). The annealing time was 270 minutes. The heights of the valleys from the substrate surface were measured along the dashed lines. The results are shown on the right.

Another feature seen in the larger cross patch of Fig. 5-2(b) and not in Fig. 5-2(a) is the horizontal line in the vertical arm of the cross. In the case of the vertical arm in Fig. 5-2(b), edges on either side are sufficiently separated that pinch-off occurs. As shown in Fig. 5-5, valleys are deeper behind convex corners and to the sides of concave corners than in the middle of an arm. This can lead to pinch-off behind the convex corners and at the sides of concave corners, while material was still left in the middle, forming the horizontal line in the vertical arm. Dewetting of patterns with corners has not been analyzed through modeling or simulation. The data and phenomenology presented here, along with other data presented in the previous chapter, will provide a basis for development and testing of models for corner retraction.

Dewetting of 500 μm-long line patches patterned from Ni(110) films showed the effects of the initial width and in-plane crystallographic direction of lines that are completely decoupled from the corner effects. Figures 5-6 and 5-7 show the morphological evolution around the middle of long line patches with various widths and 500 μm-long edges perpendicular to the $[1\bar{1}0]$ and [001] directions respectively. As seen in the figures, long line patches wider than a certain value evolved into a larger number of lines compared to narrower patches in each crystallographic direction of retraction. However, the retraction of long line patches produced a larger number of lines in the [001] direction than in the $[1\bar{1}0]$ direction of retraction for a given initial line width wider than a certain value below which patches form a single line in both directions. The effect of in-plane crystallographic directions of long line patches can also be seen in Fig. 5-8. These effects of the initial line width and an in-plane crystallographic orientation of an edge are consistent with the results shown in Figs. 5-1 and 5-2.

The initial width of the narrowest patch that evolved into two lines was 20.6 μm in the $[1\bar{1}0]$ direction of retraction (the third patch from the left of Figs. 5-6(f) and 5-6(j)). The next patch to the left evolved into a single line although its initial width was 19.2 μm, which was still wider than the initial widths of the square patch (Fig. 5-1(a)) and vertical arm of the cross patch (Fig. 5-2(b)) that evolved into two lines. This is seen to be due to the absence of corners around the middle of a long line patch. As mentioned earlier, the valley deepening rate is higher behind convex corners and to the side of concave corners of cross patches than in other locations, often leading to earlier pinch off in those locations. Because there is not such a corner effect around the middle of long

line patches, the valley deepening rate will be lower and therefore the critical width above which pinch-off occurs and two lines form will probably be wider than in square and cross patches.

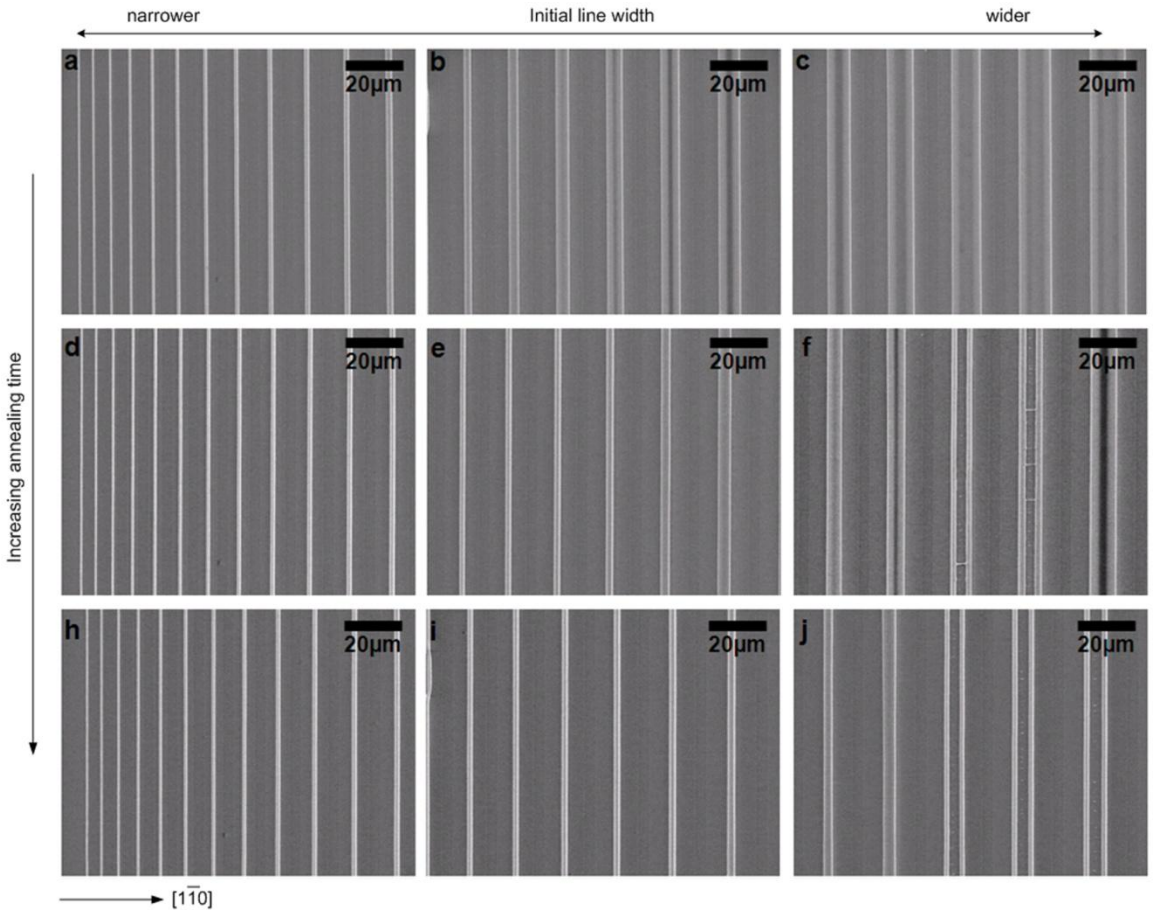

Figure 5-6. Retraction and pinch-off of long lines perpendicular to the $[1\bar{1}0]$ direction. (a)-(c) Images of long lines annealed for 540 minutes. (d)-(f) Images of long lines annealed for 1020 minutes. (h)-(j) Images of long lines annealed for 1600 minutes.

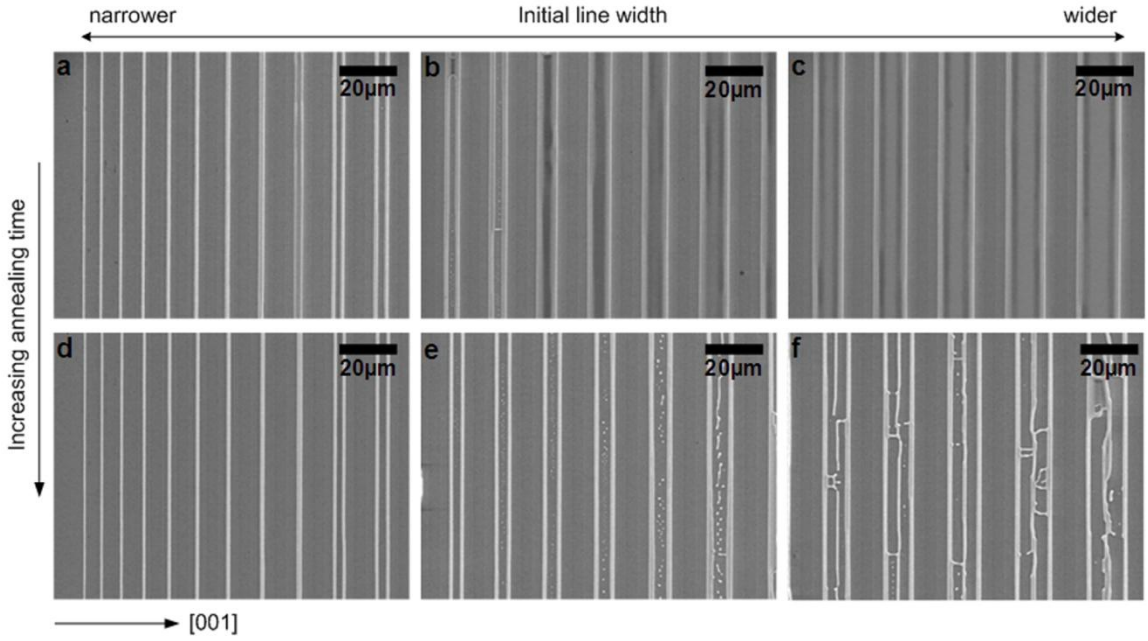

Figure 5-7. Retraction and pinch-off of long lines perpendicular to the $[001]$ direction. (a)-(c) Images of long lines annealed for 540 minutes. (d)-(f) Images of long lines annealed for 1020 minutes.

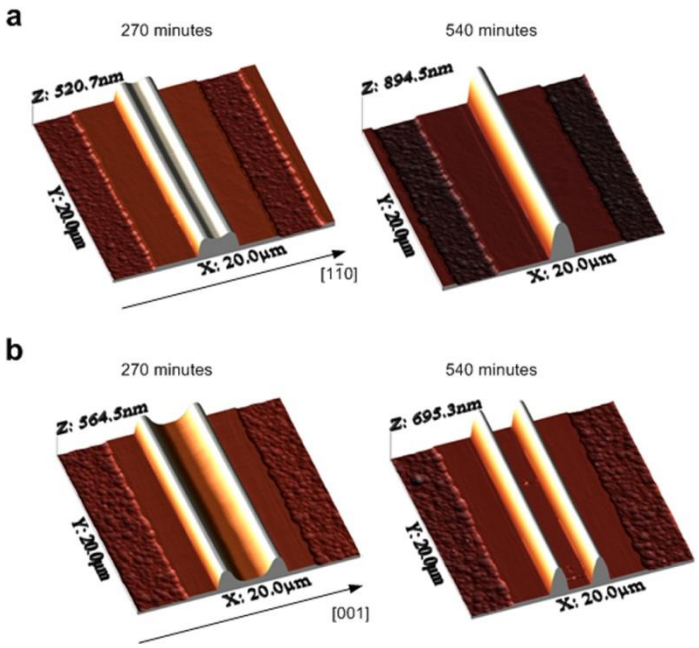

Figure 5-8. AFM images around the middle of evolving long line patches. (a) The patch with long edges perpendicular to the $[1\bar{1}0]$ direction. (b) The patch with long edges perpendicular to the $[001]$ direction. Annealing times are indicated in each image. The initial widths were 11.1 μm and 11.7 μm respectively.

The annealing ambient also affects the pinch-off phenomenon. Figure 5-9 shows the dewetting result of a square patch that was annealed at 900°C in a Transtemp tube furnace under a reducing gas flow rate of 90 sccm. Pinch-off did not occur under this annealing condition, as shown in Fig. 5-9, while it did when the flow rate of the reducing gas was much higher (2310 sccm), as shown in the top two rows of Fig. 5-1(a). We have shown in chapter 3 that the difference in the annealing ambient causes changes in surface energy anisotropy of Ni, leading to different facet morphologies of thickening rims. The top facet shown in Fig. 5-10(a) is wider than that shown in Fig. 5-10(b). This implies that cusps at {110} become deeper when the flow rate of the reducing gas is lower and the surface coverage of oxygen absorbates is higher. Dornel et al. [12] have modeled the effects of surface energy anisotropy on the rate at which valleys deepen, and found that when the top facet of a rim has a low energy (and therefore a large area), the deepening rate is low. The pinch-off phenomena seen in Figs 5-1 and 5-9 are consistent with the Dornel's analyses.

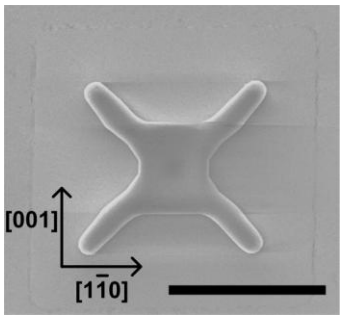

Figure 5-9. Dewetting of a square patch patterned from a Ni(110) film. The annealing was carried out in a Transtemp furnace under a reducing gas flow rate of 90 sccm. The initial width was about 17.6 μm. The annealing time was 1020 minutes. Scale bar indicates 10 μm.

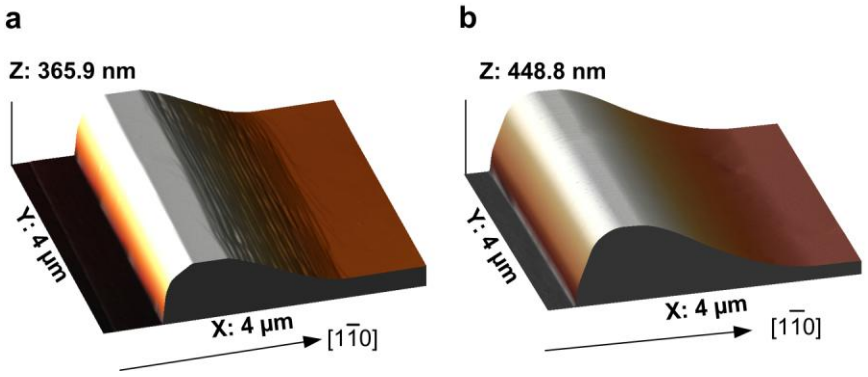

Figure 5-10. The shapes of thickening rims. (a) Annealed in a Transtemp furnace at 90 sccm for 318 minutes. (b) Annealed in a Lindberg/Blue Mini-Mite furnace at 2310 sccm for 270 minutes.

5.3.2 Ni(100) film

Figure 5-11 shows results of dewetting of square patches with edges oriented in the <001> directions and with different widths, all of which were patterned from a Ni(100) film. As seen in Figs. 5-11(a) to 5-11(d), edge retraction is slower near the corners than in other parts of dewetting patterns, leading to formation of arms at the corners in a similar manner to what was shown in Figs. 5-1(a) to 5-1(d) for a Ni(110) film. However, in large patches (e.g. the top two rows of AFM images of Fig. 5-11), edges become unstable and retract relatively faster adjacent to arms at the pattern corners than in other parts of the edges. This edge instability can be understood in terms of the variation in height of thickening rims. Figures 5-12(a) and 5-12(b) shows a plan view and a 90-degree tilted view of the dewetted pattern. As seen in the figure, thickening rims become lower adjacent to arms at the pattern corners than in other locations. Since the gradient in surface curvature is larger across thinner rims, the edge retraction velocity becomes higher adjacent to the arms.

The most significant difference in the dewetting process of patterned Ni(100) and Ni(110) films is associated with the pinch-off phenomenon. Pinch-off does not occur during dewetting of patches patterned from a Ni(100) film. This result can also provide evidence of the effect of surface energy anisotropy on the pinch-off phenomenon. It has been shown that the surface energy of Ni is lower at {100} orientations than at {110} orientations [54, 64]. As seen in Fig. 5-13, the top facet of a thickening rim in Ni(100) films is wider than those shown in Figs. 5-4(c) and 5-4(d). The top surfaces of dewetted line structures are also found to be wider in Ni(100) films than in Ni(110) films, as clearly seen in comparing Fig. 5-11(h) to Fig. 5-1(h). This also implies that Ni(100) faces have lower surface energies than Ni(110) faces. Given the anisotropy of surface energy and observed morphologies during dewetting, the difference in the pinch-off phenomenon between the patterned Ni(110) and Ni(100) film is also seen to be associated with surface energy anisotropy of Ni.

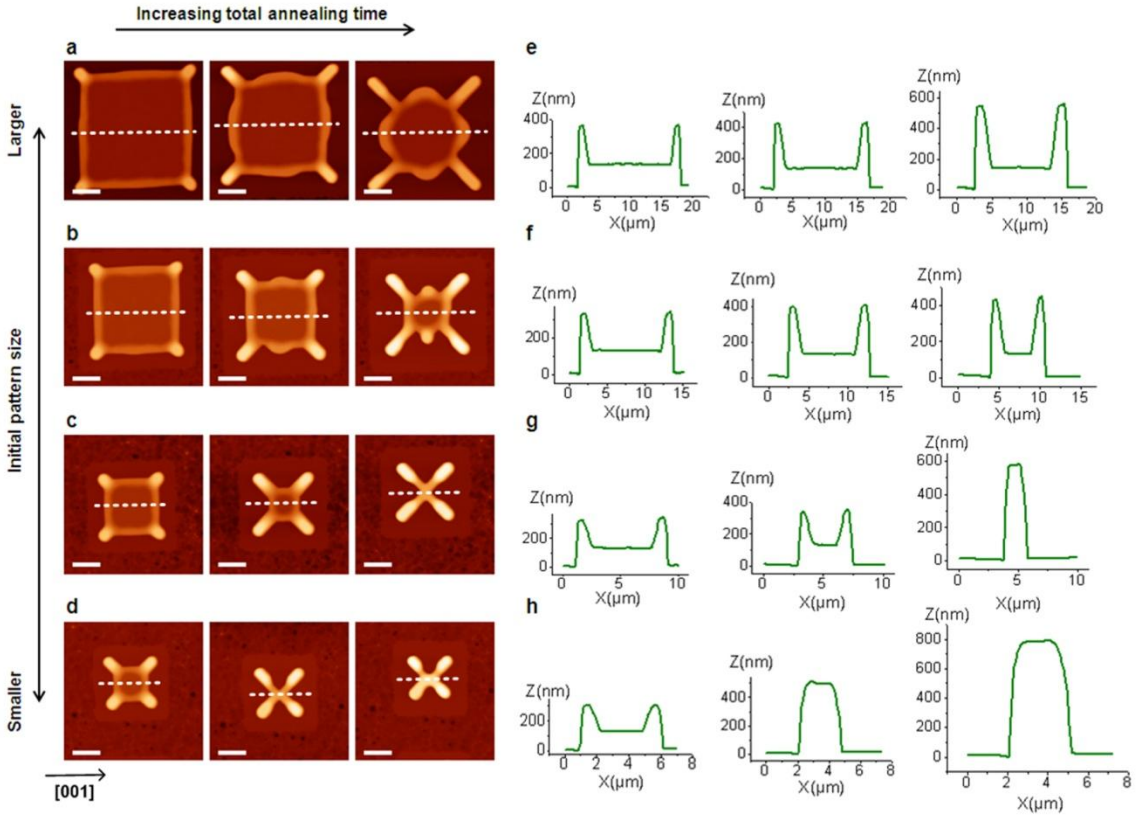

Figure 5-11. Dewetting of square patches patterned from a Ni(100) film. (a)-(d) AFM images of evolving square patches with various initial sizes. The initial edge length of each patch was about 19.3, 15.4, 11.6, and 9.7 μm respectively. The total annealing time was 270 minutes, 540 minutes, and 1020 minutes from the left to the right panel. The in-plane crystallographic orientation is indicated in the lower-left corner. Scale bars, 4 μm. (e)-(h) Height profiles for each of the patterns on the left. The height profiles were measured along the dashed lines in the AFM images.

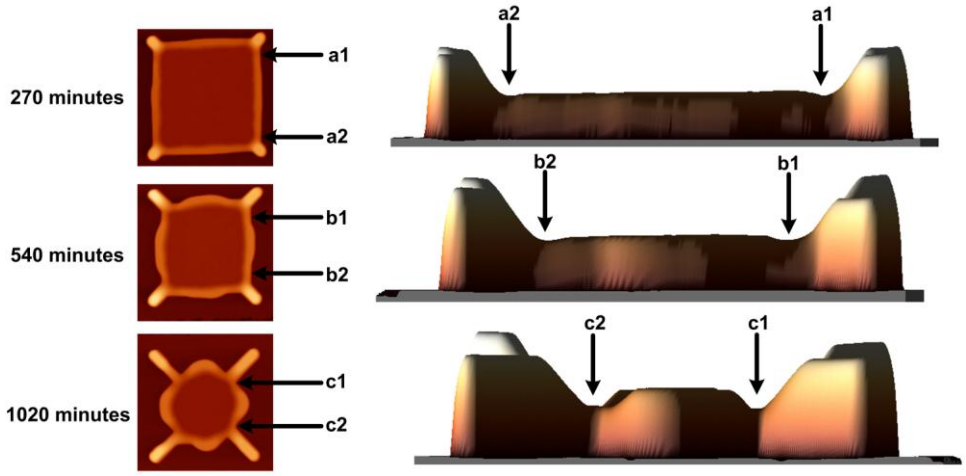

Figure 5-12. AFM images showing the variation in height along thickening rims of the dewetting pattern shown in Fig. 5-11(a). Both top-view (left-side) and the 90-degree tilted-view (right-side) images are shown. Arrows indicate relatively low parts of thickening rims. The annealing times are indicated on the left.

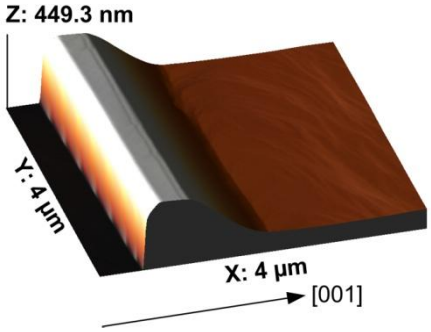

Figure 5-13. AFM image showing the shape of a thickening rim along a long retracting edge in a Ni(100) film. The annealing time was 318 minutes.

5.3.3 Numerical simulation using the crystalline method

We have shown that the pinch-off phenomenon depends on the thickness-to-width ratio of a patterned film and on the anisotropy of the surface energy. In this section, we will further demonstrate the effects of the thickness-to-width ratio of the film and the

anisotropy of surface energy on pinch-off phenomenon via a numerical simulation. As mentioned earlier, Dornel's numerical model [12] analyzed the effects of the thickness-to-width ratio of the film, the equilibrium contact angle at a three-phase boundary, and the anisotropy of the surface energy on the number of agglomerates that form via the pinch-off process, for isotropic and anisotropic surfaces with smoothly varying surface normals. The results of Dornel's analyses showed that the pinch-off process is favored as the thickness-to-width ratio of the film, equilibrium contact angle, and the surface energy of the film's top surface become larger. For faceted surfaces, Dornel investigated the effect of the anisotropy of surface energy on the valley deepening rate and found that the valley deepening rate becomes lower and pinch-off is delayed, as the top facet of a thickening rim becomes wider. However, for the case of faceted surfaces, Dornel et al did not provide a systematic investigation of pinch-off phenomenon

We model the capillary-driven surface evolution of 2-dimensional cross-sections of films with highly anisotropic surface energy using the crystalline method developed by Carter et al [2]. This simulation was carried out using Mathematica in collaboration with Prof. Carter and Victor Brunini.

The crystalline method assumes that the surface is completely faceted, and that crystal shapes can be described using a group of facets. As mentioned earlier, for isotropic surfaces, the chemical potential of surface atoms is proportional to the local curvature, and the gradient in the local curvature therefore drives the surface diffusion that results in surface evolution. Since the surface profile can be described as a smoothly varying function for isotropic surface energy, local curvature is simply defined as the

second derivative of the function. For anisotropic surface energy, surface motion is governed by a weighted curvature [65]. Because the faceted surface is not described as a single function, the formula for weighted curvature is derived in a specific way in the crystalline method. Taylor [65] derived an expression for the weighted curvature κ_i^{γ} of facet e_i (with the facet normal direction is n_i) in a completely faceted crystal, given by

$$\kappa_i^{\gamma} = \frac{\sigma_i \Lambda(n_i)}{L_i} \tag{5-2}$$

where L_i is the length of facet e_i, $\Lambda_i(n_i)$ is the length of the facet that has the normal direction of n_i in the Wulff shape, σ_i is a convexity factor. σ_i has a value of +1, 0, or -1 depending on how facet e_i meets its two neighbor facets, facets e_{i-1} and e_{i+1}. Figure 5-14 is a schematic illustration showing the meanings of the parameters in Equation 5-2.

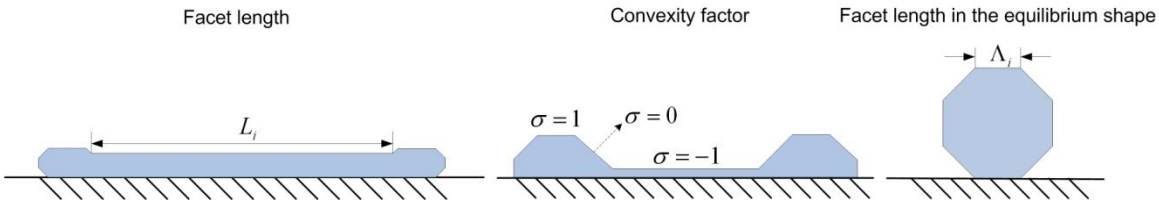

Figure 5-14. Descriptions for parameters in Equation 5-2.

In the crystalline method of Carter et al. [2], the shape evolution of completely faceted crystals occurs through the motion of each facet until the weighted curvatures of all facets have an identical value. Motion of facets is driven by the gradient in chemical potential that varies along the facet surface. Assuming that facets maintain their normal directions during their motion, the velocity v_i of facet e_i is given by

$$v_i(t) = -\frac{\partial}{\partial s} J_i(s,t) \neq f(s), \tag{5-3}$$

where s is the position along a facet e_i and J_i is the flux along facet e_i. The flux J_i along facet e_i is given by Fick's first law as follows

$$J_i(t) = -D_i \frac{\partial}{\partial s} \mu_i(s,t) \ , \tag{5-4}$$

where $\mu_i(s,t)$ is the chemical potential along a facet e_i and D_i is the surface diffusivity of for facet e_i. The expression for the chemical potential along a facet e_i is derived by integrating Equations 5-3 and 5-4,

$$\mu_i(s,t) = \mu_i - \frac{J_i}{D_i} s + \frac{v_i}{2D_i} s^2 . \tag{5-5}$$

The following equations for the chemical potential and flux at corners where facets meet are derived by requiring continuity at corners for Equations 5-4 and 5-5,

$$\mu_{i+1} = \mu_i - \frac{J_i}{D_i} L_i + \frac{v_i}{2D_i} L_i^2 \tag{5-6}$$

$$J_{i+1} = J_i - v_i L_i, \tag{5-7}$$

where μ_i, μ_{i+1} and J_i, J_{i+1} are the chemical potentials and fluxes at s=0 of facets e_i and e_{i+1}. In two-dimension, the weighted curvature is the local rate of surface energy change with a local addition of area. Therefore, when a facet moves a distance *dx*, the change of surface energy associated with this movement is $\kappa_i^{\gamma} L_i dx$. This energy change has the same value as the energy change upon incorporation of atoms into the crystal, which is $dx \cdot \int_0^{L_i} \mu_i(s) ds$. Therefore, we get the following equation

$$\kappa_i^{\gamma} = \frac{\int_0^{L_i} \mu_i(s,t)ds}{L_i} \quad . \tag{5-8}$$

Substituting Equation 5-5 into Equation 5-8, we get the expression for the velocity v_i of facet e_i,

$$v_i = \frac{6D_i(\kappa_i^{\gamma} - \mu_i) + 3J_iL_i}{L_i^2} \quad . \tag{5-9}$$

If the number of facet is N, there are 3N unknown values ($\mu_1, \mu_2 ..., \mu_N$, $J_1, J_2 ..., J_N$, and $v_1, v_2 ..., v_N$) to calculate and 3N equations obtained from Equations 5-6, 5-7, and 5-9. Therefore, we can calculate the motion of each facet by solving the 3N equations.

In this crystalline model, a perturbation on a facet occurs via stepping, by which a vanishingly small facet is inserted in the middle of the original facet, dividing the original facet into three facets. The insertion of steps is considered only at specific locations where the chemical potential does not change upon the insertion. Given that the weighted curvature of a step is zero, the specific locations are those where the chemical potential is zero. This crystalline model gives the criterion for the growth of the step. According to this model, inserted steps grow in time step only if the following condition is satisfied,

$$\sigma_{s-1} \int_0^{S_0} \mu_i(s)ds > \Lambda(n_{s-1}) \ , \tag{5-10}$$

where S_0 is the location where the chemical potential of the facet is zero. Once the step begins to grow and has a finite length, new chemical potentials are calculated for all facets, because there is a topological change.

We simulated the shape evolution of 2-dimensional thin films with the initial shape described in Fig. 5-15(a). When the initial films are not in an equilibrium state, they evolve to reach the equilibrium state via surface diffusion driven by the gradient in local weighted curvature along the surface of the films. The equilibrium shape for the two-dimensional film on a substrate is given by the Winterbottom construction [1]. The equilibrium shape defined by the Winterbottom construction depends on the adhesion energy between the film and substrate, which is given by $\gamma_{fv} - (\gamma_{fs} - \gamma_{sv})$ where γ_{fv} is the surface energy of the film, γ_{fs} is the interfacial energy between the film and substrate, and γ_{sv} is the surface energy of the substrate. Fig. 5-15(b) represents the equilibrium shape of a 2-dimensional film in the non-wetting situation, which indicates that the adhesion energy is zero. We investigated the effect of the initial width of a film and the anisotropy of surface energy on the pinch-off phenomenon by varying the values of W in the initial shape and Λ_1 / Λ_2 in the equilibrium shape. In the simulation, it is assumed that the diffusivity at the interface between the film and substrate is much lower than the surface diffusivity.

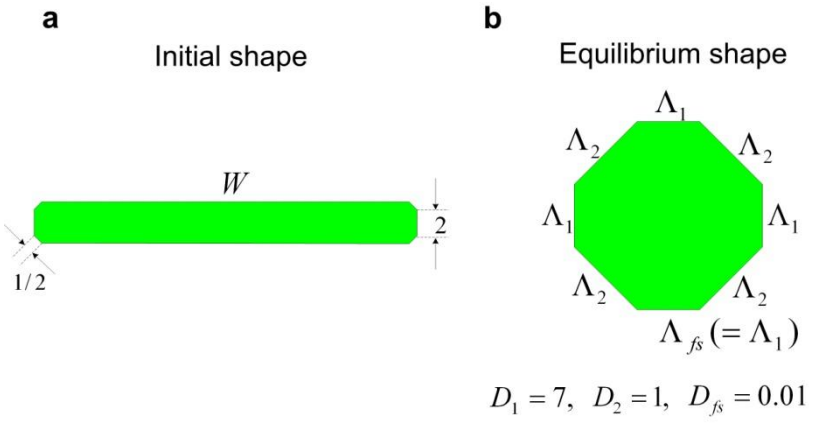

Figure 5-15. Schematic illustration showing (a) the initial shape and (b) the equilibrium shape of a 2-dimensional thin film whose evolution is simulated. The bottom facet is attached to the substrate.

Figure 5-16 shows a simulation result for different values of *W*. The shape evolution of the film begins with the retraction of edges and the development of thickening rims. As seen in the figure, films evolve into different numbers of agglomerates that depend on the initial width of the films for a given value of Λ_1 / Λ_2. The thickening rims merge and form a single agglomerate before the film surface touches the substrate surface in the case that the initial film width is not sufficiently large. This result is consistent with results showing the effect of the initial distance of separation of edges on the pinch-off phenomena presented in the previous sections (see Figs. 5-1, 5-6 and 5-7).

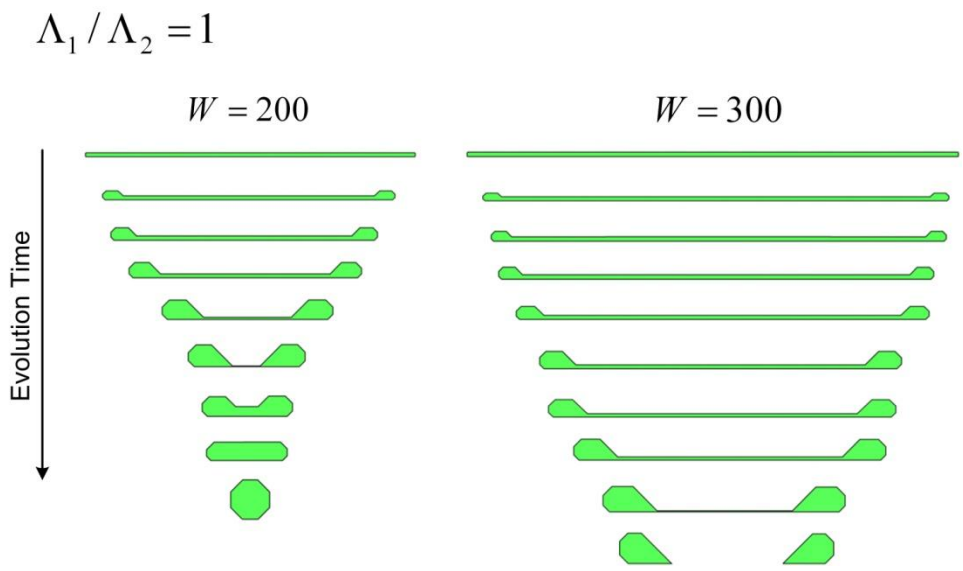

Figure 5-16. Simulation example showing the effect of the initial film width on the pinch-off phenomenon during evolution of two films.

We also simulated the evolution of films with the same width but different values of Λ_1 / Λ_2, to investigate the effect of the anisotropy of surface energy on the pinch-off phenomenon. Figure 5-17 shows the simulation result for a given initial width and two different values of Λ_1 / Λ_2. As seen in the figure, pinch-off occurs and two separate agglomerates form when the value of Λ_1 / Λ_2 is 0.5, while the thickening rims merge to form a single agglomerate when the value of Λ_1 / Λ_2 is 1.

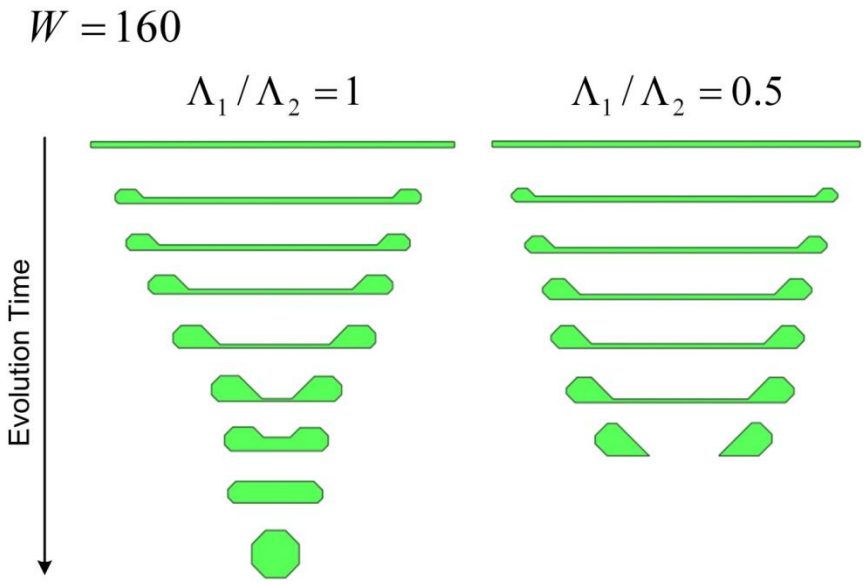

Figure 5-17. Simulation example showing the effect of the anisotropy of surface energy on the pinch-off phenomenon during evolution of two films.

Simulation results for more various values of W and Λ_1 / Λ_2 are summarized in Fig. 5-18. Pinch-off of a film edge occurs only when the initial width of the film is wider than a certain value, which becomes larger as the value of Λ_1 / Λ_2 becomes larger. Given that the larger value of Λ_1 / Λ_2 implies a larger facet width and therefore the lower surface energy of a top facet, this plot shows that the pinch-off process of an edge is suppressed as the surface energy of the top surface of a film becomes lower. This simulation result is consistent with the experimental results presented in the previous sections, which show the influence of the width of a top facet in a thickening rim on the pinch-off phenomenon.

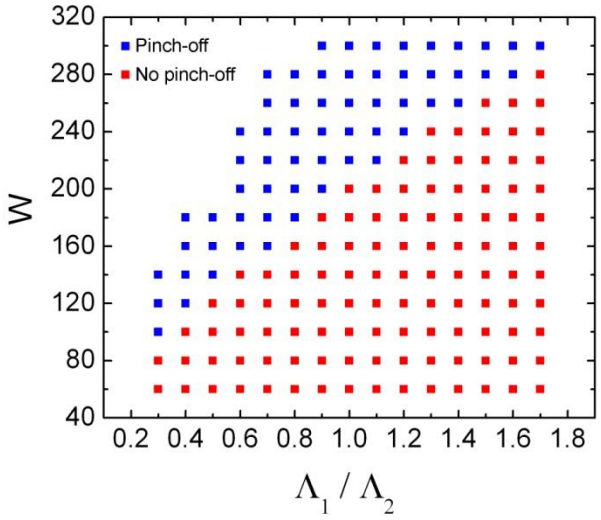

Figure 5-18. Dependence of the pinch-off phenomenon on the initial width of a film and the surface energy anisotropy.

We also characterized the effect of the surface diffusivity on the pinch-off phenomenon by varying the ratio of the surface diffusivities D_1 and D_2 shown in Fig. 5-15. For a given value of D_1/D_2, the pinch-off behavior is found to be the same for different magnitudes of D_1 and D_2. Figure 5-19 shows the results of simulations carried out to investigate the effect of the value of D_1/D_2 on the pinch-off phenomenon for two different values of Λ_1 / Λ_2. The different results seen in Figs. 5-19(a) and 5-19(b) also show the effect of the anisotropy of surface energy on pinch-off phenomenon, which is consistent with the result shown in Fig. 5-18. For a given value of Λ_1 / Λ_2, the pinch-off is favored as the value of D_1/D_2 increases at relatively small values of D_1/D_2, while the pinch-off behavior becomes almost independent of the value of D_1/D_2 at relatively large values of D_1/D_2. This indicates that the relative magnitude of the valley deepening rate-

to-edge retraction velocity becomes larger as the value of D_1/D_2 is larger at relatively small values of D_1/D_2, but that the relative magnitude of the valley deepening rate-to-edge retraction velocity becomes independent of the value of D_1/D_2 at relatively large values of D_1/D_2.

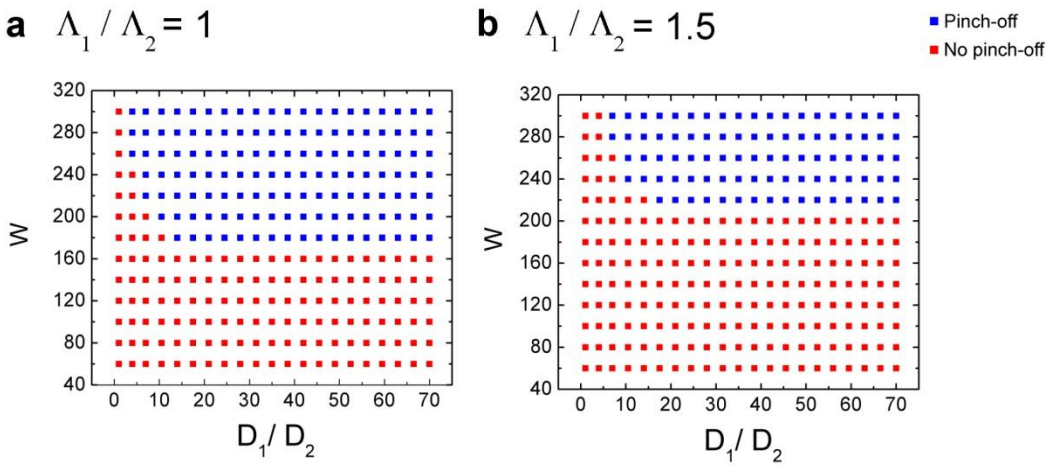

Figure 5-19. Dependence of the pinch-off phenomenon on the initial width and surface diffusivity of a film

The adhesion energy between the film and substrate also affects the pinch-off phenomenon. Figure 5-20 shows a simulation result in a partial-wetting situation. In this case, the adhesion energy equals to $\frac{1}{\sqrt{2}}\Lambda_2$. This film evolves into a single agglomerate while the film with the same value of W and Λ_1 / Λ_2 evolves to form two agglomerates through pinch-off when the adhesion energy is zero, as shown in Fig. 5-16. This shows that high adhesion energy between the film and substrate can also suppress the pinch-off process. As mentioned earlier, Dornel et al. showed that the pinch-off phenomenon is

favored as the equilibrium contact angle at a three-phase boundary becomes larger, for isotropic and anisotropic surfaces with smoothly varying surface normals. Given the values of the equilibrium contact angle shown in Figs 5-16 and 5-20, this result is consistent with the effect of the equilibrium contact angle on the pinch-off phenomenon in films with smoothly varying surface normals. Simulation results for various values of the initial width W and adhesion energy W_{ad} are summarized in Fig. 5-21. As in the case of isotropic surface energies, pinch-off is favored as the adhesion energy between the film and substrate decreases, as shown in the figure.

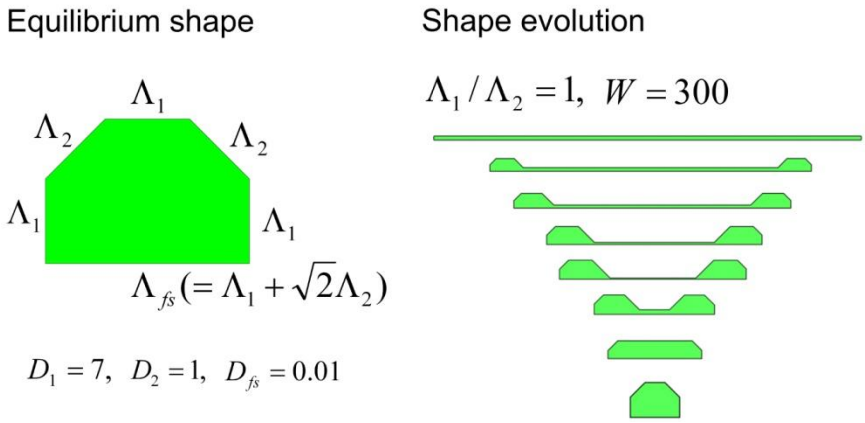

Figure 5-20. The equilibrium shape and simulation result in a partial wetting condition. Compare the result on the right to the result on the right in Fig. 5-16.

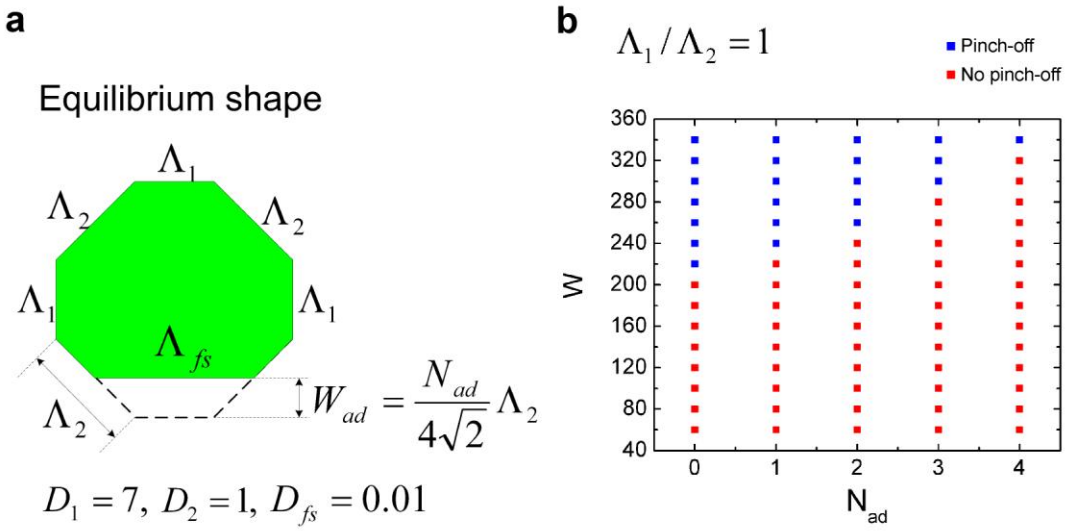

Figure 5-21. Dependence of the pinch-off phenomenon on the initial width of a film and the film-substrate adhesion energy. (a) The equilibrium shape. W_{ad} indicates the adhesion energy between the film and substrate. (b) The simulation result.

As discussed earlier, the edge retraction velocity can also affect the pinch-off phenomenon because it will determine the time at which two parallel edges begin to interact at a given valley deepening rate. Figure 5-22 shows the effect of surface energy anisotropy on the edge retraction velocity. The equilibrium shape and diffusivity are set to be the same as those shown in Fig. 5-15. As seen in this figure, the edge retraction velocity becomes lower as the value of Λ_1 / Λ_2 is decreased. Given that pinch-off was found to be favored as the value of Λ_1 / Λ_2 was decreased, this result suggests that the difference in the edge retraction velocity shown in Fig. 5-22 also plays a role in determining the different pinch-off behaviors shown in Figs. 5-17 and 5-18. It should be noted that the early-stage edge retraction velocity decreases with time due to rim thickening and the data in Fig. 5-22 are well-fit by a power-law with an exponent of

around 0.4. This is consistent with Wong's calculation for isotropic surface energies and our experimental results. The jump in the velocity occurs when two thickened rims coalesce (e.g. around t=20000 in the case that Λ_1 / Λ_2 is 0.8). The velocity eventually saturates due to pinch-off or formation of the equilibrium shape.

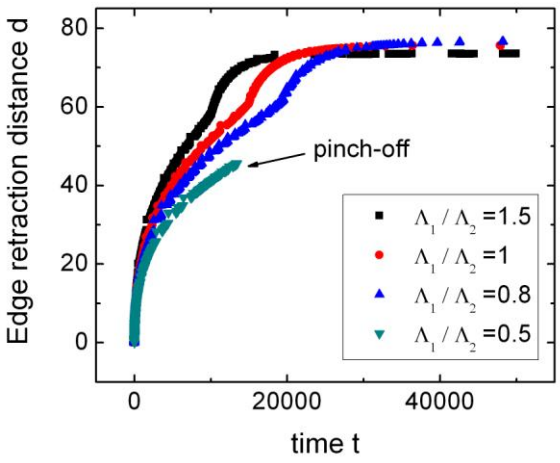

Figure 5-22. The edge retraction distance versus time in the different conditions of surface energy anisotropy. The edge retraction distance at time t is calculated by dividing the change in length of the film-substrate interfacial facet by 2.

5.4 Summary

In this chapter, studies of dewetting of patterned single crystal Ni films were discussed, mainly focusing on the pinch-off behavior of retracting edges. We reported that square and cross patches with various initial sizes patterned from 120 nm-thick single crystal Ni(110) films, evolve to regular line structures through the retraction and pinch-off of edges during solid-state dewetting. By analyzing the morphological evolution, we have shown that the pinch-off behavior strongly depends on the pattern

geometry and the in-plane crystallographic orientation of the retracting edge. Differences in pinch-off behavior for patterns with the same geometry but different crystallographic orientations are associated with differences in surface energy anisotropy along different edges. Further, we have shown that because of the lower valley deepening rate and higher edge retraction velocity at concave corners, a smaller number of lines develop in regions where concave corners approach each other. Differences in edge retraction at corners are associated with the increased (concave) or decreased (convex) areas for diffusive mass redistribution. Morphological evolution during dewetting of long line patches was also analyzed to study pinch-off behavior decoupled from the effects of corners. The pinch-off phenomena during dewetting of these patches were consistent with the effects of pattern geometry and crystallographic orientations seen in the evolution of square and cross patches.

We investigated the effect of surface energy anisotropy on the pinch-off phenomenon in more detail by observing the differences in the facet morphologies of thickening rims and in the pinch-off phenomenon during dewetting of square patches at two different flow rates of reducing gas. It was found that the top facet of a thickening rim is wider and the pinch-off process is suppressed as the flow rate of a reducing gas is lower. We also observed morphological evolution during dewetting of square patches patterned from a 120 nm-thick Ni(100) film, and showed that pinch-off of edges does not occur regardless of the initial sizes of the square patches. At a given flow rate of reducing gas, the top facet of a thickening rim was found to be wider in Ni(100) films than in

Ni(110) films. These results suggest that the pinch-off is suppressed as the surface energy of the top surface of the film becomes lower.

We also analyzed the experimentally observed effects of the initial film width and surface energy anisotropy on the pinch-off phenomenon by carrying out a numerical simulation of the evolution of the 2-dimensional films. The simulation results were qualitatively consistent with our experimental results in terms of the effects of these parameters on the pinch-off phenomenon. We also characterized the effects of film-substrate adhesion energy and demonstrated that high adhesion energy suppresses the pinch-off process. It was also numerically shown that pinch-off is favored as the ratio of the surface diffusivity on the top surface of a film relative to other surfaces increases, but that the pinch-off behavior becomes independent of the ratio for large values of the ratio.

Chapter 6

Templated solid-state dewetting to controllably produce complex patterns

6.1 Introduction

In chapter 1, we introduced recent results that reported the formation of ordered structures via solid-dewetting of thin films. The ordered structures could be obtained by imposing geometric or crystallographic constraints on the film evolution. Giermann and Thompson [26] reported that dewetting of gold films deposited on substrates with an inverted pyramidal topography resulted in formation of spatially-ordered and crystallographically-aligned gold nanoparticles. It has also been shown that single crystal nickel and silicon-on-insulator (SOI) thin films evolve to regular morphologies during dewetting due to crystallographic constraints on the shapes of holes and islands [32-36, 39, 40]. In this chapter, we discuss experiments in which geometric constraints as well as crystallographic constraints on the dewetting process were imposed by pre-patterning single crystal nickel films to produce various regular structures. We characterize the effects of these constraints on regular morphological characteristics of dewetted structures by analyzing morphological evolution during dewetting of patches with various initial shapes patterned from single crystal Ni(110) and Ni(100) films.

6.2 Experimental

We deposited 120 nm-thick single crystal Ni(110) and Ni(100) films on MgO(110) and MgO(100) substrates. The deposition conditions were same as those described in the previous chapters. After the depositions, films were patterned into patches with various shapes via photolithography followed by wet etching of Ni. The pre-patterned films were annealed in a tube furnace at 900°C under a reducing gas (5% H_2 and 95% N_2) flow rate of 2310 sccm. We observed the results of morphological evolution of patches with various initial shapes using SEM. The SEM images were taken using an FEI/Philips XL30 FEG ESEM.

6.3 Results and Discussion

6.3.1 Square patches oriented in various in-plane directions

We patterned Ni films into polar arrays of square patches with or without internal holes, as shown in Fig. 6-1, to investigate the effect of initial in-plane crystallographic alignments on the shapes of dewetted structures. In this section, we will show and discuss results for full square patches. Results for square patches with internal holes will be shown in the next section.

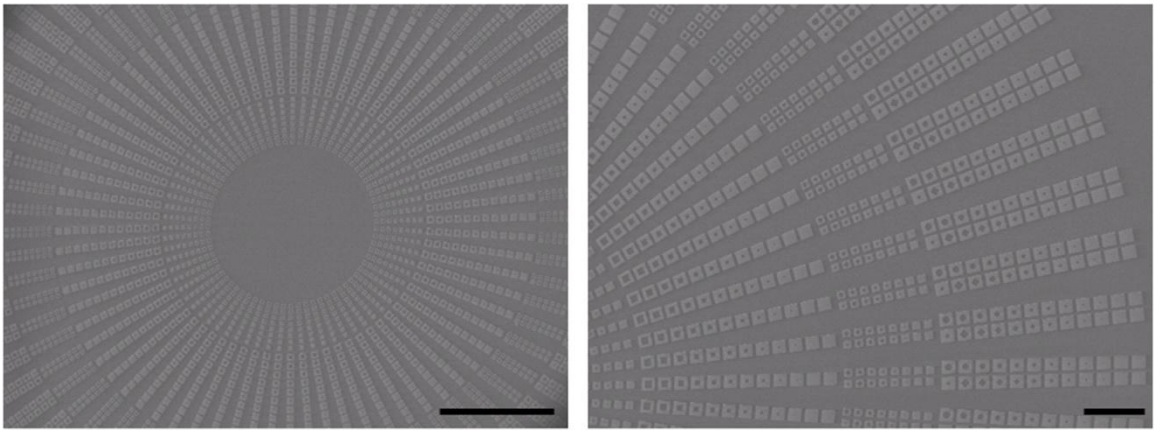

Figure 6-1. A polar array of square patches with or without internal holes. Scale bar, 200 μm

Figures 6-2(a) and 6-2(b) show morphological evolution during dewetting of square patches with two different sizes and two different in-plane crystallographic alignments, all of which were patterned from a Ni(110) film. As seen in the figure, dewetting morphologies show regular characteristics that depend strongly on the initial sizes and in-plane crystallographic alignment of the patches. Morphological evolution of the patches begins with edge retraction and accumulation of material in thickening rims. As mentioned in the previous chapter, edge retraction is often slower near convex corners than in other parts of an edge due to the overlap of diffusion fields near the corners, which leads to increased accumulation of material and a consequent smaller driving force for retraction. The slower edge retraction near convex corners can be seen in all of the dewetting square patches shown in Figs. 6-2(a) and 6-2(b), and is seen to lead to formation of arms at corners of all square patches. However, the arms are significantly longer in patterns that had an initial in-plane rotation angle of 45° with respect to the <001> and <110> directions rather than a rotation angle of 0°. This can be understood in

terms of anisotropy of the edge retraction velocity in Ni(110) films. It was shown in chapter 3 that the edge retraction velocity is lower in the <001> and <110> directions than in other directions. Due to the anisotropy of the edge retraction velocity, as the directions of corner retraction become closer to the <001> and <110> directions, the retraction velocity will be even lower relative to other parts of the edges, eventually leading to the formation of longer arms.

Retracting edges subsequently pinch-off in certain patterns, leading to more complex morphological evolution. This pinch-off behavior also depends on the in-plane crystallographic directions of alignment of square patches. During dewetting of the small square patches seen in Fig. 6-2(a), pinch-off occurs and two separate lines form in the body of the patterns with an initial in-plane rotation angle of 45°, while pinch-off does not occur and only a single line forms for patterns with an initial in-plane rotation angle of 0°. This difference shows that the initial distance of separation of edges was sufficiently large to cause valleys to touch the substrate surface in the 45° case, but not in the 45° case. It has been shown in chapter 5 that the anisotropic nature of the pinch-off process is associated with surface energy anisotropy of thickening rims. However, in the case of large square patches, pinch-off eventually occurs to form separate lines for both sets of square patches, as shown in Fig. 6-2(b). This shows that the initial distance of separation of edges was sufficiently large to cause pinch-off for both rotation angles.

The continuous line patterns formed by retraction and pinch-off of edges break up and eventually evolve into isolated islands to further reduce their surface energy, due to a Rayleigh-like instability. This evolution can be seen in the second row of Fig. 6-2(a) (the

pattern that had an initial edge length of 12 μm and an initial in-plane rotation angle of 45°). As shown in the figure, lines become thicker in the arms than in the body of the patterns due to greater accumulation of mass around convex pattern corners during dewetting. Due to the uneven mass accumulation, the continuous line patterns break up where lines were thinner after being annealed for 1020 minutes.

Figures 6-2(c) and 6-2(d) show groups of dewetted patterns with four different in-plane crystallographic alignments including the two directions seen in Figs. 6-2(a) and 6-2(b). Square patches evolve to have long lines perpendicular to specific in-plane crystallographic directions such as the <001>, <110>, and <111> directions. It has been shown in chapter 3 that only thickening rims of edges perpendicular to these particular directions can expose {111} or {100} facets with low surface energy without being broken up into a mixture of facets along the line edge. This explains the greater complexity of the evolution of square patches whose initial alignments do not lie along these directions. It should be noted that the nature of the overall evolution is virtually the same for large numbers of identical initial patch shapes and alignments.

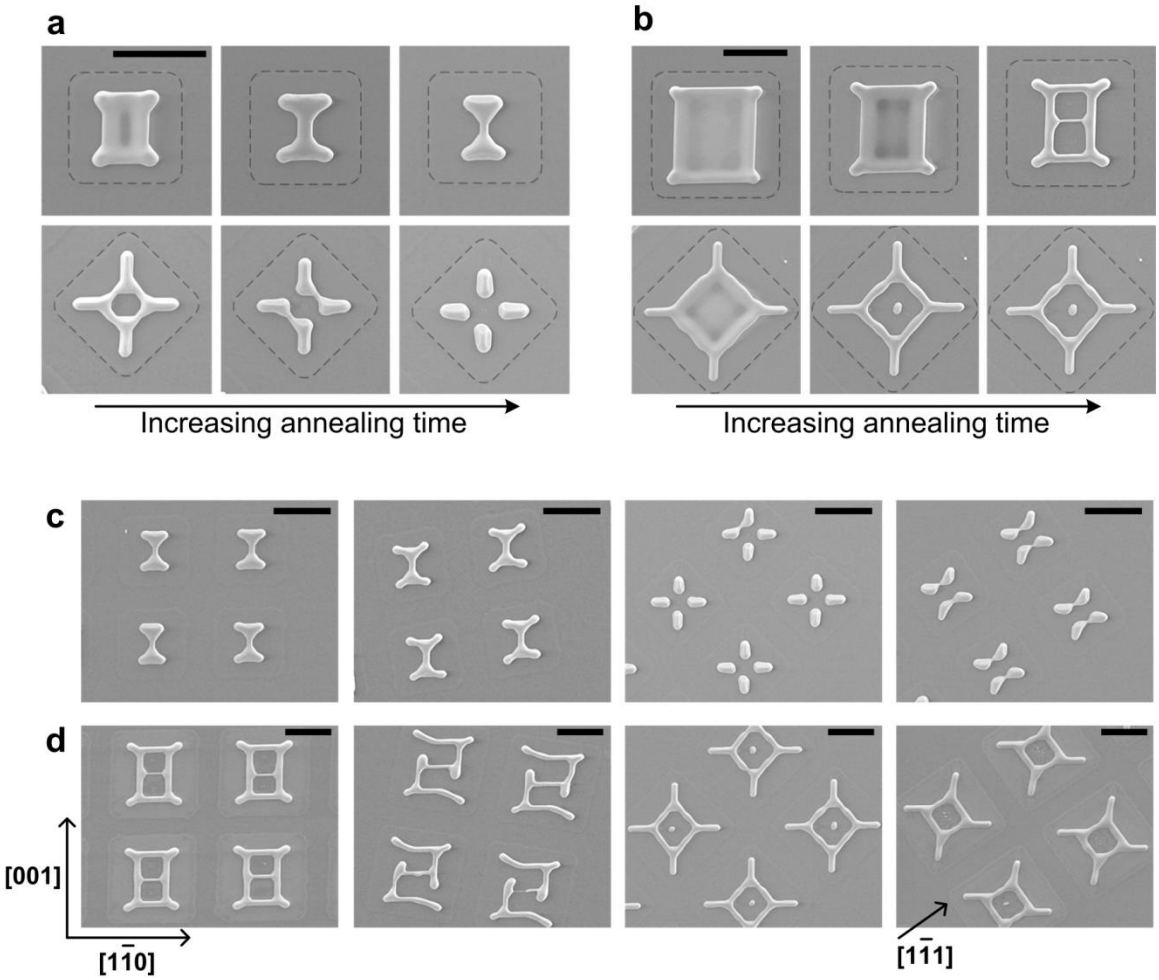

Figure 6-2. Dewetting of square patches with edges oriented in various in-plane crystallographic directions, all of which were patterned from a Ni(110) film. (a) and (b) SEM images of evolving square patches with two different in-plane orientations, (a) square patches with a relatively small initial size. The initial edge length was about 12 μm. (b) Square patches with a relatively large initial size. The initial edge length was about 19.7 μm. The total annealing time was 270 minutes, 540 minutes, and 1020 minutes from the left to right panel. The gray dashed lines indicate the initial shapes of the patches. (c) and (d) SEM images of a group of dewetted patterns with four different in-plane orientations. (c) The initial edge length was 12 μm and (d) the initial edge length was 19.7 μm. The total annealing time was 1020 minutes. The in-plane crystallographic orientations are indicated in the lower-left corner. Scale bars, 10 μm.

Figure 6-3 shows morphological evolution during dewetting of square patches that were patterned from a Ni(100) film. During dewetting, these square patches also evolve into various regular shapes that depend on their initial in-plane crystallographic alignments, as shown in Fig. 6-3(a). Formation of these regular shapes results from slower corner retraction, anisotropy of the edge retraction velocity, and in-plane faceting of edges as seen earlier in the dewetting of patterned Ni(110) films. However, pinch-off of edges does not occur during dewetting of these patches due to relatively low surface energy of {100} faces of Ni, as mentioned in chapter 5.

The anisotropy of the edge retraction velocity depends on the initial crystallographic orientation of a Ni film, as shown in chapter 3. In Ni(100) films, edge retraction is found to be slower in the <011> directions than in the <001> directions. As a result, long arms form at corners of patterns with edges initially aligned along the <001> directions, while arms have not formed at corners of patterns with edges aligned along the <011> directions. Furthermore, the dewetting structures have edges and lines aligned to specific in-plane orientations that are different from those seen in Fig. 6-2, because of the different crystallographic constraints for surface-energy minimization for films with (100) and (110) orientations. Consequently, the square patches in Fig. 6-3 evolve to have edges and lines perpendicular to the <011> directions or <001> directions during dewetting, as seen in the figure. Figure 6-3(b) also shows that the shapes of these dewetted patterns are the same for square patches with the same in-plane crystallographic alignments.

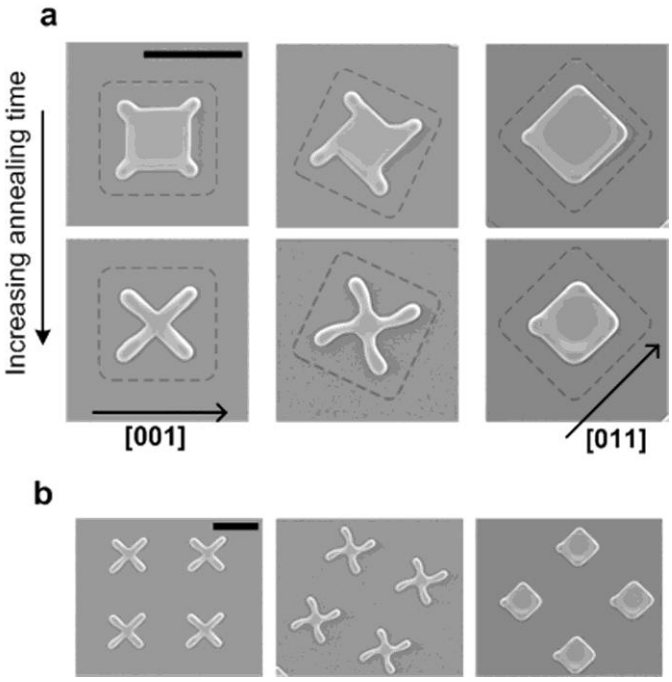

Figure 6-3. Dewetting of square patches patterned from a Ni(100) film. (a) SEM images of evolving square patches with three different in-plane orientations. The total annealing time was 270 minutes and 540 minutes from the top to bottom panel. The gray dashed lines indicate the initial shapes of the patches. The in-plane crystallographic orientations are also indicated. (b) SEM images of a group of dewetted patterns seen in (a). The total annealing time was 540 minutes. Scale bars, 10 μm.

6.3.2 Square patches with square and circular internal holes

We also observed dewetting of square patches with internal holes and investigated the effect of the initial crystallographic orientations of these patches on the shapes of dewetted structures. Figure 6-4 shows the dewetting results. As shown in this figure, the stability of square ring patterns during dewetting also depends strongly on their initial crystallographic alignments. Square ring patches with edges oriented in particular directions remain stable during dewetting while other square ring patterns break up to form isolated islands. This result can be understood in terms of the effect of surface

energy anisotropy on the Rayleigh-like instability of the lines that make up the square ring patterns. Cahn [17] evaluated the stability of a single crystal solid cylinder with surface energy anisotropy and derived an equation for the critical wavelength of the Rayleigh instability as a function of the initial surface orientation of a cylinder:

$$\lambda_{crit} = 2\pi R_0 \left(1 + \frac{1}{\gamma_s}\left(\frac{\partial^2 \gamma_s}{\partial \varphi^2}\right)\right)^{1/2},$$

where R_0 is the initial radius of the cylinder, γ_s is the surface energy of the cylinder, φ is the angle between the cylinder surface and the cylinder axis. Because the γ-plot of Ni shows prominent cusps and therefore large positive values of $\left(\frac{\partial^2 \gamma_s}{\partial \varphi^2}\right)$ at {111} and {100} orientations [54, 64], the critical wavelength will be especially large in the cylinders that expose {111} and {100} facets. As shown in chapter 3, for each out-of-plane orientation of a film, because of crystallographic constraints there are only a few particular in-plane crystallographic directions for which thickened rims can expose {111} or {100} facets. As shown in Fig. 6-4, the lines of the stable square rings are aligned with these particular in-plane crystallographic directions. Misalignment of initial patches with respect to these directions leads to earlier break-down of the ring structures through a Rayleigh-like instability with a smaller critical wavelength.

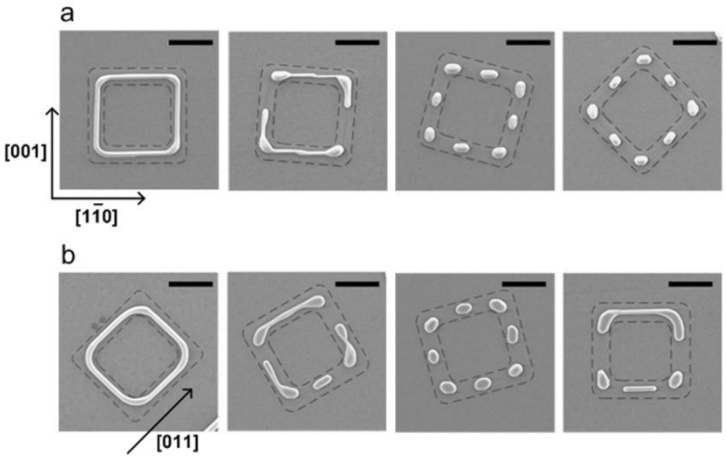

Figure 6-4. SEM images of dewetted structures that evolved from square ring patches with two different in-plane orientations. (a) Patterned from a Ni(110) film. (b) Patterned from a Ni(100) film. The total annealing time was 1020 minutes. The gray dashed lines indicate the initial shapes of the patches. The in-plane crystallographic orientations are also indicated. Scale bars, 5 μm

More dewetting results for square patches with internal holes are shown in Figs. 6-5 and 6-6 for different shapes and locations of internal holes. Figure 6-5 shows dewetting of square patches with internal circular holes that were patterned from a Ni(110) film. These patches also evolve into ring structures during dewetting, and the stability of the ring structures decreases as normals of their external edges deviate from the <001> and <110> directions. This is consistent with the results shown in Fig. 6-4(a), but the number of islands in decayed ring structures is found to be smaller. The smaller number of islands is associated with their circular initial shapes and smaller initial sizes. Due to the circular initial shapes and smaller initial sizes, the growth directions of internal holes are less constrained compared to those of the square holes shown in Fig. 6-4(a). The internal holes can therefore evolve to have long stable edges perpendicular to the <001> and <110> directions, as seen in Fig. 6-5. This leads to formation of long

stable lines perpendicular to the <001> and <110> directions even in off-orthogonal ring structures, and eventually results in a smaller number of islands than in the dewetted patterns shown in Fig. 6-4(a).

The initial location of an internal hole also affects the shape evolution of square patches in terms of the pinch-off behavior and break-down of lines, as seen in Fig. 6-6. The internal holes of the patterns shown in Fig. 6-6 had square initial shapes that were initially located in various off-centered positions. Pinch-off of edges occurred only in the patches that were initially most off-center in the [001] direction, as seen in the figure. This is consistent with the effect of the initial separation distances and in-plane directions of edges on the pinch-off behavior shown in chapter 5. Lines become thinner and break down near retracting concave corners of an internal hole. This is associated with less accumulation of material near concave corners of an internal hole. Because of the difference in the initial location of an internal hole in each patch of Fig. 6-6, line patterns break down at different locations.

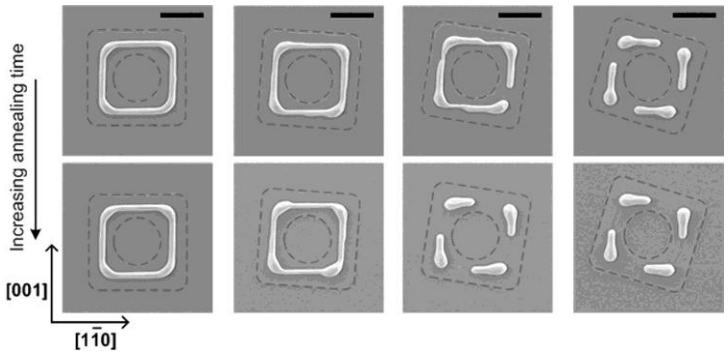

Figure 6-5. Dewetting of square patches with circular internal holes and with edges oriented in different in-plane crystallographic directions, all of which were patterned from a Ni(110) film. The total annealing time was 540 minutes and 1020 minutes from the top to bottom panel. The gray dashed lines indicate the initial shapes of the patches. The in-plane crystallographic orientations are indicated in the lower-left corner. Scale bars, 5 μm.

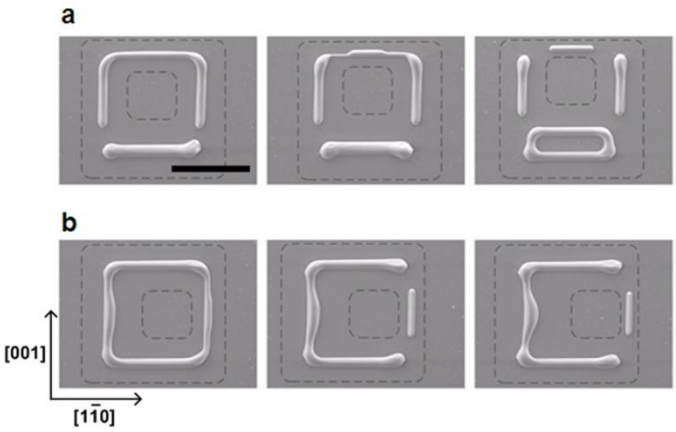

Figure 6-6. SEM images showing dewetting results for square patches with off-centered internal square holes, all of which were patterned from a Ni(110) film. (a) Off-centered in the $[001]$ direction. (b) Off-centered in the $[1\bar{1}0]$ direction. The annealing time was 1020 minutes. The gray dashed lines indicate the initial shapes of the patches. The in-plane crystallographic orientations are also indicated. Scale bars, 10 μm

6.3.3 Square and circular patches with inverted T-shaped internal holes

The effects of corners and locations of internal holes on dewetting behaviors of patches was further investigated by observing dewetting of patches with internal holes

that had both convex and concave corners. Figure 6-7 shows dewetting results for square and circular patches with inverted T-shaped internal holes, all of which were patterned from a Ni(110) film. As seen in the figure, the specific locations in which pinch-off occurs or line patterns break down are determined by initial locations of internal holes in these patches as well. Specific shapes of these dewetted structures can also be understood in terms of the mechanisms discussed earlier. Faster and slower hole growth at concave and convex corners also consistently affects the formation of line patterns with specific shapes. This result shows that the dewetting of patches can be precisely controlled to form line patterns with specific shapes by modulating locations and convexities of internal holes.

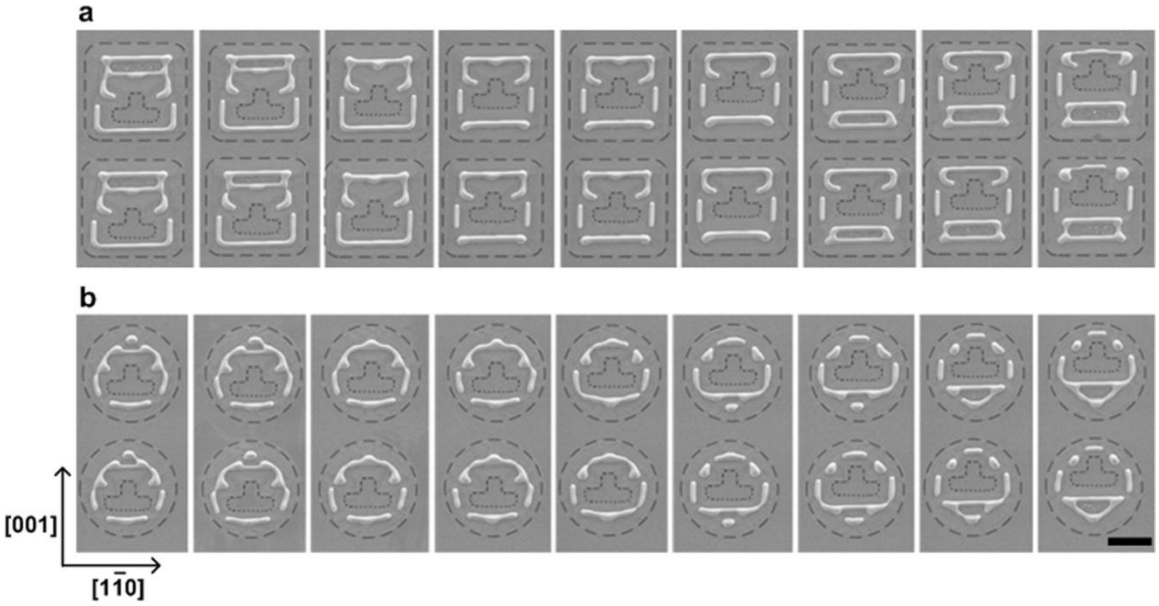

Figure 6-7. SEM images of (a) square and (b) circular patches with inverted T-shaped internal holes patterned from a Ni(110) film. The gray dashed lines indicate the initial shapes of the patches. The initial shapes were the same for patterns in the same column of each image. The position of the T-shaped internal holes within the patterns changes going from left to right. The in-plane orientation is indicated in the lower-left corner. The annealing time was 1020 minutes. Scale bar, 10 μm.

6.3.3 Cross patches with internal holes

The specific mechanisms of regular pattern formation discussed above are also observed during dewetting of cross patches with internal holes, and lead to formation of regular structures with greater complexity, as shown in Fig. 6-8. Figure 6-8 shows results of dewetting of cross patches with two different initial sizes and two different initial sizes of internal circular holes located at various locations, all of which were patterned from a Ni(110) film. As seen in the figure, the retraction of external edges of cross patches, growth of internal circular holes, and pinch-off of edges lead to formation of line patterns, and these line patterns subsequently break at retracting concave corners or internal hole corners near initially concave patch corners of dewetting cross patches. This can also be understood in terms of the nature of the diffusion field at concave corners. As mentioned earlier, material from long straight edges must diffuse in the direction normal to the edge. However, material diffusing from retracting concave corners can diffuse in many directions that radiate from the corner. The rim at concave corners is therefore smaller than the rim on straight edges, so that the retraction velocity is faster. Line patterns that form at the particular locations mentioned above are therefore thinner and decompose earlier. Afterwards, each broken part further dewets to become more widely separated. Figure 6-9 shows AFM images and height profiles in the earlier stage of dewetting of the cross patterns shown in Figs. 6-8(i) and 6-8(d). As shown in the figure, lines of dewetting cross patterns become thinner at the specific locations mentioned above than at other locations. Breakdown of the line patterns at the specific locations can be seen in Figs. 6-8(d) and 6-8(i).

In the patterns of Figs. 6-8(h) and 6-8(i), isolated islands form near the initial locations of internal circular holes. This is associated with the relatively large initial size of cross patches and relatively small initial size of the internal holes. The growth of internal holes will initially be less strongly affected by retracting external edges of the cross patches, as the initial internal holes are smaller and the initial cross patches are larger. Therefore, a corner-induced instability appears near the internal holes of the patterns seen in Figs. 6-8(h) and 6-8(i). Development of a corner-induced instability causes more mass accumulation at the centers of growing internal holes and eventually leads to formation of isolated islands.

Pinch-off behaviors seen in the patterns of Fig. 6-8 are consistent with results of dewetting of square patches seen in Fig. 6-2. As seen in Fig. 6-8, a larger number of lines form via the pinch-off process in larger cross patches because of the larger initial separation distances of the edges. A larger number of horizontal lines than of vertical lines seen in Fig. 6-8(f) also show the effect of the in-plane crystallographic orientation of the edges on the pinch-off behavior. This result is consistent with the in-plane anisotropy of the pinch-off phenomenon shown in chapter 5.

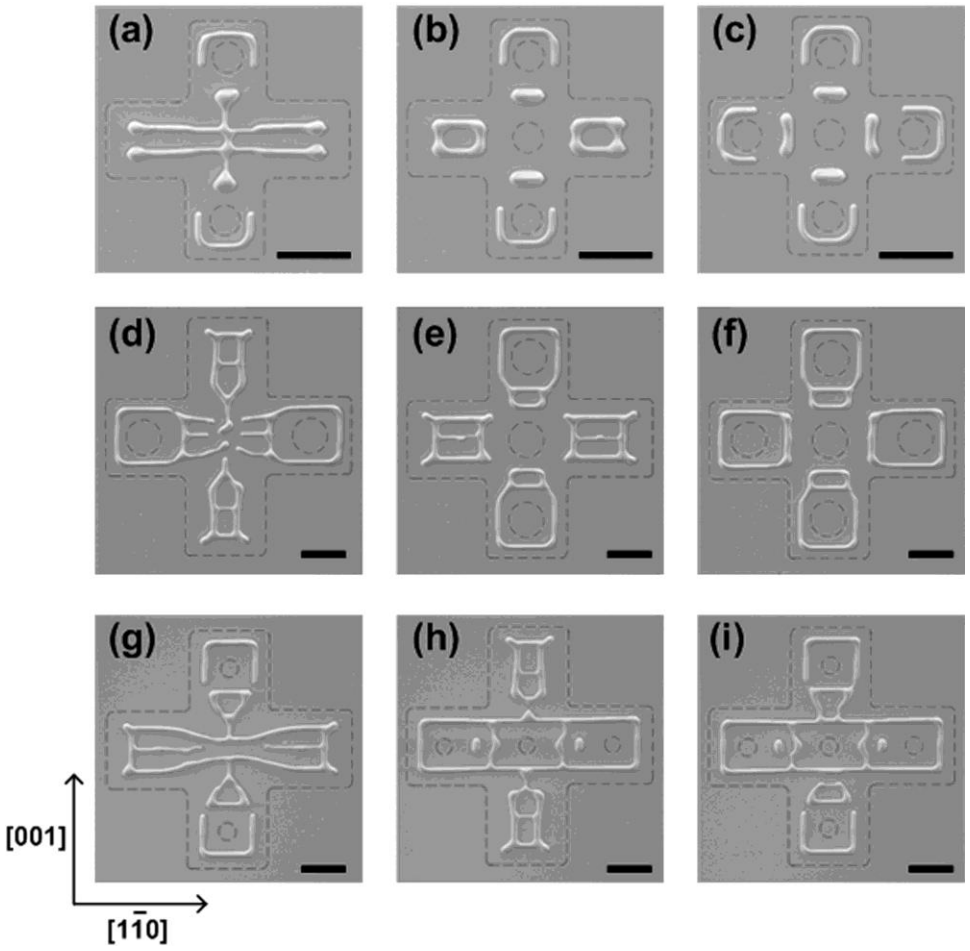

Figure 6-8. Dewetting of cross patches with pre-patterned internal circular holes patterned from a Ni(110) film. (a) through (c) are SEM images of dewetted patterns with an initial edge length of 10.8 µm. (d) through (i) are SEM images of dewetted patterns with an initial edge length of 18.4 µm. The gray dashed lines indicate the initial shapes of the patches. The in-plane orientation is indicated in the lower-left corner. The annealing time was 1020 minutes. Scale bars, 10 µm.

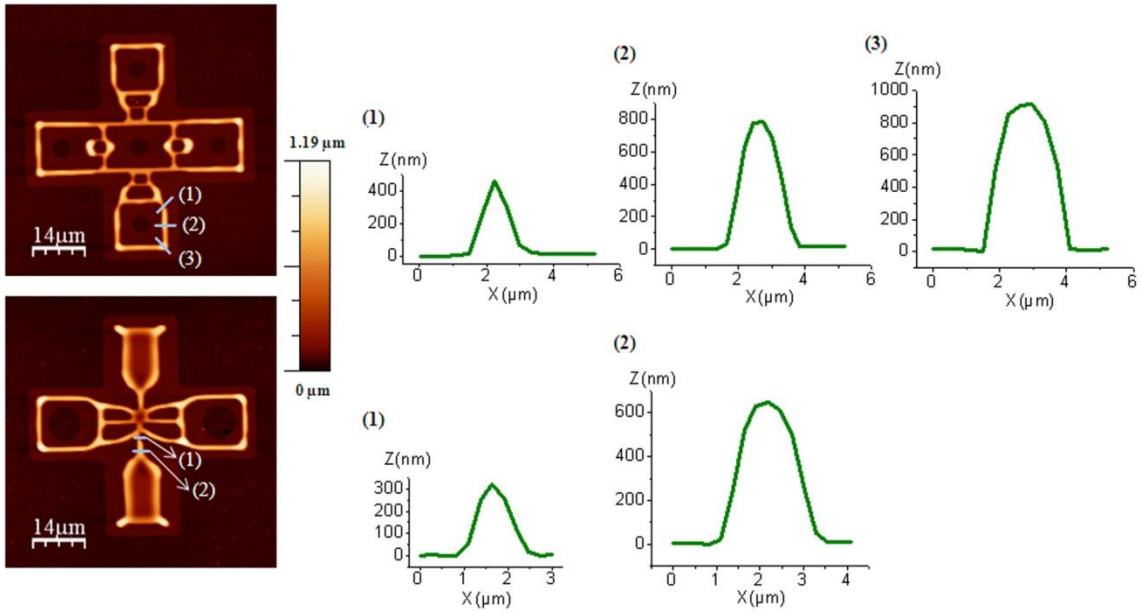

Figure 6-9. AFM images and height profiles of dewetting cross patterns. AFM images show the earlier-stage morphology of the pattern shown in Fig. 6-8(i) (upper image) and 6-8(d) (lower image). The annealing time was 540 minutes.

Figure 6-10 shows dewetting results for cross patches that were patterned from a Ni(100) film. The edge pinch-off seen in Fig. 6-8 does not occur in these patches. However, line patterns with regular shapes also form via retraction of external edges and growth of internal holes. Internal circular holes in the small cross patches of Figs. 6-10(a) to 6-10(d) grow to have concave corners with the same shapes as natural holes shown in chapter 4, unless their growth is strongly affected by retraction of external edges. Concave corners with a similar shape also form in the middle of arms without a circular hole, due to slower retraction of convex corners, as seen in Figs. 6-10(a) and 6-10(b). These concave corners retract in the <001> directions. The line patterns become thinner and eventually break at locations where the concave corners impinge. Breakdown of the

line patterns can also be seen between convex corners. This was also shown in Fig. 6-2(a). The locations at which these line patterns break are dependent on the initial shapes of the internal holes, because different hole shapes lead to the formation of concave corners at different locations, as seen in Figs. 6-10(g).

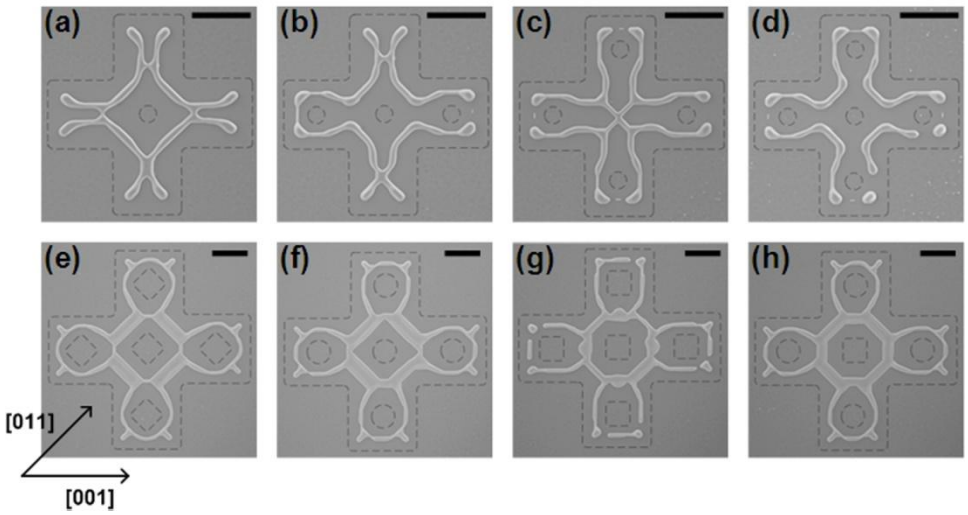

Figure 6-10. Dewetting of cross patches with pre-patterned internal holes patterned from a Ni(100) film. (a) though (d) are SEM images of dewetted patterns with an initial edge length of 11.6 μm. (d) through (i) are SEM images of dewetted patterns with an initial edge length of 19.2 μm. The gray dashed lines indicate the initial shapes of the patches. The in-plane orientation is indicated in the lower-left corner. The annealing time was 1020 minutes. Scale bars, 10 μm.

It should be noted that each complex dewetted structure shown in Figs. 6-8 and 6-10 was reproduced in arrays of cross patches with the same crystallographic and geometric characteristics. This further illustrates the ability to reproducibly create complex patterns through dewetting of single-crystal films with simpler, larger-scale initial patterns. The processes through which these complex patterns develop can be understood in terms of a finite set of mechanisms and phenomena that can be studied in

simpler structures. This provides the basis for the use of pre-patterning to template the formation of specific desired complex structures.

6.4 Summary

To summarize, we have shown that soild-state dewetting of patches patterned from single crystal nickel films leads to formation of regular line or island patterns with increased complexity. The regular shapes of the patterns depend strongly on the shapes and locations of internal holes as well as the crystallographic alignments and sizes of the initial patches. We investigated the origins of specific shapes of various dewetted patterns by analyzing morphological evolution of patches and showed that the effects of surface energy anisotropy and pattern corners (convex and concave) on edge retraction and instabilities (corner-induced instability, pinch-off instability, and Rayleigh-like instability) determine the specific shapes of the dewetted structures. This study will provide new strategies to produce regular structures with smaller scales and more complexity than the initial patterns.

Chapter 7

Summary and Future Work

7.1 Summary

Solid-state dewetting of as-deposited and pre-patterned single crystal Ni(100) and Ni(110) films was investigated. In chapter 3 and 4, we presented results of studies on the morphological evolution during dewetting of as-deposited single crystal Ni films. During dewetting, as-deposited single crystal Ni films evolve to form regular dewetting morphologies through the nucleation and growth of natural holes with regular shapes. In the early stage of dewetting, natural holes have simple in-plane faceted shapes that depend strongly on the crystallographic orientation of a film and on the annealing ambient. Through investigations of the retraction velocity and faceting of pre-patterned long edges oriented in various crystallographic directions, we showed that surface energy anisotropy of Ni leads to prominent local minima of the edge retraction velocity in specific directions and results in the specific shapes of natural holes. We also showed the effect of anisotropic surface diffusion on the anisotropy of the edge retraction velocity by analyzing the breakdown of four-fold symmetry in the polar plots for the edge retraction velocity in Ni(100) films. The breakdown of four-fold symmetry was consistent with orientations of ledge structures that resulted from a small misorientation between the film and substrate. In the late stage of dewetting, natural holes grow

unstably with more complex shapes and eventually form regular island morphologies. Corner-induced, pinch-off, fingering and Rayleigh-like instabilities were identified as underlying kinetic mechanisms through analyses of the complex morphological evolution.

In chapter 5 and 6, we showed that solid-state dewetting of patches patterned from single crystal Ni films leads to formation of regular structures with smaller dimensions and more complexity than the initial patches. Initial geometric characteristics of patches as well as surface energy anisotropy of Ni were found to play critical roles in determining specific shapes of the dewetted structures. Dewetting results for square, cross, and long line patches patterned from Ni(110) films demonstrated the effect of surface energy anisotropy, initial widths of patches, and patch corners on the pinch-off behavior of edges and the number of lines formed through retraction and pinch-off of edges. It was also shown that pinch-off does not occur during dewetting of patches patterned from Ni(100) films, and that this is associated with lower surface energy of a Ni(100) surface compared to a Ni(110) surface. Regular line or island patterns with other various shapes were produced by adding internal holes or varying the initial in-plane crystallographic alignments of patches. The specific shape of each dewetted pattern was analyzed and found to also form through anisotropic edge retraction, pinch-off instability, corner-induced instability, and Rayleigh-instability, each of which is profoundly influenced by the surface energy anisotropy of Ni. These mechanistic understandings will provide a basis for a further exploitation of solid-state dewetting of

single crystal films to produce self-assembled structures in highly predictable and deterministic ways.

7.2 Future work

The work reported here will be the basis for future research on various aspects of solid-state dewetting of single crystal films. Several examples of future research directions following this work are suggested in this section.

In chapter 3 and 4, we showed that the annealing ambient plays a critical role in determining the dewetting morphologies of Ni films by affecting the surface energy anisotropy of Ni. The observed dependence of faceting on the flow rate of reducing gas was consistent with the known effect of oxygen adsorption on the surface energy anisotropy of Ni. Given that the effect of oxygen adsorption has been shown to be significantly different among different metals [66, 67], carrying out the dewetting experiments described in chapter 3 and 4 for different metal films will be an interesting topic for future work. Such work will help us to further generalize the proposed theory for the dominant effect of the surface energy anisotropy of a film material on determining the specific shapes of dewetting morphologies. The difference in the crystallographic symmetry of an initial film surface will result in different crystallographic constraints imposed by surface minimization of the film surface. However, these constraints will be consistent with those seen in Ni(100) and Ni(110) films investigated in this thesis. Therefore, future research on films that have different symmetries will help to further

improve our understanding of dewetting mechanisms that reproducibly produce more various regular patterns.

In chapter 5 and 6, we reported results showing the formation of various regular structures via solid-state dewetting of single crystal Ni films. The results demonstrated that solid-state dewetting of single crystal thin films can be used as a fabrication method for self-assembled regular structures. Our analyses of regular morphological evolution during dewetting of patches led to key mechanistic understandings that can provide predictability for shapes of dewetted structures. Development of 3-dimensional models for dewetting of patterned single crystal films will further increase the predictability and also deepen physical insights into the effects of pattern geometries and surface energy anisotropy on the dewetting processes.

Nanomaterials have unique electronic, magnetic, photonic, and chemical properties that are significantly different from those of bulk materials and depend strongly on their size and shape. Much effort has been made to exploit the unique properties of nanomaterials to fabricate a broad range of novel devices. Highly ordered nanostructures with controlled shapes are fundamental building blocks for fabrication of nanodevices. The fabrication of ordered nanostructures with specific shapes via solid-state dewetting of patterned single crystal films is a potential area of future researche following this work. Regular structures produced in this work have lateral dimensions ranging from a few micrometers to several tens of micrometers and individual line widths or island sizes ranging from several hundreds of nanometers to around a micrometer. Reduction of the initial patch size and film thickness is required to produce dewetted

structures with nanoscale feature sizes. Nanofabrication methods such as interference lithography, electron beam lithography, and nanoimprint lithography will be needed to fabricate smaller initial patches. It should also be noted that dewetting of thinner films will proceed with larger amounts of oxygen absorbates on the dewetting film surface because of a higher dewetting rate. Therefore, more systematic study of the association of oxygen absorbates with dewetting morphologies and use of a UHV annealing apparatus will be important in future research. Better control over the amounts of oxygen absorbates on the film surface might be achieved by annealing the film at temperatures below the dewetting temperatures, but high enough to reduce the oxide for a certain amount of time and subsequently increasing the temperature to induce dewetting.

Ni nanostructures produced via solid-state dewetting will provide further research opportunities. Ordered single crystal Ni nanostructures can be used as catalysts for growing ordered arrays of carbon nanotubes. Because the crystallographic orientations of the Ni nanostructures will be controlled by epitaxial relationships between Ni and MgO, the dewetted Ni nanostructures will provide an opportunity to study the effect of crystallographic orientations of catalysts on the growth of carbon nanotubes. Another potential research subject is studying the magnetic properties of the dewetted Ni nanostructures. It is known that magnetic properties such as the magnetic anisotropy and magnetic switching behavior strongly depend on the geometry and crystallographic orientation of a magnetic structure [68-70]. The effect of geometries and crystallographic alignments of magnetic nanostructures can be investigated in detail through magnetic characterization of single crystal Ni nanostructures with various shapes.

Appendix A Dewetting of Ni films with various initial thicknesses

In this thesis, dewetting mechanisms of single crystal films were studied by analyzing morphological evolution during dewetting of 120 nm-thick single crystal Ni films. In this section, we present dewetting results for Ni films with various initial thicknesses

Figure A-1 shows dewetting results of Ni(110) films with various initial thicknesses. Each film was annealed in the Transtemp tube furnace at 900°C under a reducing gas flow rate of 90 sccm. As seen in the figure, thinner films evolve to form arrays of lines and islands earlier, indicating that the rate of dewetting becomes higher as the initial film thickness becomes smaller. The higher dewetting rate of thinner films can be understood in terms of the larger gradient in local surface curvature at edges of holes. The shapes of growing holes and island morphologies also depend on the initial film thickness. For the case of 120 nm-thick and 60 nm-thick films, the orientations of hole edges and dewetted lines significantly deviate from the <001> directions during dewetting, as shown in Figs. A-1(b) and A-1(c). The angles of rotation with respect to the <001> directions are generally smaller in 60 nm-thick films. As seen in Fig. A-1(d), the angle of rotation further decreases and most dewetted lines are nearly parallel to the <001> directions when the initial film thickness is decreased to 15 nm. The difference in the in-plane orientations of lines and edges might be associated with the effect of initial film thickness on the amount of oxygen adsorbates on dewetting Ni films. Because the

dewetting rate is higher as the initial film thickness is smaller as mentioned earlier, the amounts of oxygen adsorbates on the dewetting film surfaces will be larger for thinner films, presuming the rate of surface oxide reduction will be independent of the initial film thickness. This can cause the difference in the surface energy anisotropy of Ni during dewetting for different initial film thicknesses, and eventually result in dewetted morphologies that depend strongly on the initial film thickness, as shown in Fig. A-1.

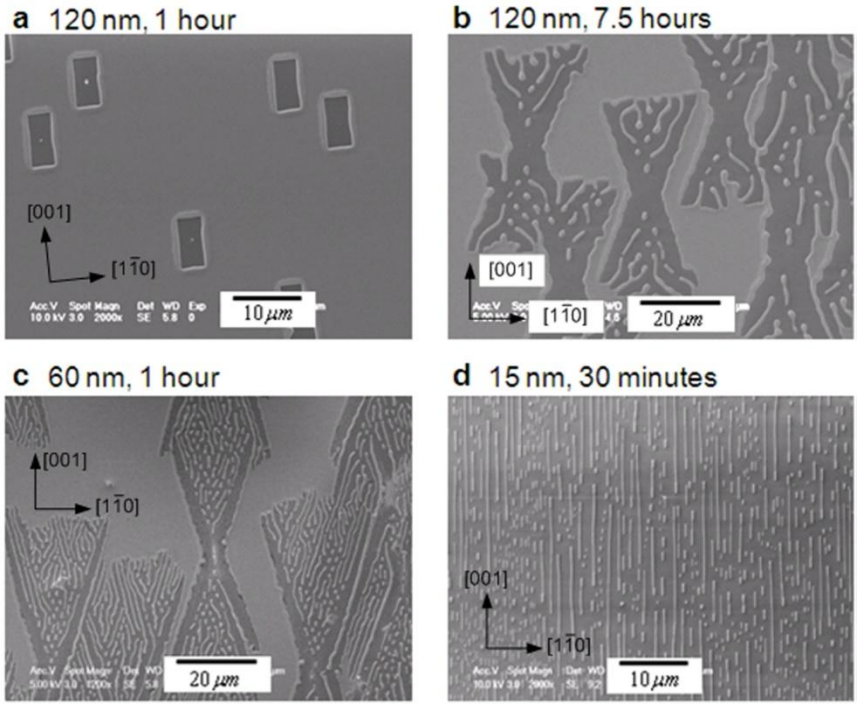

Figure A-1. SEM images showing dewetting results for Ni(110) films with various initial film thicknesses. The initial film thickness and annealing time is indicated for each image. The in-plane crystallographic orientations are also indicated in each image.

Appendix B The effect of annealing temperature on dewetting rates and morphologies

In this section, we present dewetting results for Ni films that were annealed at different temperatures. We have shown that dewetting of single crystal Ni films occurs via surface self-diffusion. Surface diffusion is a thermally activated process and the surface diffusivity is expressed as

$$D_S = D_0 \exp(-\frac{E_a}{kT}),$$

where D_0 is the pre-exponential factor, E_a is the activation energy for surface diffusion, k is Boltzmann's constant, T is temperature. Therefore, as the annealing temperature is increased, the surface diffusivity and dewetting rate also increase.

Figure B-1 shows dewetting results for 15 nm-thick Ni(110) films that were annealed at different temperatures for 1 hour. Annealing was carried out in the Transtemp tube furnace under a reducing gas flow rate of 90 sccm. As seen in the figure, the films dewet to form line morphologies that are generally parallel to the [001] direction, but the dewetting rate is higher at 900°C than at 500°C, resulting in higher lines and a more discontinuous film at 900°C.

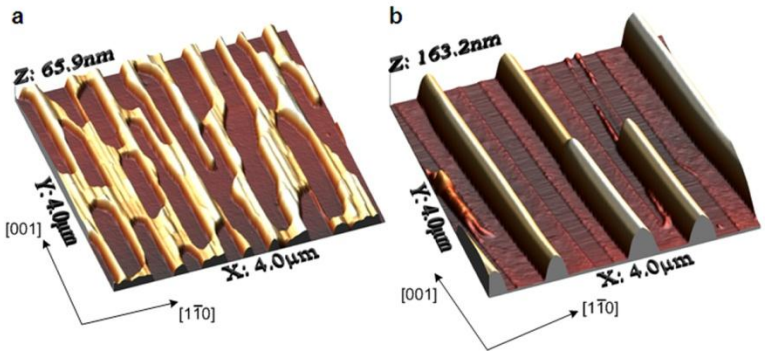

Figure B-1. AFM images showing dewetting results for 15nm-thick Ni(110) films. (a) Annealed at 500°C. (b) Annealed at 900°C.

Figure B-2 shows shapes of natural holes observed during dewetting of 120nm-thick Ni(110) films that were annealed at three different temperatures (700°C, 800°C, and 900°C). Annealing of these films was also carried out in the Transtemp tube furnace under a reducing gas flow rate of 90 sccm. As the annealing temperature was decreased, a longer annealing time was required to form natural holes and the growth rate of the holes was found to be lower. This also shows that the rate of dewetting increases with an increasing annealing temperature. As seen in Fig. B-2, the natural holes were longer in the [001] direction at the three different annealing temperatures, but the aspect ratio of the natural hole increased as the annealing temperature was decreased. It has been shown that the surface energy anisotropy of crystalline solids increases with decreasing temperature [71, 72]. Given the effect of surface energy anisotropy on the shape of natural holes (see chapter 3), the higher aspect-ratio of natural holes at lower temperature is likely to be associated with the higher anisotropy of surface energy at lower temperatures. The anisotropy of surface diffusivity and the rate of oxide reduction also

depend on temperature and can also affect the results shown in Fig. B-2. Systematic investigation of the temperature dependence of hole shapes will be an interesting future research direction.

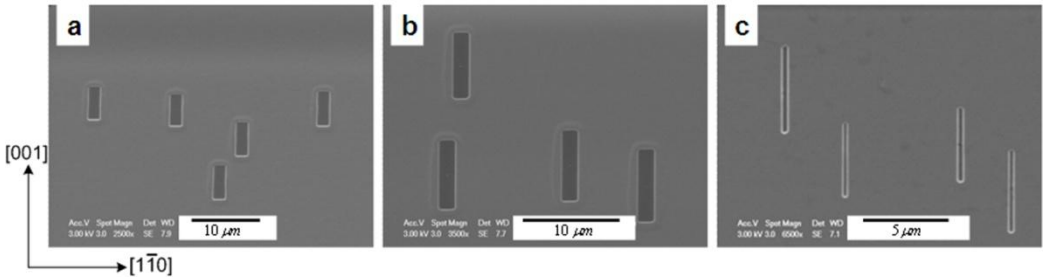

Figure B-2. SEM images of natural holes that formed during dewetting of 120nm-thick Ni(110) films. (a) Annealed at 900°C for 30 minutes. (b) Annealed at 800°C for 2.5 hours. (c) Annealed at 700°C for 6 hours. The in-plane crystallographic orientation is indicated in the lower-left corner.

Appendix C The effect of the adhesion energy on the edge retraction velocity

We calculated the edge retraction distance for different values of the adhesion energy using the crystalline method. The equilibrium shape and surface diffusivity were set to be the same as those shown in Fig. 5-21. The initial width was set to 160. In these simulations, pinch-off did not occur and thickening rims completely merged to form single agglomerate. As seen in Fig. C-1, the edge retraction velocity is seen to be almost independent of the magnitude of the film-substrate adhesion energy.

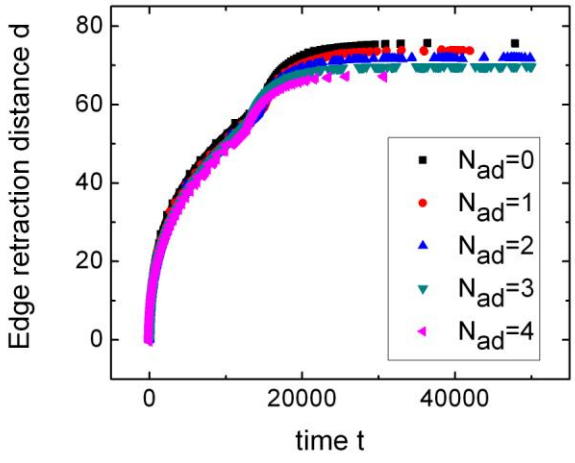

Figure C-1. The edge retraction distance versus time for different magnitudes of the adhesion energy. The larger value of N_{ad} indicates the higher adhesion energy. The edge retraction distance at time t is calculated by dividing the change in length of the film-substrate interfacial facet by 2.

References

1. W.L. Winterbottom, *Equilibrium Shape of a Small Particle in Contact with a Foreign Substrate.* Acta Metallurgica, 1967. **15**(2): p. 303-310.
2. W.C. Carter et al., *Shape Evolution by Surface-Diffusion End Surface Attachment Limited Kinetics on Completely Faceted Surfaces.* Acta Metallurgica Et Materialia, 1995. **43**(12): p. 4309-4323.
3. W.W. Mullins, *Flattening of a Nearly Plane Solid Surface Due to Capillarity.* Journal of Applied Physics, 1959. **30**(1): p. 77-83.
4. W.W. Mullins, *Theory of Thermal Grooving.* Journal of Applied Physics, 1957. **28**(3): p. 333-339.
5. D.J. Srolovitz and S.A. Safran, *Capillary Instabilities in Thin-Films .1. Energetics.* Journal of Applied Physics, 1986. **60**(1): p. 247-254.
6. D.T. Danielson et al., *Surface-energy-driven dewetting theory of silicon-on-insulator agglomeration.* Journal of Applied Physics, 2006. **100**(8): p. 083057.
7. D.J. Srolovitz, D.J. and S.A. Safran, *Capillary Instabilities in Thin-Films .2. Kinetics.* Journal of Applied Physics, 1986. **60**(1): p. 255-260.
8. E. Jiran and C.V. Thompson, *Capillary Instabilities in Thin, Continuous Films.* Thin Solid Films, 1992. **208**(1): p. 23-28.
9. E. Jiran and C.V. Thompson, *Capillary Instabilities in Thin-Films.* Journal of Electronic Materials, 1990. **19**(11): p. 1153-1160.
10. R.H. Brandon and F.J. Bradshaw, *The mobility of the surface atoms of copper and silver evaporated deposits*, in *Technical Report*. 1966, Royal Aircraft Establishment: Farnborough.
11. H. Wong et al., *Periodic mass shedding of a retracting solid film step.* Acta Materialia, 2000. **48**(8): p. 1719-1728.
12. E. Dornel, E, *Surface diffusion dewetting of thin solid films: Numerical method and application to Si/SiO2.* Physical Review B, 2006. **73**(11): p. 115427.
13. W. Kan and H. Wong, *Fingering instability of a retracting solid film edge.* Journal of Applied Physics, 2005. **97**(4): p. 043515.
14. F.A. Nichols and W.W. Mullins, *Surface- (Interface-) and Volume-Diffusion Contributions to Morphological Changes Driven by Capillarity.* Transactions of the Metallurgical Society of Aime, 1965. **233**(10): p. 1840-1848.
15. D.J. Srolovitz and C.V. Thompson, *Beading Instabilities in Thin-Film Lines with Bamboo Microstructures.* Thin Solid Films, 1986. **139**(2): p. 133-141.
16. M.S. McCallum, *Capillary instabilities in solid thin films: Lines.* Journal of Applied Physics, 1996. **79**(10): p. 7604-7611.
17. J.W. Cahn, *Stability of Rods with Anisotropic Surface Free-Energy.* Scripta Metallurgica, 1979. **13**(11): p. 1069-1071.
18. K. Sieradzki, K. Bailey, and T.L. Alford, *Agglomeration and percolation conductivity.* Applied Physics Letters, 2001. **79**(21): p. 3401-3403.

19. A.E. Presland, G.L. Price, and D.L. Trimm, *Hillock Formation by Surface Diffusion on Thin Silver Films.* Surface Science, 1972. **29**(2): p. 424-434.
20. A.E. Presland, G.L. Price, and D.L. Trimm, *Role of Microstructure and Surface-Energy in Hole Growth and Island Formation in Thin Silver Films.* Surface Science, 1972. **29**(2): p. 435-446.
21. S.K. Sharma and J. Spitz, *Hillock Formation, Hole Growth and Agglomeration in Thin Silver Films.* Thin Solid Films, 1980. **65**(3): p. 339-350.
22. S.K. Sharma and J. Spitz, *Void Growth in Thin Silver Films.* Thin Solid Films, 1980. **67**(1): p. 109-116.
23. R.E. Hummel et al., *Thermal Grooving, Thermotransport and Electrotransport in Doped and Undoped Thin Gold-Films.* Thin Solid Films, 1981. **78**(1): p. 1-14.
24. J.Y. Kwon et al., *Comparison of the agglomeration behavior of Au and Cu films sputter deposited on silicon dioxide.* Journal of Applied Physics, 2003. **93**(6): p. 3270-3278.
25. C.M. Kennefick and R. Raj, *Copper on Sapphire - Stability of Thin-Films at 0.7-Tm.* Acta Metallurgica, 1989. **37**(11): p. 2947-2952.
26. A.L. Giermann and C.V. Thompson, *Solid-state dewetting for ordered arrays of crystallographically oriented metal particles.* Applied Physics Letters, 2005. **86**(12): p. 121903.
27. A.L. Giermann, C.V. Thompson, and H.I. Smith, *Templated formation of ordered metallic nano-particle arrays.* Nanoparticles and Nanowire Building Blocks-Synthesis, Processing, Characterization and Theory, 2004. **818**: p. 37-42
28. A.L. Giermann, *Templated dewetting of thin solid films.* Ph.D Thesis, MIT Dept. Mat. Sci. and Eng., 2009.
29. Y.J. Oh et al., *Cobalt Nanoparticle Arrays made by Templated Solid-State Dewetting.* Small, 2009. **5**(7): p. 860-865.
30. J. Petersen and S.G. Mayr, *Dewetting of Ni and NiAg solid thin films and formation of nanowires on ripple patterned substrates.* Journal of Applied Physics, 2008. **103**(2): p. 023520.
31. J. Basu et al., *Nanopatterning by solid-state dewetting on reconstructed ceramic surfaces.* Applied Physics Letters, 2009. **94**(17): p. 171114.
32. Y. Ono et al., *Thermal Agglomeration of Thin Single-Crystal Si on Sio2 in Vacuum.* Japanese Journal of Applied Physics Part 1-Regular Papers Short Notes & Review Papers, 1995. **34**(4A): p. 1728-1735.
33. R. Nuryadi, Y. Ishikawa, and M. Tabe, *Formation and ordering of self-assembled Si islands by ultrahigh vacuum annealing of ultrathin bonded silicon-on-insulator structure.* Applied Surface Science, 2000. **159**: p. 121-126.
34. R. Nuryadi et al., *Thermal agglomeration of single-crystalline Si layer on buried SiO2 in ultrahigh vacuum.* Journal of Vacuum Science & Technology B, 2002. **20**(1): p. 167-172.
35. Y. Fan et al., *Thermal agglomeration of ultrathin silicon-on-insulator layers: Crystalline orientation dependence.* Japanese Journal of Applied Physics, 2008. **47**(3): p. 1461-1464.

36. Z.A. Burhanudin et al., *Transition from wire formation to island formation in thermal agglomeration of a (111) silicon-on-insulator layer.* Thin Solid Films, 2006. **508**(1-2): p. 235-238.
37. P. Sutter et al., *Mechanisms of thermally induced dewetting of ultrathin silicon-on-insulator.* Applied Physics Letters, 2006. **88**(14): p. 141924.
38. K.N. Tu, *Interdiffusion in Thin-Films.* Annual Review of Materials Science, 1985. **15**: p. 147-176.
39. Y. Ishikawa et al., *Effect of patterning on thermal agglomeration of ultrathin silicon-on-insulator layer.* Applied Surface Science, 2002. **190**(1-4): p. 11-15.
40. Y. Ishikawa et al., *Pattern-induced alignment of silicon islands on buried oxide layer of silicon-on-insulator structure.* Applied Physics Letters, 2003. **83**(15): p. 3162-3164.
41. S. Chikazumi, *Epitaxial Growth and Magnetic Properties of Single-Crystal Films of Iron, Nickel, and Permalloy.* Journal of Applied Physics, 1961. **32**(3): p. S81-S82.
42. H. Qiu et al., *Epitaxial growth, structure and properties of Ni films grown on MgO(100) by d.c. bias sputter deposition.* Thin Solid films, 1994. **241**: p. 9-11
43. P. Sandstrom et al., *Structure and surface morphology of epitaxial Ni films on MgO(111) and (001) substrates: Growth of high quality single domain films.* Mechanisms and Principles of Epitaxial Growth in Metallic Systems, 1998. **528**: p. 209-217
44. R.A. Lukaszew et al., *Annealing effects on (001) Ni films grown on MgO.* Applied Surface Science, 2003. **219**(1-2): p. 74-79.
45. C. Lin et al., *Morphology evolution of thin Ni film on MgO(100) substrate.* Journal of Physics D-Applied Physics, 2002. **35**(15): p. 1864-1866.
46. W. Tian et al., *Hexagonal close-packed Ni nanostructures grown on the (001) surface of MgO.* Applied Physics Letters, 2005. **86**(13): p. 131915.
47. K. Helming et al., *A new method for texture measurements using a general area detector diffraction system.* Powder Diffraction, 2003. **18**(2): p. 99-102.
48. D.R. Gaskell, *Introduction to the thermodynamics of materials*. 3rd ed. 1995, New york: Taylor & Francis.
49. I. Horcas et al., *WSXM: A software for scanning probe microscopy and a tool for nanotechnology.* Review of Scientific Instruments, 2007. **78**(1): p. 013705.
50. J. Mayer et al., *TEM sample preparation and FIB-induced damage.* Mrs Bulletin, 2007. **32**(5): p. 400-407.
51. J. Villain, *Nonequilibrium Systems - the Shape of Crystals to Come.* Nature, 1991. **350**(6316): p. 273-274.
52. D.X. Du et al., *Systematic prediction of kinetically limited crystal growth morphologies.* Physical Review Letters, 2005. **95**(15): p. 155503.
53. C. Herring, *Some Theorems on the Free Energies of Crystal Surfaces.* Physical Review, 1951. **82**(1): p. 87-93.
54. H. Mykura, *The variation of the surface tension of nickel with crystallographic orientation.* Acta Metallurgica, 1961. **9**(6): p. 570-576.

55. J.M. Blakely and H. Mykura, *The effect of impurity adsorption on the surface energy and surface self diffusion in nickel.* Acta Metallurgica, 1961. **9**(6): p. 595-599.
56. R. Hielscher and H. Schaeben, *A novel pole figure inversion method: specification of the MTEX algorithm.* Journal of Applied Crystallography, 2008. **41**: p. 1024-1037.
57. P.S. Maiya and J.M. Blakely, *Surface Self-Diffusion and Surface Energy of Nickel.* Journal of Applied Physics, 1967. **38**(2): p. 698-704.
58. R.L. Schwoebel and E.J. Shipsey, *Step Motion on Crystal Surfaces.* Journal of Applied Physics, 1966. **37**(10): p. 3682-3686.
59. R.L. Schwoebel, *Step Motion on Crystal Surfaces .2.* Journal of Applied Physics, 1969. **40**(2): p. 614-618.
60. G. Ehrlich and F.G. Hudda, *Atomic View of Surface Self-Diffusion - Tungsten on Tungsten.* Journal of Chemical Physics, 1966. **44**(3): p. 1039-1049.
61. J. Ye and C.V. Thompson, *Mechanisms of complex morphological evolution during solid-state dewetting of single-crystal nickel thin films.* Applied Physics Letters, 2010. **97**(7): p. 071904.
62. M.C. Flemings, *Solidification Processing.* Metallurgical Transactions, 1974. **5**(10): p. 2121-2134.
63. H. Wong et al., *Capillarity driven motion of solid film wedges.* Acta Materialia, 1997. **45**(6): p. 2477-2484.
64. S.M. Foiles, M.I. Baskes, and M.S. Daw, *Embedded-Atom-Method Functions for the Fcc Metals Cu, Ag, Au, Ni, Pd, Pt, and Their Alloys.* Physical Review B, 1986. **33**(12): p. 7983-7991.
65. J.E. Taylor, *Mean-Curvature and Weighted Mean-Curvature .2.* Acta Metallurgica Et Materialia, 1992. **40**(7): p. 1475-1485.
66. F. Mittendorfer et al., *Morphology of mesoscopic Rh and Pd nanoparticles under oxidizing conditions.* Physical Review B, 2007. **76**(23): p. 233413.
67. N. Seriani and F. Mittendorfer, *Platinum-group and noble metals under oxidizing conditions.* Journal of Physics-Condensed Matter, 2008. **20**(18): p. 184023.
68. M. Klaui et al., *Vortex formation in narrow ferromagnetic rings.* Journal of Physics-Condensed Matter, 2003. **15**(21): p. R985-R1023.
69. J.M. Shaw et al., *Effect of microstructure on magnetic properties and anisotropy distributions in Co/Pd thin films and nanostructures.* Physical Review B, 2009. **80**(18): p. 184419.
70. S.Y. Chou, *Patterned magnetic nanostructures and quantized magnetic disks.* Proceedings of the IEEE, 1997. **85**(4): p. 652-671.
71. M. Mclean and H. Mykura, *Temperature Dependence of Surface Energy Anisotropy of Platinum.* Surface Science, 1966. **5**(4): p. 466-481.
72. D.M. Saylor, D.E. Mason, and G.S. Rohrer, *Experimental method for determining surface energy anisotropy and its application to magnesia.* Journal of the American Ceramic Society, 2000. **83**(5): p. 1226-1232.